

Multi-Objective Design Optimization of Compliant Lunar Wheels

Michele Faragalli

Doctor of Philosophy

Department of Mechanical Engineering

McGill University

Montreal, Quebec

2013-04-15

A Thesis submitted to the Faculty of Graduate studies in partial fulfilment of a
Doctorate of Philosophy

©Michele Faragalli, 2013

DEDICATION

This thesis is dedicated to all those who've given me the freedom to pursue my dreams. It is my hope that this work constitutes another small step towards returning to the Moon.

ACKNOWLEDGEMENTS

There are countless people to thank for motivating, inspiring, supporting and challenging me throughout my studies. None of this work would have been possible without the complimentary guidance of my supervisors, Drs. Peter Radziszewski and Damiano Pasini. I would also like to thank Mo Farhat of the Canadian Space Agency and Brad Jones of Neptec Design Group for their support of the McGill-CSA-Neptec compliant wheel PSP, through which this research has been funded. Thank you to Nima, Dan, Suda, Robin, Nasim and all the undergraduate students that have contributed to the compliant wheel project. Special thanks also goes out to the members of Dr Pasini's group, especially Sajad, Andrea, Kazem, Swaroop and Mahdi.

There are also many who contributed to this work indirectly: Nico, Adam and Marco for all the men's night adventures; Ozgur, for the lunch-time conversations; Tim, for the epic squash games; and Carlos for all the great chats.

Lastly and most importantly, I must thank my better half. Zaida, I know that I would not have been able to surmount all of the challenges I've faced without your unwavering love and support. I love you.

ABSTRACT

The development of the wire-mesh wheel of the Apollo Lunar Roving Vehicle was realized through a time consuming trial and error design process, primarily driven by manufacturability and physical testing. Recent wheel development, motivated by renewed interest in lunar surface exploration, utilizes more sophisticated numerical simulation tools. However, many researchers still employ trial and error or parametric approaches to designing the wheels.

This thesis proposes a systematic approach to the design optimization of compliant lunar wheels. The problem is decomposed into system and component level analyses. The system level analysis investigates the effect of elastic wheel behaviour on rover and mission performance metrics. This is realized by optimizing concept independent wheel design variables using multi-disciplinary models coupled with optimization algorithms. Wheel concepts are explored by prototyping and physical testing, as well as numerical modelling. The mobility performance metrics of cellular, segmented and iRings wheels are compared to a baseline rubber wheel. In the component level analysis, a multi-objective optimization algorithm is coupled with numerical simulations of wheel-ground interaction to find optimal cellular wheel designs. The effectiveness of the methodology to optimize cellular wheel concepts is verified, and the limitations of the approach examined. Finally, a discussion to extend the proposed methodology to alternative wheel concepts is provided.

ABRÉGÉ

Le développement de la roue treillis métallique de l’Apollo Lunar Roving Vehicle a été réalisé par un processus d’essais et d’erreurs. Les récents développements de roues flexibles, motivé par un regain d’intérêt pour l’exploration lunaire, ont maintenant à leur disposition des outils de simulation numérique plus sophistiqués. Cependant, la majorité des chercheurs emploient toujours des méthodes expérimentales, itératives ou paramétriques pour développer leurs roues.

Cette thèse propose une nouvelle approche systématique pour l’optimisation de concepts de roues lunaires flexibles. Le problème est décomposé en deux analyses se rapportant au niveau du système et celui des composantes. L’analyse au niveau du système étudie l’effet du comportement de la roue élastique sur des mesures de performance lors d’une mission du rover. Ceci est réalisé en optimisant les paramètres décrivant une roue flexible à l’aide de modèles multidisciplinaires. Différents concepts de roues sont explorés à l’aide de prototypes et d’essais physiques, ainsi que de modélisations numériques. La performance de chacun des concepts de roues flexibles cellulaires, iRings et segmentés sont comparées à un pneu standard. L’analyse au niveau des composantes effectue une optimisation multi-objective afin de déterminer, par le biais de simulations numériques, le concept optimal de roues flexibles cellulaires. L’efficacité de la méthodologie pour optimiser la roue cellulaire est ensuite vérifiée et les limites de cette approche sont examinées en détail. Finalement, une discussion sur l’application de la méthodologie proposée à des concepts de roues arbitraires est abordée.

TABLE OF CONTENTS

DEDICATION	ii
ACKNOWLEDGEMENTS	iii
ABSTRACT	iv
ABRÉGÉ	v
LIST OF TABLES	ix
LIST OF FIGURES	xi
1 Introduction	1
1.1 Motivation	1
1.1.1 Problem Statement	3
1.2 Research Objectives	3
1.3 Thesis Outline	5
2 Literature Review	8
2.1 Planetary Surface Mobility	8
2.1.1 Modelling and Testing Mobility Performance	10
2.1.2 Existing Wheel Designs and Design Methodologies	14
2.2 Optimization Theory	21
2.2.1 Structural Optimization and Compliant Mechanisms	21
2.2.2 Design Optimization	23
2.3 Material Modelling	25
2.3.1 Cellular Materials	26
2.3.2 Homogenization of Lattice Materials	27
2.4 Summary of Literature Review	30
3 Systematic Wheel Design Methodology	32
3.1 Design Framework	32

3.2	System Level Optimization	35
3.3	Wheel Concept Development and Selection	36
3.4	Component Level Optimization	38
4	System Level Optimization	42
4.1	Performance Metrics for Planetary Exploration Vehicles	42
4.2	Multi-Disciplinary Performance Models	44
4.2.1	Elastically Compliant Wheel Pseudo-model	46
4.2.2	Terramechanics Model	47
4.2.3	Rover Steering Model	50
4.2.4	Simplified Rover Dynamics Model	53
4.2.5	Mission Performance Models	56
4.3	Wheel Optimization for Lunar Missions	60
4.3.1	Prospecting Mission Optimization	61
4.3.2	Excavation Mission Optimization	66
4.4	System Level Analysis Discussion	71
5	Development, Testing and Modelling of Wheel Design Concepts	73
5.1	Wheel Development	73
5.1.1	Segmented Wheel Concept	74
5.1.2	Cellular Wheel Concept	75
5.1.3	iRings Wheel Concept	77
5.1.4	Baseline Rubber Pneumatic Tire	77
5.2	Experimental Performance Investigation	79
5.2.1	Qualitative Performance Comparison	79
5.2.2	Trafficability and Maneuverability Testing	82
5.2.3	Dynamic Terrainability Testing	86
5.3	Preliminary Numerical Investigation	90
5.3.1	Segmented Wheel Structural Optimization	91
5.3.2	Cellular Wheel Parametric Analysis	102
5.4	Selection of Wheel Concepts	108
6	Component Level Optimization	111
6.1	Homogeneous Wheel Multi-Objective Optimization	111
6.1.1	Wheel MOO Problem Formulation	113
6.1.2	MOO Algorithm	115
6.1.3	Wheel MOO Results	117

6.2	Cellular Material Optimization	126
6.2.1	Unit Cell Designs	126
6.2.2	Cellular Material Optimization Problem Formulation . . .	128
6.2.3	Cellular Material Optimization Results	130
6.3	Error Analysis	135
6.3.1	Component Level Error Analysis	135
6.3.2	System-Component Level Error Analysis	139
6.3.3	Rigid Ground Verification	142
6.4	Discussion of Component Level Optimization	144
7	Conclusions and Recommendations	147
7.1	Contributions	150
7.2	Limitations of Current Methodology and Future Work	150
7.3	Recommendations for Flight Rover Wheels	153
	Appendix	154
A	Parametric Mission and Rover Mobility Performance Analysis	154
A.1	Mission Performance Analysis	154
A.1.1	Prospecting Mission Scenario	154
A.1.2	Excavating Mission Scenario	158
A.2	Rover Performance Analysis	165
A.2.1	Rover Trafficability and Manoeuvrability Analysis	166
A.2.2	Rover Dynamic Terrainability Analysis	170
B	Closed-form Material Constitutive Models	173
B.1	2D Hexagonal Unit Cell Properties	173
B.2	Cubic Unit Cell Properties	173
B.3	Body Centred Cube Unit Cell Properties	174
B.4	Face Centred Cube Unit Cell Properties	175
B.5	Cuboctahedron Unit Cell Properties	177
	REFERENCES	181

LIST OF TABLES

<u>Table</u>		<u>page</u>
2-1	Lunar rover missions as a function of lunar base development [33] . . .	9
4-1	Surface Exploration Vehicle Performance Metrics	45
4-2	Material-Soil lateral sliding coefficients [119]	52
4-3	Terrain Roughness Parameters [94] [98]	55
4-4	Mission Scenario Parameters ($\mathbf{c}_{mission}$)	61
4-5	Lunar Environmental Properties (\mathbf{c}_{env})	62
4-6	Rover Parameters (\mathbf{C}_{rover})	62
4-7	Prospecting Mission Optimization Results	65
4-8	Excavation Mission Optimization Results	69
5-1	Qualitative Wheel Performance Evaluation	80
5-2	Traction system C_r	84
5-3	Driving efficiency η_{DP}	85
5-4	Turning efficiency η_{st}	85
5-5	Wheel Dynamic Properties	87
5-6	Genetic algorithm properties	97
5-7	Solution for geometrically and structurally optimum segments	98
5-8	Unit cell 2D homogenized properties found in [65]	104
5-9	Homogeneous Cellular Wheel Parametric Analysis	106
6-1	Wheel Simulation Parameters	112

6-2	NSGA-II Algorithm Parameters	117
6-3	Weighting coefficients for trade-off solutions	119
6-4	Trade-off solutions from single layer MOO	122
6-5	304 Stainless Steel Material Properties	130
6-6	Cubic and Cuboctahedron cellular material optimization solutions . .	132
6-7	Cubic cellular material solutions for \bar{G}_{zx}	133
6-8	Cuboctahedron cellular material solutions for \bar{E}_{zz}	133
6-9	Hexagonal cellular material optimization solutions	134
6-10	Cubic Wheel Designs Component Level Error Analysis	137
6-11	System-Component Level Verification	140
6-12	GRC-1 Lunar Regolith Soil Simulant Properties [85]	142
6-13	Rigid vs. Soft Soil Results Comparison	144
A-1	Prospecting Scenario Rover Parameters (\mathbf{C}_{rover})	155
A-2	Excavating Rover Parameters (\mathbf{C}_{rover})	160
A-3	Trafficability and Manoeuvrability Analysis Parameters (\mathbf{x}_{sys} and \mathbf{c}_{rover})	166
A-4	Dynamic Terrainability Parameters (\mathbf{x}_{sys} and \mathbf{C}_{rover})	170

LIST OF FIGURES

<u>Figure</u>	<u>page</u>
1.1 LRV Wire Mesh Wheel (NASA) [121]	3
2.1 Planetary Rovers	10
2.2 Numerical Modelling of Wheel-Soil Interaction	11
2.3 Planetary Analog Test Sites	13
2.4 Recent Wheel Developments	17
2.5 Lunar Wheel Development and Selection in the 1970s [7]	18
3.1 Wheel Design Framework	34
3.2 Wheel System Level Analysis	37
3.3 Component Level Optimization Framework	40
4.1 Deformable Wheel-Soil Model	48
4.2 Rover Skid-Steer Model	51
4.3 Simplified rover dynamics model	54
4.4 2D Mckyes Excavation Model [118]	58
4.5 Prospecting Mission Objective Function Results Comparison	64
4.6 Excavation Mission Objective Function Results Comparison	68
5.1 Wheel Configuration Functional Breakdown	73
5.2 McGill Segmented Wheel Concept	75
5.3 Cellular Wheel with aluminum Hexagonal Unit Cells	76
5.4 Cellular Wheel with Polypropylene Circular Unit Cells	76

5.5	McGill's iRings on CSA's Juno II rover	78
5.6	ODG Rubber Wheels	78
5.7	Small scale rubber non-pneumatic tires	79
5.8	Wheel Testing	82
5.9	Drawbar pull Test Set-up	83
5.10	Drawbar pull Testing	84
5.11	Lateral Deformation on Under-inflated Rubber Tires	86
5.12	Terrain Types	87
5.13	Dynamic Terrainability Results	88
5.14	Segmented Wheel Concept	91
5.15	Parameterization of Wheel Segment into Lamé curves	92
5.16	Objective Space	99
5.17	Optimal Segments	101
5.18	Unit Cell Topology Designs	103
5.19	Unit cell macroscopic properties	105
5.20	Cellular Wheel Numerical Investigations	107
6.1	FE Simulation Models	113
6.2	Homogeneous and Gradient Material Wheels	118
6.3	Single Layer MOO Results	120
6.4	Trade-off Solutions Objective Function Values	122
6.5	Multi-Layer MOO Results	125
6.6	Cellular Wheel Unit Cell Topologies of Interest	127
6.7	Cellular Wheels	135

6.8	Optimal Cubic Wheel Designs	138
6.9	Pressure-Strain Relationship for common sandy soils and GRC-1 [85]	143
6.10	Soft soil FE results	143
A.1	Prospecting Mission Performance	156
A.2	Prospecting scenario energy	158
A.3	Berm Building Power Mission Performance	161
A.4	Berm Building Energy Mission Performance	162
A.5	Berm Building Mission Performance	164
A.6	Trafficability Performance Analysis	167
A.7	Maneuverability Performance Analysis	168
A.8	Dynamic Terrainability Performance Analysis	171

CHAPTER 1

Introduction

The history of humanity is shaped by our ability to invent tools. From Homo Habilis' development of rudimentary hunting tools to Homo Erectus' mastering of fire; our survival and evolution to modern Homo Sapiens would not have been possible without technology [50]. The wheel is commonly referred to as one of mankind's most fundamental inventions. The wheel enables movement, the transportation of load and can perform work in a machine. The wheel was most likely invented in Mesopotamia around 5000 BCE as a potter's wheel, while applications of rotary motion for transportation were adopted shortly thereafter [29]. Until 1650 BCE, wheels were still very heavy and bogged down in soft soils, and could not be used on rocky terrain. It was still much easier to transport goods over long distances on animals, and wheeled vehicles were not utilitarian rather, they were a sign of social status [50]. With the development of roads, railways, vehicle suspension and pneumatic rubber tires, wheels became ubiquitous in transportation technology. Now, their applications are as diverse as their designs.

1.1 Motivation

In the early 1960s, as mankind left its cradle to explore the solar system, enabling technologies to launch mass into orbit, sustain human life off the planet and explore our solar system were developed. Yet, according to [7], the development of flexible metallic wheels was the most time consuming and challenging aspects of

Apollo 15, 16 and 17's Lunar Roving Vehicle (LRV) development. The lunar environment precludes the use of rubber, which deteriorates when exposed to solar wind, solar cosmic rays and galactic cosmic radiation [33]. The extreme temperature variation, ranging from 40K in the bottom of shadowed craters to 254K near the equator under full sunlight [98], changes the elasticity of rubber. A lunar pneumatic tire wall would therefore be considerably thinner than terrestrial tires, increasing the risk of tire puncture. This is considered a single point failure for manned and robotic vehicles and an unacceptable mission risk.

Apollo LRV engineers were tasked with designing and fabricating a reliable, flexible metallic wheel replicating the performance of rubber pneumatic tires. The design was realized through a trial and error design process, primarily driven by manufacturability and physical testing [7]. A number of flexible wheel design concepts were explored during the 1960s and 1970s [15] which led to the selection of the wire-mesh wheel concept shown in Figure 1.1. The wheel was capable of supporting the weight of the vehicle and astronauts, provide adequate traction in the lunar soil, add some suspension capability to the LRV when overcoming obstacles and withstand the environment and loading conditions over the 3 day missions [15].

The next generation of lunar vehicles will travel further on the lunar surface, explore permanently shadowed craters and perform a variety of tasks such as transport sensitive payloads, excavate regolith and allow for both robotic and manned operations [33]. Thus, the optimal design of future rover wheels will depend on a different set of environmental, mission specific and vehicle design factors.

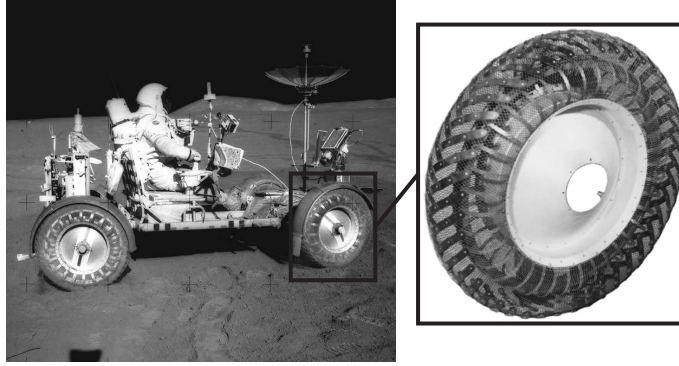


Figure 1.1: LRV Wire Mesh Wheel (NASA) [121]

1.1.1 Problem Statement

A framework is required for the design of flexible wheels for lunar surface vehicles to avoid a time consuming trial and error design process. To date, no methodological approach for developing or optimizing wheel designs for specific mission objectives or performance requirements has been addressed. This thesis develops a systematic approach to the design of compliant wheels for lunar vehicles. The aim being that such a methodology is used to design wheels for various vehicle or mission types, thereby avoiding the need to *reinvent* a wheel for each new planetary exploration vehicle proposed.

1.2 Research Objectives

This research proposes a two-stage sequential optimization approach to the design of compliant, non-rubber, non-pneumatic wheels for planetary exploration vehicles. This is achieved by decomposing the wheel design problem into system and

component level analyses and exploiting multi-disciplinary mathematical and numerical models with single and multi-objective optimization algorithms. As no preferred wheel concept for lunar exploration has been identified in the literature, this research also investigates wheel concepts through prototyping and physical testing. In particular, wheels composed of a periodic microstructure, dubbed cellular wheels, are explored. The design methodology is verified by optimizing a cellular wheel concept. In developing and verifying the proposed methodology, the following research objectives are addressed:

- i Define and classify a comprehensive set of mission and rover mobility specific performance metrics for robotic and manned planetary surface exploration vehicles.
- ii Define and propose system level relationships between concept independent elastic wheels, and mission and rover performance metrics through the use of multi-disciplinary models.
- iii Identify critical wheel design variables for mission success by conducting a system level optimization.
- iv Explore existing and novel wheel concepts through numerical and experimental analyses.
- v Develop a systematic approach to the structural design of compliant lunar wheel concepts by multi-objective optimization (MOO).
- vi Apply and verify the design approach to a cellular wheel concept.

1.3 Thesis Outline

The research presented in this thesis is multi-disciplinary in scope hence a broad literature review of relevant topics is presented first in Chapter 2. Planetary mobility is described by a review of planetary exploration missions and vehicle concepts, as well as simulated and experimental mobility performance evaluation methods. An extensive review of existing wheel concepts and wheel design approaches are also provided. The literature review is completed by introducing pertinent optimization theory and material homogenization methods for cellular materials.

The design framework proposed for optimizing compliant lunar wheels is presented next, in Chapter 3. The decomposition of the design problem is presented in detail, including a description of the system and component level analyses as well as the coordination between the two levels.

Chapter 4 describes the system level analysis. First, a classification and description of a comprehensive set of performance metrics for planetary exploration vehicles are proposed. Terramechanics, vehicle dynamics and mission scenario models are used to characterize the relationship between wheel design variables, rover performance, and consequently, mission performance. Two lunar rover missions are investigated: a resource prospecting and berm building scenario. Both mission scenarios are considered for autonomous or tele-operated rovers in preparation for establishing a lunar outpost in the near future. Resource prospecting consists of traversing long distances on the lunar surface and searching for in-situ water or ice. Berm building requires the rover to excavate lunar soil (i.e. regolith) using a scooping tool and transport it to construct a protective wall between landing sites and a lunar base. Detailed

mission architectures have not yet been developed, so specific mission priorities are unknown. Therefore, a set of relevant mission performance metrics for each scenario are identified by the author. For each metric, an optimization problem is formulated and solved to determine optimal wheel system design variables.

The development and investigation of promising wheel concepts, presented in Chapter 5, precedes the component level analysis. First, a functional breakdown is presented by describing the main components of wheel concepts. Then, four distinct wheel concepts are described and investigated through qualitative and quantitative physical testing and numerical analyses. In addition to the mobility performance, the selection criteria of wheel concepts suitable for component level analysis are proposed. A wheel with an internal structure composed of a periodic microstructure, or cellular material, is identified as the preferred concept and is investigated further in Chapter 6.

Chapter 6 describes the component level analysis in two main steps: a multi-objective optimization (MOO) of a homogeneous 3D wheel model and a cellular material optimization. The cellular wheel concept is simplified as a homogeneous wheel composed of a 3D orthotropic material. The Non-dominated Sorting Genetic Algorithm (NSGA-II) [28] is used to solve the MOO problem to yield a non-dominated (or Pareto) set of optimal orthotropic wheel material properties. The cellular material optimization is conducted to find periodic unit cells which meet the optimal material properties while withstanding the imposed loading conditions. A verification of the two-step approach is performed by direct modelling of cellular wheel concepts. Coordination between the system and component level analyses is investigated through

an additional error analysis step. A discussion on the results, assumptions and applicability of the component level analysis for alternative wheel concepts is presented. A review of the research objectives accomplished, and the contributions of this research to the field of planetary surface mobility is given in Chapter 7. This thesis concludes with a discussion of limitations and proposed extensions of the wheel design methodology, as well as recommendations for future lunar rover wheel development.

CHAPTER 2

Literature Review

In this chapter, an overview of planetary surface exploration missions and rover designs is presented followed by a discussion on methods to evaluate mobility performance and a review of existing wheel designs and design methodologies. Section 2.2 introduces some structural, single and multi-objective optimization theory applicable to this work. Finally, this chapter concludes with a discussion on homogenization techniques for modelling lattice materials. Homogenization theory is used in Chapters 5 and 6 to model the mechanics of a cellular wheel design.

2.1 Planetary Surface Mobility

The mobility performance of planetary rovers is an essential consideration in the success of surface exploration missions. The performance of the Apollo LRV allowed Astronauts to explore a larger area of the lunar surface, return a variety of regolith samples and conduct more scientific experiments than on foot [7]. More recently, however, the importance of planetary mobility was demonstrated with Spirit's inability to traverse a very soft patch of Martian terrain-which proved to be the beginning of the end of the rover's mission life [55].

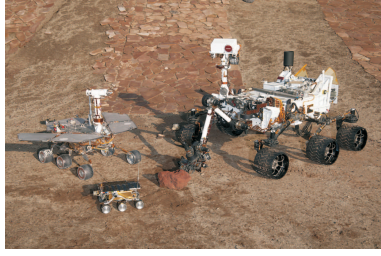
With renewed interest in returning to the Moon, international space agencies have undertaken the development of the next generation of lunar rovers as described in [117],[83] and [44]. Rovers will be used for a variety of surface mobility tasks, as

shown in Table 2–1 [33]. Figure 2.1 illustrates terrestrial prototypes of lunar rover concepts which satisfy a range of tasks outlined in Table 2–1.

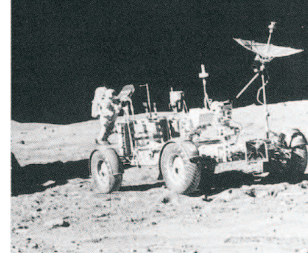
Table 2–1: Lunar rover missions as a function of lunar base development [33]

Development phase	Rover Type	Rover Tasks
Precursor	Autonomous or tele-operated.	Resource assessment, robotic surface surveys, robotic site preparation, sample return.
Pioneering	Autonomous, tele-operated and astronaut driven.	Lunar base site preparation, surface mining/lunar oxygen pilot plant, short-range surface transportation.
Consolidation	Pressurized crew driven, autonomous, remote-operated and astronaut driven.	Extended mining capabilities, lunar oxygen production, longer-range surface transportation.
Settlement	Pressurized crew driven, autonomous, remote-operated and astronaut driven.	Large-scale mining/oxygen production facilities, long-range surface exploration, tourism.

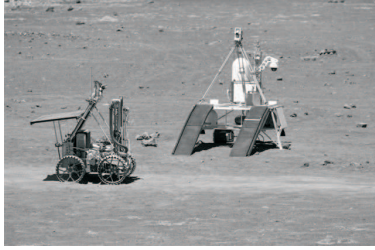
Broadly, the mobility system of planetary vehicles can be divided into: motors and drivetrain, traction system, steering mechanism and suspension system. The rover mobility system must be designed to meet the specific mission requirements. Autonomous or tele-operated rovers typically employ geometric suspension and explicit steering on multiple wheels to efficiently negotiate irregular and soft terrain at slow speeds [6]. The design of rovers driven by on-board astronauts will emphasize suspension and handling to accommodate higher driving speeds, such as the LRV [15].



(a) NASA Mars Rovers (NASA/JPL)



(b) Apollo LRV [19]



(c) Artemis Jr. Rover (Neptec Design Group)



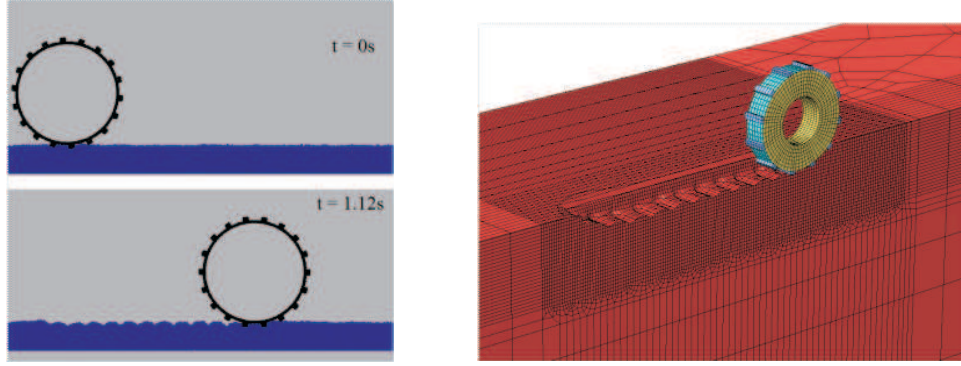
(d) NASA LER [44]

Figure 2.1: Planetary Rovers

Pressurized mobile habitats must provide life support for astronauts for long range missions [19] [33]. In all cases, however, the traction systems plays a critical role in rover mobility. The wheels, or tracks, must be designed to minimize sinkage into the regolith, provide sufficient traction for the vehicle to traverse soft soil and slopes, conform to surface irregularities, absorb shock, transmit torque and withstand the dynamic loading of the vehicle-terrain interaction [119].

2.1.1 Modelling and Testing Mobility Performance

Several approaches have been developed to model wheeled and tracked vehicles in soft soil. M.G. Bekker first introduced the field of terramechanics by developing a set of semi-empirical relationships which predict the available drawbar pull and motion resistance of traction systems in deformable soil according to the Mohr-Coulomb failure criterion [14] [13]. Janosi and Hanamoto presented a semi-empirical model



(a) Discrete Element Modelling [17] (b) Finite Element Modelling [89]

Figure 2.2: Numerical Modelling of Wheel-Soil Interaction

for plastic soils in [59]. J.Y. Wong [119] extended the semi-empirical formulations to include the effects of slip and wheel entry and exit angles. In [6] and [57], the semi-empirical approach was extended for a deformable wheel. Numerical approaches have also been proposed to study wheel-soil interaction; these include Finite Element (FEM) [126] [89] [76] and Discrete Element Methods (DEM) [68] [82] [75] illustrated in Figure 2.2.

Finite Element Analysis (FEA) can be used to model the soil as a continuum body with homogeneous properties. The deformation in a flexible wheel can be modelled more accurately in a FEA than in the semi-empirical approach. The dynamic nature and large displacements of the wheel-soil interaction can be captured using a time-integration in the Finite Element solver, namely explicit or implicit. Implicit FEA solves for displacements by inverting the stiffness matrix, whereas explicit FEA solves for accelerations by inverting the mass matrix [2]. Various material models have been introduced to capture the deformation of the soil under the motion of the wheel, including: the Mohr-Coulomb failure criterion, Drucker-Prager cap

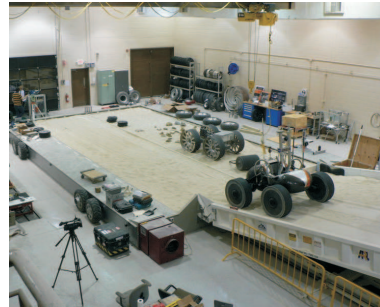
model and the Cam Clay critical-state model [119]. Soil compaction can be captured by pressure-dependent elasto-plastic material models, such as the modified Cam-clay and Drucker-Pracker with cap plasticity [30] [85]. Soil model parameters can be found experimentally through direct shear and pressure-plate soil testing [64]. Discrete element analysis provides a more accurate physical representation of the wheel-soil interaction as soil particles are modelled individually rather than as a continuum. However, virtual soil properties of the DEM must be calibrated to match the geotechnical properties of the appropriate soil [18]. Further, attempting to model individual soil particles becomes computationally expensive unless model calibration permits a reduction in particle quantity by increasing particle size [18].

Modelling tool accuracy is highly dependent on the geotechnical soil properties used in the model. These include the soil cohesion (C), soil internal angle of friction (ϕ) and soil bulk density (γ), and can be determined experimentally [21] [4]. Characterizing extraterrestrial soils is achieved by remote sensing, in-situ sensing and direct measurements [23]. Lunar regolith simulant have also been developed to replicate lunar wheel-soil mechanics on earth [84]. Extensive physical testing in controlled environments to validate modelling tools has been undertaken in [121], [68] and [11]. In [120] a parabolic test campaign was undertaken to investigate the effects of gravity on wheel-soil interaction. Figure 2.3 illustrates existing planetary analog single wheel and rover test facilities.

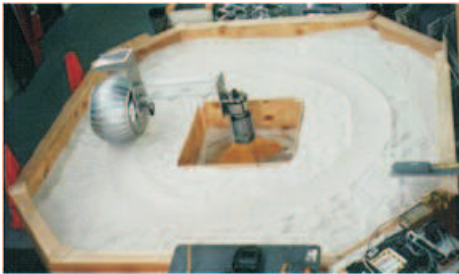
A challenge in conducting experimental testing is accurately measuring the mobility performance of the wheel. Typically, load cells, linear and rotational encoders allow



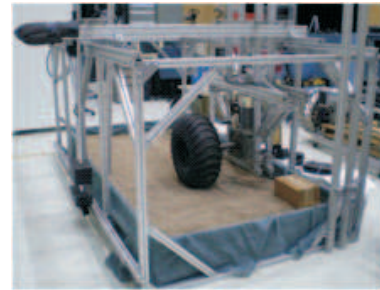
(a) Oerlikon ExoMars testing [80]



(b) NASA GRC Facilities [122]



(c) CMU single wheel test bed [6]



(d) McGill-CSA single wheel test bed

Figure 2.3: Planetary Analog Test Sites

for an accurate depiction of the tractive, torque, speed and slip metrics [106] [122]. In [5], three dimensional pose tracking was achieved using a camera system, which allowed for validation of a rover modelling tool. Accurately measuring sinkage over the entire length of the terrain can be challenging. In [80], a laser range finder was used to manually measure the sinkage at various points along the track. An average sinkage over the course of the wheel track is then computed. To verify the effect of multiple passes, however, single wheel testing is preferred over rover testing. This is due to the fact that the rover’s rear wheels will pass over the same track as the front wheels. In-situ sinkage measurements would be required to measure the multi-pass effect of wheels using a rover based testing method.

The terrainability of the rover, or the ability to negotiate terrain irregularities, is typically evaluated using a quasi-static approach, where semi-empirical terramechanics models are coupled with multi-body dynamics software [10] [109] [70]. In [8], a numerical soil model is formulated to be compatible with a multi-body dynamics (MBD) software. In [97], a MBD and wheel-soil simulation environment is developed for optimizing the locomotion system of planetary rovers. Multi-body dynamics software can be used to capture rover-terrain dynamics, however, rigid wheel assumptions are prevalent in planetary vehicle modelling. An approach to numerical modelling of the deformable soil, rover dynamics and flexible wheel is available in [96]

2.1.2 Existing Wheel Designs and Design Methodologies

Three wheels successfully rolled on the surface of the moon during the 1970s. To satisfy the requirements of three different vehicles, these wheels had significantly

different structural designs: the push cart of Apollo 14 used stiff rubber pneumatic tires, the Russian Lunakhod used a rigid spoke wheel while the LRV of Apollo 15, 16 and 17 used a compliant wire mesh wheel [7]. Additionally, a number of rigid and elastically compliant wheels, shown in Figure 2.5, were explored in the context of the LRV program as described in [7] and [15]. Flexible wheels are preferred as they allow for a smaller wheel to achieve similar traction as a larger rigid wheel. They offer promising obstacle negotiation capabilities, low ground pressure and sinkage, high traction and improved rider comfort [93].

More recent developments in non-pneumatic, non-rubber flexible wheels have shown promise for planetary exploration vehicle traction systems. Michelin and Goodyear Tire Company have investigated non-pneumatic compliant wheels for terrestrial and potentially extraterrestrial use. The Michelin wheel, aptly named the Tweel, uses a flexible spoke design working primarily in tension and a shear band to evenly distribute ground pressure to provide some added suspension and improved traction characteristics to the vehicle [93]; while the Goodyear lunar wheel uses 800 interwoven springs as a carcass to provide a highly elastic tire to conform to surface features [122]. Employing a flexible internal structure between the hub and outer rim, compliant wheels increase their effective rolling diameter. In the literature, the shape and size of the compliant spokes range from hoop springs [15] [56], flexible metallic carcasses [40] [7] [122] [43], staggered sine-wave spokes [86] [96] or individual cantilever-like beams mounted circumferentially about the wheel hub [39]. Individually mounted cantilever-like beam wheel concepts, as shown in 2.4(f), are dubbed segmented wheels in this work. Various periodic microstructures have been

investigated for the shear band component of the TWEEL design in [104]. It was demonstrated that cellular materials, namely regular and re-entrant honeycomb unit cells, offered low ground pressure at the wheel-soil interface [78]. It should also be noted that polyurethane honeycomb unit cells were investigated for the structural design of a terrestrial wheel in [62]. NASA’s Mars Exploration Rovers (MERs) Spirit and Opportunity utilize spoke compliance to improve obstacle negotiation-however, the outer rim is rigid limiting tractive performance. A novel class of non-elastic compliant wheels, dubbed iRings, has been developed at McGill University [90] which does not rely on the elastic properties of the structural elements of the material. This wheel is described in more detail in Chapter 5. A number of planetary rover wheel designs are provided in Figure 2.4.

Several approaches to the design and selection of wheel concepts have been proposed. During the Apollo program, wheel prototyping and testing, as well as engineering judgement was used to select and refine the wire-mesh wheel design. A summary of the comparison conducted in [15] is available in Figure 2.5.

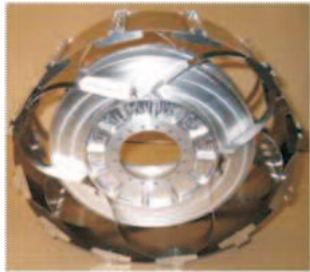
More recently, Patel [86] compared wheel prototypes experimentally over a subset of mobility performance metrics to select the *optimal* wheel for the ExoMars rover. In [78] and [62], a parametric approach to the design of hexagonal cellular wheels was undertaken. In both cases, however, the analysis was limited in scope. In [108] and [111], an optimization approach was employed to determine the optimal effective shear modulus of a homogeneous linear-elastic shear band material, shear band thickness and spoke thickness to reduce rolling resistance of TWEEL. To enable iterative objective function evaluations in the optimization problem, the rolling resistance



(a) Michelin TWEEL [117]



(b) Goodyear Spring Wheel [122]



(c) ESA ExoMars Wheel [86]



(d) NASA Mars Rover Wheels (NASA/JPL)



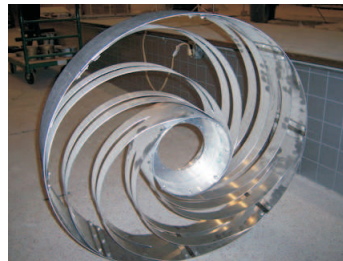
(e) McGill iRings Wheel



(f) ODG Wheel (ODG)






(g) CSA Wheel [40]



(h) NASA Spiral Wheel [106]

Figure 2.4: Recent Wheel Developments

Wheel type:		Rigid rim	Pneumatic	Wire mesh	Spiral spring	Hoop spring	Elliptical	Cone	Hobless
Example reference:		Gromov 2003	Goodyear 1969	GM 1970a	Markow 1963	Bendix 1965	Markow 1963	Grunman 1970	Lockheed 1972
Criteria	Method								
	Weighting factor								
	J 0.15	6.0	4.5	5.0	4.7	4.7	1.7	4.0	1.9
	C/E 0.14	3.8	7.3	7.3	8.7	8.7	8.2	8.3	8.7
	C 0.14	6.6	3.3	8.7	2.5	4.5	1.0	5.8	0.5
	J 0.13	0.0	8.0	9.0	3.0	5.0	6.0	2.0	3.0
	C 0.10	6.8	7.4	7.4	6.4	6.4	6.8	7.4	6.4
	J 0.08	8.0	7.0	7.0	2.8	5.7	4.3	7.0	2.8
	J 0.08	3.0	1.5	5.3	6.0	6.0	6.0	5.3	6.0
	J/E 0.06	7.3	5.8	5.8	2.0	2.0	4.1	6.6	2.0
Environmental compatibility		8.0	0.0	6.0	7.0	7.0	6.0	6.0	3.0
Development risk and cost		10	1.3	8.0	8.0	8.0	4.0	5.3	2.7
Total		Eliminated	Eliminated	7.1	5.0	5.8	4.7	5.6	3.8

Key : C – Calculation, E – Experiment, J – Engineering judgment

Figure 2.5: Lunar Wheel Development and Selection in the 1970s [7]

simulation was simplified by computing the ground pressure distribution beneath the wheel during a static FEA. Then, six hexagonal cellular structures with the optimal effective shear modulus and shear band thickness were modelled in an explicit FEA of the TWEEL rolling on deformable soil [78]. In [62], six polyurethane hexagonal cellular wheel spoke designs were selected to meet a target effective uni-axial elastic modulus, and were compared in a static FEA to evaluate ground pressure distribution and load carrying ability. A topology optimization of a non-pneumatic terrestrial tire with polyurethane spokes was performed in [58] to minimize the weighted compliance on two distinct loading conditions: vertical and tractive loading. However, the analysis used a linear-static FEA and neglected the large deformation of the polyurethane spokes in order to reduce the complexity of the optimization problem. Most recently, a systematic approach to the design of elastically compliant lunar wheels was proposed in [20]. This approach considered rover performance objectives by employing semi-empirical terramechanics models to find the suitable wheel diameter, width and vertical stiffness. Two distinct wheel concepts, a hoop and spiral spoke configuration, were investigated and refined using the FEM. Cardile [20] highlighted the importance in wheel concept selection and mobility performance requirements, however, ignored complex loading and the multi-objective nature of the wheel’s role in the rover and mission systems. Further, optimization was not considered in his analysis. Multi-objective optimization of terrestrial rubber pneumatic tires has been considered in [25] and [91] to improve maneuverability and durability performance. It should be noted, however, that terrestrial automotive tires have well defined performance requirements and design constraints. A multi-objective optimization approach to the

design of a four and six wheeled Martian rovers was been considered in [72] and [73] respectively. The optimization problem varied the suspension system linkage lengths, cross-sectional area and wheel dimensions to improve rover mass, power, accumulated sinkage, dynamic and static stability and driving efficiency. Several driving scenarios were identified, and objective functions were computed from the numerical simulations of a rover driving over soft and irregular terrain. A rigid wheel assumption was used in all cases.

To date, no systematic approach to the structural optimization of a compliant lunar wheel has been proposed. The analyses have been limited in scope, by employing parametric numerical or experimental investigations or neglecting the complex and dynamic loading of the wheel. Furthermore, only a subset of lunar mission relevant performance objectives have been addressed, and wheel concepts were developed for specific vehicles and applications in mind. It was demonstrated, however, that the size and shape of wheel structural components influences mobility performance. A multi-objective optimization approach provides a means to consider multiple performance objectives, and simplifying the periodic internal wheel structure as a homogeneous material provides a computationally efficient way to simulate wheel-soil interaction. As such, an overview of pertinent optimization and material modelling theory is presented next.

2.2 Optimization Theory

Optimization theory applicable to this research is introduced here, including: structural, single and multi-objective optimization. Although not considered explicitly in this research, multi-disciplinary optimization concepts are also discussed briefly in this section.

2.2.1 Structural Optimization and Compliant Mechanisms

Typically, structural design optimization problems involve finding the suitable structural form (i.e. shape, size and/or topology) of a component that minimizes mass while maintaining the stresses, strains and deflections below the allowable material limit [67]. With a known set of loading conditions and geometric constraints of simple structures, Mitchell developed a set of optimum structures of minimum mass and maximum stiffness from the mathematical solution of solid mechanics equations [92]. In particular, Mitchell presented an optimal cylindrical structure to withstand torsional loading. While his work does not consider the complex loading of a wheel-soil interaction, it provides insight into rigid lightweight wheel design or optimal spoke configuration.

In the case of a lunar wheel, however, mobility performance is improved with compliance of wheel structural components. Functional mechanical components which rely on the elastic deformation of material are typically called compliant mechanisms [60] [52]. Compliant mechanisms can be designed to maximize mean and mutual compliance [3] or achieve functional specifications such as mechanical advantage, geometrical advantage and work ratios [71]. Three models to describe the design problem of compliant mechanisms were proposed by Ananthasuresh [3]: force-deflection method,

spring model and the multi-criteria model [42]. The force-deflection model is similar to the design of stiff structures in structural optimization, where a prescribed displacement is desired given an input force. The spring model is a generalized model to describe the relationship between the work piece and compliant mechanism, where the stiffness of the spring is estimated by the elastic behaviour of the work piece. The multi-criteria model is characterized by the desired function of the mechanism to first deform and make contact with a work piece, then resist an output load exerted by the work piece after contact. This is formulated using multi-criteria which maximize the output displacement and minimize compliance under two separate loading conditions. The output displacement is quantified by the mutual potential strain energy (MPE) and compliance by strain energy (SE). MPE and SE can then be combined in a weighted sum to form a single objective optimization problem, or kept separate and solved as a multi-objective optimization problem.

Various systematic approaches have been developed to synthesize and design compliant mechanisms in terms of their size, shape and topology. In topology optimization, a component is modelled as a homogeneous continuum and the finite element method is used iteratively to solve for optimal material distribution to satisfy compliance requirements [16]. Alternatively, pseudo-rigid-body methods models compliant mechanism behaviour by a combination of rigid links and torsional springs [52]. Size and shape optimization problems lend themselves towards closed-form solutions of compliance equations derived from solid mechanics for simple geometries [77]. Finite element methods are required to determine the relationship between geometric design variables and elastic behaviour for more complex structures [52]. In all cases, the

optimal component is found through mathematical or numerical structural analysis which ensures it can withstand the imposed loading conditions while achieving the desired functionality.

2.2.2 Design Optimization

A design optimization problem is defined by finding the optimal design variables describing a component or system to satisfy some performance objective(s), subject to the boundaries and constraints of a well defined problem. The performance of the design is evaluated by the objective function, which can be a mathematical expression or a numerical simulation. Single objective optimization problems (SOO) involve minimizing or maximizing a single objective function, whereas multi-objective optimization (MOO) problems consider several conflicting objectives simultaneously. Multi-disciplinary optimization involves the simultaneous manipulation of design variables which strongly interact between disciplines [102]. MDO is widely investigated in the aerospace industry, where coupling between structural and aerodynamic performance of components is evident.

MDO methods are classified in the way the optimization problem is organized, how the models are coupled and how the overall optimization problem is solved [79]. Monolithic architectures describe MDO methods where one single optimization problem is solved and can be classified on the way feasibility between analyses is ensured [26], namely: all-at-once (AAO), individual discipline feasible (IDF) and multidisciplinary feasibility (MDF). In distributed approaches, complex systems are decomposed into multiple optimization problems [1]. Partitioning the problem into

separate analyses and coordinating between the analyses is a critical consideration in decomposition-based optimization. Both hierarchical and non-hierarchical approaches have been presented in [101], although hierarchical approaches facilitate optimization by separating analyses at different levels [69]. Classification of distributed architectures is based on how convergence properties of the partitioning strategies is addressed.

In MOO problems, no single feasible design exists which simultaneously optimizes all objective functions, but a set of alternative solutions with different trade-offs can be found. These solutions are called non-dominated solutions, or Pareto optimal, and require a decision by the designer to select the single most preferred solution. The preference of the designer can be used to classify the solution method of MOO problems into: no-preference methods, posteriori methods, a priori methods and interactive methods [27]. No-preference methods do not assume any information of the objectives and find one single Pareto optimal solution; posteriori methods use the information to iteratively generate a set of optimal solutions; a priori methods use the objective preference to find one preferred Pareto optimal solution, while interactive methods use the preference information progressively during the optimization process.

Closed-form optimization problems lend themselves well to gradient-based optimization algorithms, where the first and second derivatives of the objective functions can be found to satisfy optimality conditions. For non-linear programming problems, the Karush-Kuhn-Tucker conditions are solved which can account for both equality and inequality constraints. Gradient-based optimization approaches are based on

mathematical theory and convergence to an optimal solution is guaranteed. Approximation techniques exist to compute gradients and Hessians for non-linear problems. However, gradient-based optimization may converge to a local optimum. Evolutionary optimization (EO) algorithms use stochastic operators and therefore typically do not need gradient information. Further, EO's population-based approach searches a larger design space at each iteration which helps avoid converging to a local optimum. This also allows the algorithm to be easily run on parallel computers. However, as the approaches are stochastic and not based on mathematical theory, optimality cannot be ensured in the final solution(s). The effectiveness of evolutionary algorithms is greatly reduced for large optimization problems where many design variables exist. Nonetheless, EO's are well suited for non-smooth (or non-convex) optimization problems. Other heuristic derivative-free methods suited for non-convex problems have been proposed, which can also solve large-scale problems and provide some convergence properties, such as the Generalized Pattern Search (GPS) method. However, EO's, in particular Genetic Algorithms (GA's) are especially well suited for MOO problems where finding a wide spread of non-dominated solutions is desired.

2.3 Material Modelling

Homogenization techniques are used to improve computational efficiency of modelling periodic structures, such as composite or cellular materials. This is particularly relevant, as a cellular wheel is a promising design concept while modelling it is computationally expensive. This section presents an overview of cellular materials and

homogenization theory.

2.3.1 Cellular Materials

Cellular solids are composed of a combination of voids and solid material in an ordered or arbitrary pattern, which can be man-made or naturally occurring [45]. Naturally occurring cellular materials have multiple functions in nature as seen in bones, wood and cork. Stochastic cellular materials are dubbed foams, whereas lattice materials are periodic and hence characterized by ordered patterns of repeating unit cells. The advantage of such materials is that, with a variation in relative density, cellular topology, volume and base material, the macroscopic properties can be tailored to achieve a desired mechanical, thermal, filtration, electrical or other function [45] [100] [115] [37]. New ultralight materials, such as silica aerogels, carbon nanotube aerogels, metallic foams and polymer foams are useful for thermal insulation, battery electrodes, catalyst supports and acoustic, vibration and shock energy damping [95]. The optimization of cellular structures to match material stiffness of bones in implants has been investigated in [66]. The compliance of lattice materials have also been used in flexible non-pneumatic wheel designs as described previously. Cellular structures can be particularly advantageous, as wheel deformation is not limited to the linear-elastic range. Geometric and material non-linearities can be exploited through elastic buckling of the cell walls and base material selection: in [63] by shape memory alloy Nitinol and in [62] by polyurethane.

As such, many unit cell patterns have been investigated to achieve desirable properties and multiple functions. The effective mechanical properties of two dimensional

lattices such as square, circular, Kagomé, diamond, triangular and hexagonal periodic unit cells have been well characterized in [54], [116], [35] and [113]. Three dimensional lattice structures, including four cubic and nine archimedean polyhedral unit cells have also been investigated in [114]. Unit cell walls deform by either stretching or bending yielding different behaviour at the macroscopic scale [31]. Bending-dominated lattices have low nodal connectivity between the cell walls or struts, resulting in lower stiffness than stretching-dominated lattices [31]. Stretching-dominated has much higher nodal connectivity and therefore higher stiffness [31]. Cellular foams can be manufactured from liquid metal, solid metal in powdered form, metal vapour or gaseous metallic compounds, or from a metal ion solution [9]. Lattice materials require accurate methods to tessellate specific unit cell structures. Novel processes, such as electron beam melting (EBM), selective laser melting (SLM) or stereolithography apparatus (SLA) provide accurate, high quality and reliable methods to generate lattice materials with greater control of mechanical properties or graded structures [103] [114].

2.3.2 Homogenization of Lattice Materials

In the applications discussed previously, direct modelling of individual cells of a large structure would be cumbersome. Further, optimization of cellular structures requires that the structural model be solved iteratively. To reduce computational efforts, constitutive models have been developed such that the macroscopic properties of a large cellular structure can be found based on periodic unit cell parameters.

These models can be developed through closed-form expressions or numerical models.

Ashby and Gibson’s work in [45] proposed mathematical relationships between hexagonal honeycombs and their macroscopic mechanical properties by assuming cell walls flex like beams under a uniform macroscopic axial and shear stress. To develop constitutive models for more complex unit cell designs, alternative methods have been developed. Cellular micro-structures can be modelled as equivalent micro-polar medium [36], whereby the rotation and displacement of cell walls of the lattice can be found by the macroscopic displacement of the joints and microscopic rotation associated with the joint rotation. The structural analysis of a representative volume element (RVE) of the lattice or an energy approach, based on equating strain energies of the structure and micropolar continuum, are used to obtain macroscopic properties. Micro-polar theory has been used to characterize rectangular [12], square, triangular and regular hexagonal structures [22].

The Cauchy-Born hypothesis is another method which formulates microscopic lattice nodal deformations in terms of material macroscopic strain fields [53]. The macroscopic stiffness properties can then be derived. A limitation was shown for this method for pin-jointed micro-trusses in [35]. The stiffness matrix of stretching dominated micro-structure stiffness matrices are full rank, however, bending dominated structures are singular. The Cauchy-Born hypothesis was extended using a Dummy Node Scheme for arbitrary topologies in [35].

Asymptotic homogenization is a numeric approach based on the asymptotic expansion of field quantities on two length scales: macro (x) and micro (y) [51]. These

length scales are related through $y = x/\epsilon$, where ϵ relates the unit cell and structure dimensions. Asymptotic expansion allows for governing equations with oscillating coefficients to be substituted by the equivalent properties of the periodic material [49]. For simple unit cell designs, mathematical approaches can be used to solve for the macroscopic properties, however numerical approaches are required for more complex topologies [49].

Alternatively, the effective mechanical properties of a periodic structure can be solved directly from a FEA of a representative volume element (RVE) provided unified periodic boundary conditions are imposed and the mesh is identical at the boundaries [124] [110] [81]. For three dimensional lattices, six uni-axial loading conditions are imposed and the effective stiffness matrix of the lattice is found through the principle of superposition [123]. The relationship between macroscopic stress fields and the microscopic distribution within the RVE can also be found [51].

In [114], a general procedure based on a multi-scale approach is developed to find the macroscopic stiffness, internal forces and buckling loads for open and closed cells three dimensional lattices. Microscopic displacements of the RVE are expressed as a function of the macroscopic strain field, and the displacements are found by imposing equilibrium stiffness. The method presented in [114] can also be extended to account for both material and geometric non-linearities. For a cellular wheel concept where large deformations are desired, such a homogenization technique can capture elastic buckling of polymeric cellular materials.

2.4 Summary of Literature Review

This chapter presented an overview of the multi-disciplinary topics pertinent to the optimization of compliant lunar wheels. The design of planetary rovers was shown to be dependent on the intended function of the vehicle. In particular, the mobility and reliability performance of the vehicle is of prime interest for the success of lunar surface exploration missions. A number of methods to characterize the mobility performance were also introduced, with a focus on wheel-soil interaction.

Wheel compliance plays an important role in the mobility performance of the rover, as such, several flexible wheel concepts have been investigated in literature. However, no existing wheel concept has been shown to satisfy all rover or mission performance requirements. Coupling between the structural components of the wheel and wheel mobility performance is evident, yet trial and error prototyping and physical testing is still widely used in wheel development. Numerical or mathematical modelling of flexible wheels has been used primarily to evaluate the performance of existing wheel concepts. Parametric analysis and optimization of cellular wheels to improve ground pressure or vertical compliance have been found, however the studies were limited in scope and ignored complex wheel loading and mission performance requirements.

In sum, a systematic approach to the design and optimization of a flexible lunar wheel to improve rover mobility and ensure mission success is lacking. It is shown, however, that structural optimization can be used in the design of compliant mechanisms and multi-objective optimization allows for multiple performance criteria to be satisfied by a single design. Models exist that capture the wheel-soil interaction, which can be related to rover and mission performance metrics. Additionally, cellular

solids can achieve a wide range of properties through the design of its microstructure. Modelling individual periodic unit cells of a large component such as a wheel, however, is impractical. Homogenization theory simplifies the structural analysis by modelling the effective properties of lattice materials.

Subsequent chapters will develop a wheel design methodology, employing the concepts introduced in this chapter. It should be noted that although the design of a flexible wheel is a multi-disciplinary problem, the application of an MDO approach is considered out of scope of the current work. Future work in compliant wheel design optimization utilizing MDO methods is discussed in Chapter 7.

CHAPTER 3

Systematic Wheel Design Methodology

In this chapter, a framework for optimizing compliant lunar wheels is proposed. This framework is developed and verified in subsequent chapters.

3.1 Design Framework

Designing a flexible wheel is non-trivial given that it must satisfy multi-disciplinary performance criteria. As discussed in Chapter 2, lunar rovers have been proposed to conduct surface mission scenarios for various phases of lunar development. The wheel-soil interaction plays a critical role in the mobility performance of planetary rovers and therefore mission success. From a structural perspective, the wheel must deform while withstanding complex loading without failure.

To address the multi-level and multi-disciplinary nature of the problem, a two-step sequential optimization approach is proposed. The framework is partitioned into system and component level optimization problems, as well as a wheel concept development step. To simplify the analysis at the system level, the structural configuration of the wheel concept is ignored by employing a pseudo-model of an elastically compliant cylindrical wheel. At the component level, structural modelling of wheel concepts is considered via FEA. The framework, summarized in Figure 3.1, coordinates the system and component levels by system level design variables describing the elastic wheel pseudo-model. As this framework was developed for a generalized

approach to lunar wheel design optimization, wheel concept development is also considered. An error analysis step is included to verify the component level optimization results at the system level. It should be noted that the component level optimization depicted in Figure 3.1 is a generalized approach for arbitrary wheel concepts. The detailed component level design methodology is described for a cellular wheel concept in Section 3.4.

As described in Figure 3.1, at the system level, the optimal wheel design variables (\mathbf{x}_{sys}^*) are found which maximize rover (z_i) and mission (f_j) mobility performance metrics, using multi-disciplinary models (a_i, b_j) and parameters describing the environment (\mathbf{c}_{env}), mission ($\mathbf{c}_{mission}$) and rover design (\mathbf{c}_{rover}). The optimal wheel which satisfies the rover and mission objectives can be described as a set of concept independent wheel design variables. The design variables describing the elastic wheel pseudo-model are independent at the system-level.

Coordination between the component and system level optimization is achieved through \mathbf{x}_{sys}^* . A sub-set of \mathbf{x}_{sys}^* , dubbed the shared system design variables ($\mathbf{x}_{sys,s}^*$), constrain the shape and size of the wheel at the component level. The so-called local system design variables ($\mathbf{x}_{sys,l}$) describe the linear-elastic deformation of the wheel. At the component level, the relationship between component level design variables (\mathbf{x}_{comp}) and linear-elastic deformation is achieved through an explicit FEA of wheel-terrain interaction. Hence, the elastic behaviour $\mathbf{x}_{sys,l}$ of the wheel in the pseudo-model is approximated by a set k of component level performance metrics (y_k) computed numerically. To illustrate the conflicting nature of y_k in achieving $\mathbf{x}_{sys,l}^*$, multi-objective optimization is implemented at the component level. A method with

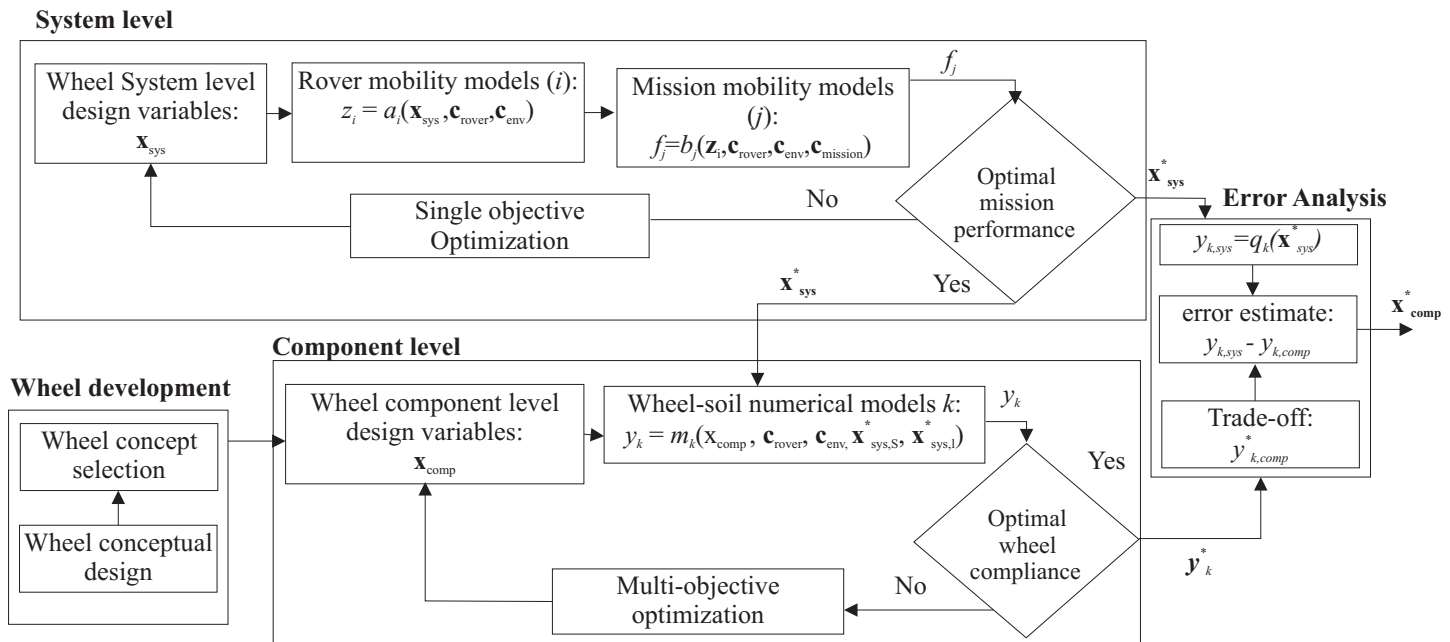


Figure 3.1: Wheel Design Framework

posteriori articulation of preference is used, such that a Pareto set of optimal wheel designs are found. Trade-off solutions (\mathbf{x}_{comp}^*) are selected, and the effectiveness of the design approach can be verified by estimating the error between $y_{k,comp}$ and \mathbf{x}_{sys}^* using coupling models q_k . This error analysis step is conducted outside the optimization framework, such that convergence between the system and component levels is not addressed in this research. With additional knowledge of a specific wheel concept, mission scenario and rover design, the convergence between system and component level results can be addressed through a design framework based on multi-disciplinary optimization theory. This is proposed as future in Chapter 7.

By employing a multi-step approach, the surface exploration vehicle performance is directly related to elastic wheel behaviour, independent of the wheel design concept. Then, optimizing a wheel to accomplish the required performance can be conducted in a secondary step, using a defined wheel concept at the component level. The methodology is applicable to various wheel concepts and gives insight into optimal elastic wheel design for planetary exploration missions. Subsequent sections in this chapter provide more details of the system level optimization, wheel concept development activities and component level optimization.

3.2 System Level Optimization

The objective of the system level analysis is to investigate the importance of the wheel on rover (z_i) and mission performance (f_j) metrics, and determine the values of the optimal wheel system design variables (\mathbf{x}_{sys}^*) which describe linear-elastic behaviour, regardless of the wheel concept. To accomplish this, the wheel is described

by a linear-elastic pseudo-model parameterized by system level design variables \mathbf{x}_{sys} compatible with closed-form rover (a_i) and mission mobility (b_j) models. The models are multi-disciplinary, addressing the rover terramechanics, steering and dynamics which in turn affect the energy, power and excavation capabilities of the rover. The system level analysis is described in more detail in Figure 3.2. The performance metrics (f_j, z_i) are discussed in more detail in Chapter 4.

The scenario, rover and environmental parameters are described by $\mathbf{c}_{mission}$, \mathbf{c}_{rover} and \mathbf{c}_{env} respectively. In this work, two rover mission are investigated: a resource prospecting and berm building scenario. These missions are of interest for lunar surface exploration and early lunar infrastructure development. The system level optimization problem is formulated and solved for a set of user-defined mission priorities. Since detailed mission architecture and requirements are unavailable, the mission priorities are selected to highlight the importance of the wheel at the system level. The system level optimization is presented in Chapter 4.

3.3 Wheel Concept Development and Selection

A consequence of the proposed approach is that although optimal elastic wheel design can be found via the system level analysis, selection and parameterization of a wheel concept is required to perform the component level analysis. Selecting a wheel concept will impose constraints on the design space and variable dependence, and thus can limit the optimal system level performance. As such, a thorough review of wheel concepts is necessary to select a promising wheel concept for the component level analysis. This is conducted by reviewing ongoing wheel development activities,

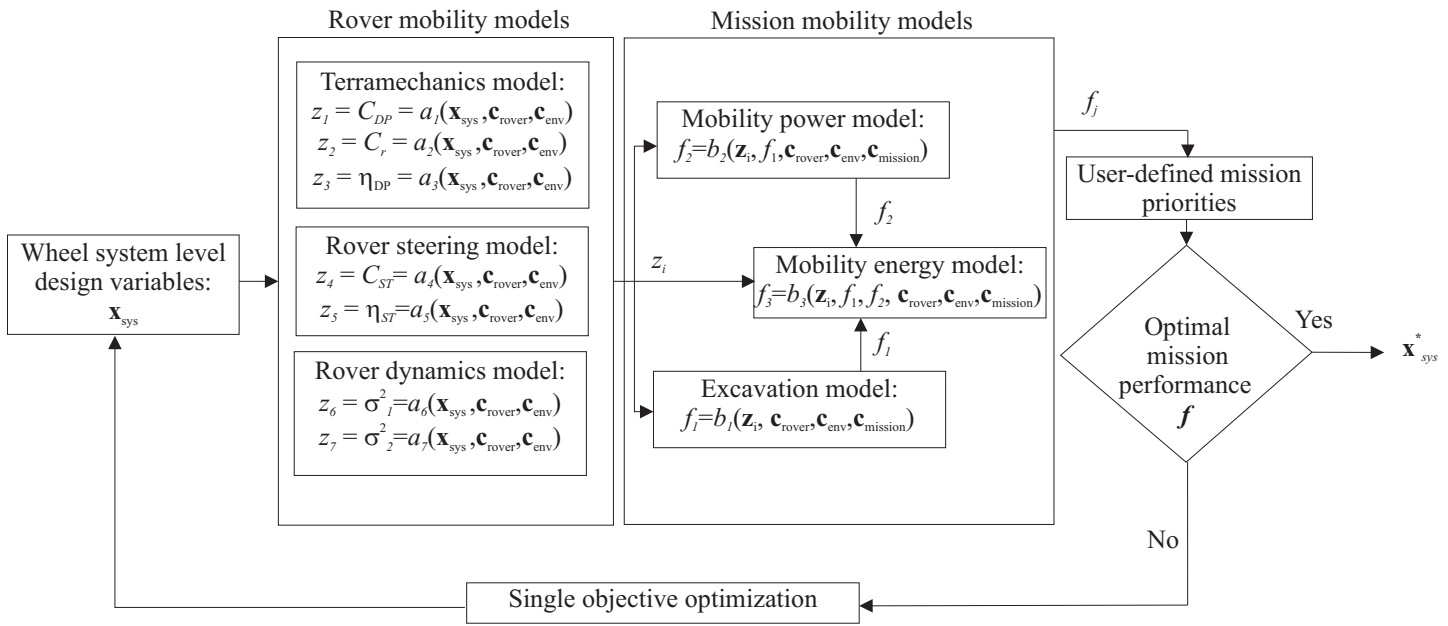


Figure 3.2: Wheel System Level Analysis

prototyping, testing and investigating wheel concepts through numerical modelling in Chapter 5. It should be noted that imposing variable dependence and constraints at the system level will ensure that the optimal system performance is feasible. However, the dependence of the elastic wheel design variables can only be found through a structural model of a wheel concept. This is conducted at the component level analysis. Additionally, a goal of this work is to recommend optimal elastic wheel design, irrespective of wheel concepts, in order to guide future wheel development activities.

3.4 Component Level Optimization

The component level optimization presented in Figure 3.1 is formulated for arbitrary wheel concepts. Although preliminary component level optimization of a segmented wheel concept was performed, as discussed in Chapter 5, a cellular wheel is selected to develop the wheel optimization framework. This section presents the details of the cellular wheel component level optimization which is performed in Chapter 6.

The objective of the component level analysis is to target wheel system variables (\mathbf{x}_{sys}) and evaluate wheel reliability performance by structural analysis of the wheel concept. For the cellular wheel concept, the component level analysis is separated into two scales: macroscopic and microscopic. At the macroscopic scale, the cellular wheel is modelled using a linear-elastic homogeneous material, described by the effective material stiffness $\bar{\mathbf{K}}$ and relative density $\bar{\rho}$, in dynamic FEAs of two driving scenarios. The component level objectives y_k are defined based on the elastic wheel

pseudo-model. More specifically, the vertical, torsional and lateral stiffness are considered independent at the system level, whereas they are linked by the material and structural topology of the wheel concept. Due to the nature of the dynamic loading conditions in the component level, the wheel effective vertical, torsional and lateral stiffness are approximated by the average contact area, peak torsional displacement and peak lateral displacement found in the explicit wheel FEAs. To improve computational efficiency, the ground is modelled as rigid in the FEA. As such, coordination between component and system analysis is approximated by coupling models q_k . Given the conflicting nature of y_k , an MOO approach is used. A set of trade-off solutions from the Pareto front are selected for further investigation at the microscopic scale, and verification at the system level.

At the microscopic scale, a cellular material optimization problem is solved to find feasible cellular materials $(\mathbf{x}_{top}, \mathbf{x}_{mat}, \mathbf{x}_{cell})$ which minimize error e_s between homogeneous wheel material properties $\bar{\mathbf{K}}^*$ and cellular material effective properties $\bar{\mathbf{K}}_{cell}$. This is achieved by using closed-form expressions of the material constitutive models. The feasibility is verified by the constraints vector \mathbf{g} to ensure buckling and plastic deformation does not occur in the cell walls. Error analysis to compute the error between cellular wheels composed of feasible unit cell topologies $y_{k,feasible}^*$ and optimal effective materials y_k^* is achieved by direct modelling the cellular wheel in the FEA. The component level optimization framework is illustrated in Figure 3.3.

Alternatively, the component level optimization can be combined into a single step, where cellular material feasibility is ensured by using constitutive models within the wheel MOO feedback loop. This would require a cellular topology to be selected a

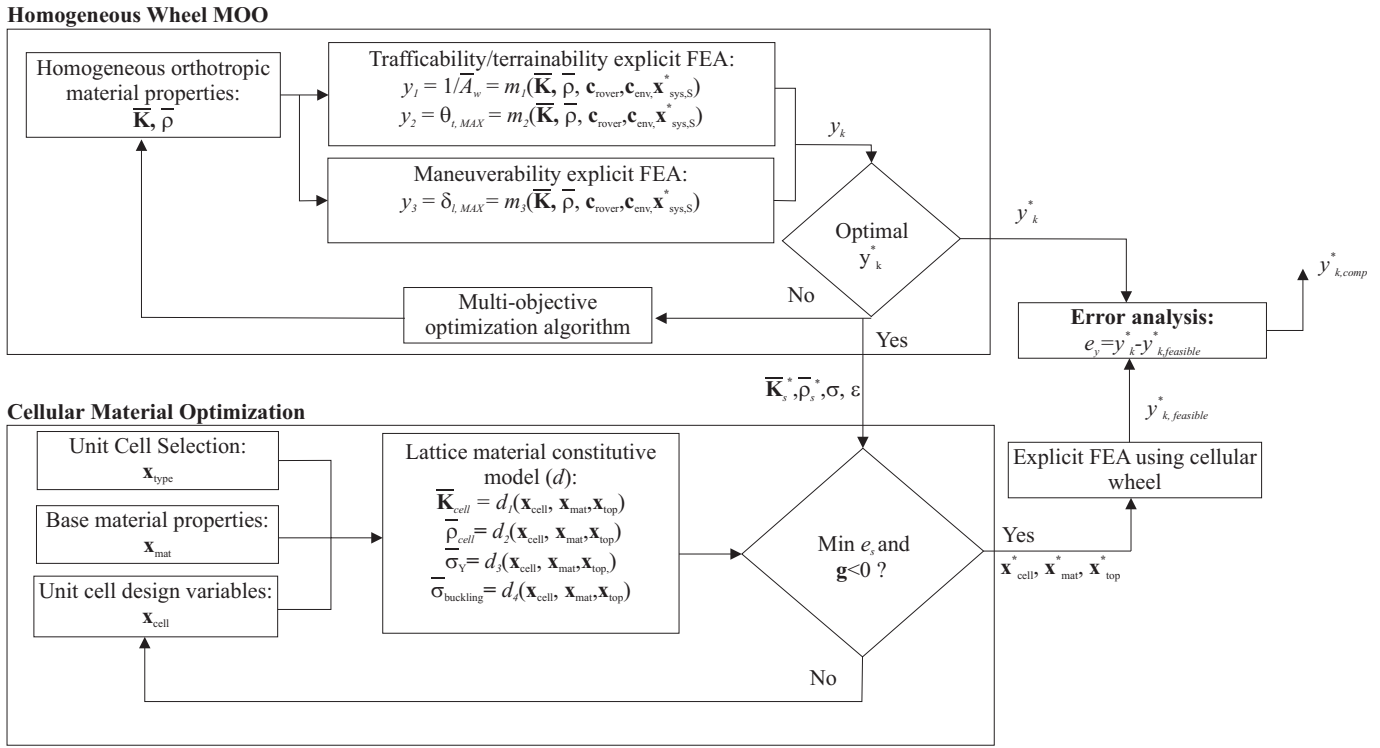


Figure 3.3: Component Level Optimization Framework

priori for each MOO simulation. Given the computational effort required to solve the MOO, running multiple simulations for various cell topologies of interest would be time consuming. Additionally, the posteriori approach provides insight into the optimal effective linear-elastic material properties of the wheel first without limiting the design space, which can be useful in guiding non-cellular wheel designs as well. Further, a thorough search of all available unit cell designs is out of the scope of this research and only a limited subset of promising unit cells are investigated herein. Therefore, finding optimal three dimensional material properties through the homogeneous wheel MOO enables future work to more thoroughly investigate optimal cellular wheel topologies.

CHAPTER 4

System Level Optimization

This chapter begins by proposing and classifying an inclusive set of mission and rover mobility performance metrics, followed by a description of the mathematical models used to evaluate them. System level optimization problems are formulated for two lunar rover missions: a resource prospecting and berm building scenario. For each mission scenario, \mathbf{x}_{sys}^* is found for different mission priorities. A parametric analysis of wheel system variables \mathbf{x}_{sys} with respect to rover performance metrics z_i and mission performance metrics f_j was performed as well, but is included in Appendix A for conciseness.

4.1 Performance Metrics for Planetary Exploration Vehicles

To quantify the performance of lunar rover wheels, it is necessary to develop a set of performance metrics for planetary exploration vehicles. The performance metrics for planetary exploration vehicles was first introduced by Bekker [15] to select the optimal wheel for the Lunar Roving Vehicle. These metrics and associated importance, illustrated in Figure 2.5, were specific to the Apollo 15, 16 and 17 missions and LRV design. In Bekker's analysis, mechanical reliability, weight, soft ground performance and ride comfort were weighted importantly. This was due to the relatively short sortie missions, low travel distances, high driving speeds and importance of astronaut safety. Robotic missions will place more importance on steerability,

stability, environmental compatibility and wear resistance given the longer mission duration and navigation requirements for autonomous operation. Bekker's approach favoured qualitative measures of performance through extensive physical testing and prototyping, as well as engineering judgement to select optimal wheel designs.

In [6], Apostolopoulos identified three indices of performance to synthesize robotic vehicle configurations and optimize them for improved locomotion. He proposed analytical relationships to compute the trafficability, maneuverability and terrainability performance of the vehicle. Trafficability is defined as the robot's ability to traverse soft soils or hard ground without the loss of traction; maneuverability addresses the robot's ability to navigate through an environment; and terrainability captures its ability to negotiate terrain irregularities [6]. His framework emphasized closed-form relationships and neglected the numerically computed metrics related to vehicle-terrain interaction or mechanical reliability. Apostolopoulos's framework is extended by the system level analysis presented in Figure 3.2 to accommodate planetary vehicle and mission performance metrics.

Wong outlines the performance and ride characteristics of off-road terrestrial vehicles in [119]. The performance is evaluated by criteria depending on the function of the vehicle. For example, tractors require a high drawbar pull whereas military vehicles favour maximizing speed between two points of interest in a random environment. Broadly, however, mobility over unprepared terrain is the defining criterion for off-road vehicles. He defines this as the vehicle performance in soft terrain, obstacle negotiation and avoidance, ride quality over rough terrain and water crossing.

In an attempt to define a comprehensive list of planetary exploration vehicle performance metrics, the metrics proposed by Bekker [15], Apostolopoulos [6], Wong [119] and others [34] [105] identified through this research are listed in Table 4–1. It should be noted that redundant metrics or those irrelevant to planetary exploration were eliminated. In some instances, the metric nomenclature was adapted to suit planetary exploration vehicles. Table 4–1 includes a classification of the performance criteria.

The metrics presented in Table 4–1 are exhaustive. At the system level, the rover performance metrics are limited to trafficability, maneuverability and terrainability. Reliability performance assessment requires further knowledge of wheel structural configuration. This is addressed further in Chapter 6. Mission compatibility metrics are used here to constrain the system level design variables and identify mission success criterion such as total mission duration, driving distance, power or energy consumption. Environmental compatibility becomes important when selecting materials for wheel designs.

4.2 Multi-Disciplinary Performance Models

Wheel system design variables \mathbf{x}_{sys} relate to rover mission performance metrics f_j through the rover performance metrics z_i , as shown in Figure 3.2. The multi-disciplinary mathematical models for rover (a_i) and missions (b_j) are presented in this section, as well as a description of the system level design variables.

Table 4–1: Surface Exploration Vehicle Performance Metrics

Performance Category	Metric
Trafficability	Drawbar pull
	Motion Resistance
	Sinkage
	Maximum Gradient
	Maximum Speed
	Slip
	Drive Torque
	Driving/Tractive Efficiency
	Drive Resolution/Accuracy
	Traction Controllability
Maneuverability	Minimum Turning Distance
	Minimum Turning Radii
	Steering Resistance
	Turning Efficiency
	Steering Accuracy
Terrainability (quasi-static)	Maximum Surmountable Discrete Obstacle
	Maximum Roll-Over Angle
	Obstacle Climbing Resistance
Terrainability (dynamic)	Ride Comfort
	Road Holding Ability
	Suspension Travel
Reliability	Maximum Static and Dynamic Load
	Wear Resistance
	Lifetime
	Mean Time To Failure
	Mean Time To Repair
Mission compatibility	Mechanical Complexity
	Volume
	Mass
	Vibration Limits
	Power Limitation
Environmental compatibility	Operational Limitations
	Radiation Sensitivity
	Operating Temperature

4.2.1 Elastically Compliant Wheel Pseudo-model

A pseudo-model of a linear-elastic wheel which ignores wheel internal structure is used at the system level. The outer shape of the wheel, however, is important in determining the contact area with the soil. Three wheel shapes can be considered: spherical, toroidal and cylindrical. These wheel types result in two contact patch types: elliptical and rectangular [6]. The contact area with the ground can be approximated knowing the ground contact length (L_w) and width (b_w) [6]:

$$A_{ellipse} = \frac{\pi}{4} L_w b_w \quad (4.1)$$

$$A_{rectangular} = L_w b_w \quad (4.2)$$

In this work, a cylindrical wheel is assumed and therefore only Equation (4.2) is used. The pseudo-model considers the wheel to have a smooth continuous circumferential tread surface, and an internal wheel structure which behaves as a linear elastic spring with stiffness K_V that deforms vertically under an applied static load (W_w). The wheel vertical deflection (δ_w) can be found by Hooke's law as shown below.

$$\delta_w = W_w / K_V \quad (4.3)$$

Similarly, assuming a continuous outer surface, the lateral (δ_L) and torsional deflections (θ_T) can be computed knowing the lateral (K_L) and torsional stiffnesses (K_T), applied torque (T_w) and lateral resistance (R_L) as:

$$\delta_L = R_L / K_L \quad (4.4)$$

$$\theta_w = T_w / K_T \quad (4.5)$$

The undeformed wheel width (b_w), diameter (D_w) and hub diameter (D_h) are also required to fully describe the wheel. Defining the hub diameter creates a vertical deformation limit on the wheel, alternatively this can also represent a mechanical bumper.

The set of system level wheel design variables \mathbf{x}_{sys} used to describe the elastically compliant wheel pseudo-model are shown in Equation (4.6). The sliding friction coefficient (μ_s) between the wheel and soil is included in Equation (4.6) which is used by the simplified rover steering model. Wheel dynamic rolling stiffness (K_D) and dampening (C_D), which are described in more detail in the simplified rover dynamics model, are also included in \mathbf{x}_{sys} .

$$\mathbf{x}_{sys} = [D_w, b_w, D_h, K_V, K_T, K_L, K_D, C_D, \mu_s]^T \quad (4.6)$$

It should be reiterated that dependence between system level design variables is not considered at the system level analysis. Structural modelling of wheel concepts is required to establish such relationships, which is addressed in the component level analysis in Chapter 6.

4.2.2 Terramechanics Model

A semi-empirical terramechanics model is preferred here to due to its simplicity and applicability for a concept independent wheel. The parameters of interest in the deformable wheel-soil model are depicted in Figure 4.1.

From Figure 4.1, the contact length of the wheel (L_w) can be found as [57]:

$$L_w = 2\sqrt{D_w\delta_w - \delta_w^2} \quad (4.7)$$

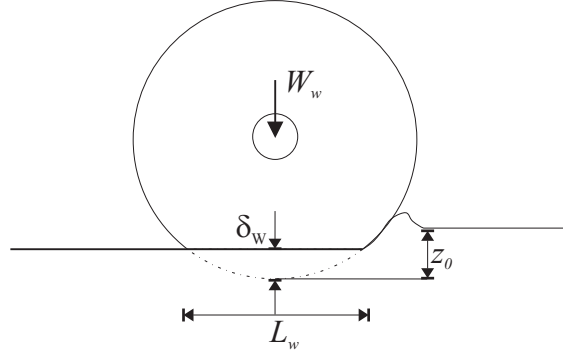


Figure 4.1: Deformable Wheel-Soil Model

Although Equation (4.7) is used to compute the contact length of the wheel, alternative methods to estimate the contact length of a deformable wheel are found in [6]. Sinkage (z_0), traction (H) and motion resistances (R_w) in [118] are found as:

$$z_0 = \left[\frac{W_w/A}{\left(\frac{k_c}{L_w}\right) + k_\phi} \right]^{1/n} \quad (4.8)$$

$$H = AC + W_w \tan \phi (1 - e^{\frac{SL_w}{k}}) \quad (4.9)$$

$$R_w = R_c + R_b + R_{slope} + R_{obstacle} + R_{st} \quad (4.10)$$

where k_c , k_ϕ , k , C , ϕ and S are the modulus of cohesion of soil deformation, modulus of friction of soil deformation, the coefficient of soil deformation due to sinkage, soil cohesion, internal angle of friction and the wheel slip respectively. The motion resistance due to terrain slope is computed by:

$$R_{slope} = W_{rover} g \sin \theta \quad (4.11)$$

Closed-form expressions have been proposed to compute the resistance caused by surmounting an obstacle at low speeds [6]. However, these models do not consider wheel compliance. $R_{obstacle}$ is ignored in the system level analysis. It should be noted, however, that passing over obstacles at high speeds is considered in the rover dynamics model described in Section 4.2.4. The steering resistance (R_{st}) is addressed in Section 4.2.3. The compaction resistance (R_c) caused by wheel sinkage can be computed as follows [118]:

$$R_c = b_w \left(\frac{k_c}{L_w} + k_\phi \right) \left(\frac{z_0^{n+1}}{(n+1)} \right) \quad (4.12)$$

Bulldozing resistance (R_b) comes from pushing of soil in front of a wheel. Bulldozing resistance is described in [118] as:

$$R_b = \frac{b \sin((\alpha + \phi))}{(2 \sin \alpha \cos \phi)} (2z_0 C_0 k_c + \gamma z_0^2 k_\gamma) + \left(\frac{\pi \gamma l_0^2 (90 - \phi)}{540} + \left(\frac{\pi C_0 l_0^2}{180} + C_0 l_0^2 \tan(45 + \phi/2) \right) \right) \quad (4.13)$$

where the modulus of density of soil deformation (k_γ) is found as:

$$k_\gamma = \left(\frac{2N_\gamma}{\tan \phi} + 1 \right) \cos^2 \phi; \quad (4.14)$$

N_γ is the coefficient of passive earth pressure, γ is soil density, l_0 is the distance of rupture computed as:

$$l_0 = z \tan \left(45 - \frac{\phi}{2} \right)^2 \quad (4.15)$$

and α is

$$\alpha = \cos^{-1} \left(1 - \frac{2z_0}{d} \right) \quad (4.16)$$

The dimensionless coefficients for tractive effort (C_{DP}) and rolling resistance (C_r) can now be found respectively through [119]:

$$z_1 = C_{DP} = \frac{DP}{W_w} = \frac{H - R_w}{W_w} \quad (4.17)$$

$$z_2 = C_r = \frac{R_w}{W_w} \quad (4.18)$$

The tractive efficiency metric (n_d) is computed as the ratio of output (E_{out}) to input energy (E_{in}) to drive the wheel:

$$z_3 = \eta_d = \frac{E_{out}}{E_{in}} = \frac{(T_w(1 - s)\omega) - E_v - E_T}{T_w\omega} \quad (4.19)$$

where s is wheel slip, ω is wheel rotational velocity, and wheel torque (T_w), vertical (E_v) and torsional (E_T) energy losses are found respectively through:

$$T_w = \frac{R_r D_w}{2} \quad (4.20)$$

$$E_v = \left(T_w - R_r \left(\frac{D_w}{2} - \delta_w \right) \right) \omega \quad (4.21)$$

$$E_T = \frac{(R_w(0.5D_w - \delta_w))^2}{2K_T} \quad (4.22)$$

4.2.3 Rover Steering Model

The steering resistance (R_{st}), steering efficiency (η_{st}) and minimum turning radius are dependent on steering system design, such as independent, coupled, articulated or skid steering [6]. The relationship between steering resistance and wheel design variables can be found through kinematic relationships and soil properties. The mathematical model used in this analysis considers skid-steering as it also imposes the highest lateral loads on rover traction system.

For steady-state turning at low velocities, the sum of the motion resistances and tractive forces must be equal as shown in Equation (4.23), where N is the number of wheels. The parameters relevant to a turning maneuver on a skid-steer vehicle are depicted in Figure 4.2.

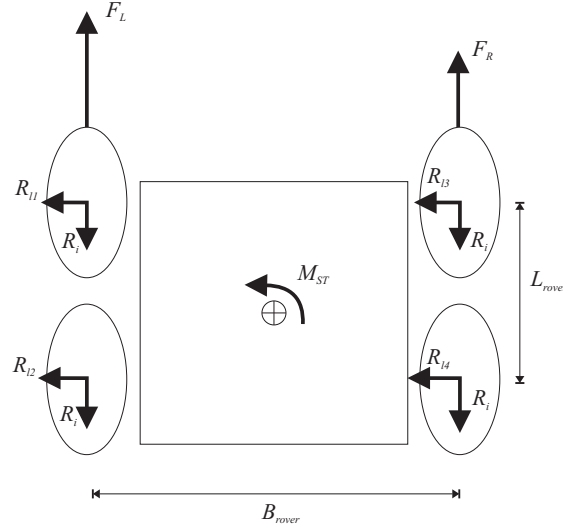


Figure 4.2: Rover Skid-Steer Model

$$F_R + F_L \geq \sum_{i=1}^N R_{C,i} + R_{b,i} \quad (4.23)$$

where the forward motion resistances at each wheel i can be found from the coefficient of rolling resistance C_r :

$$R_{Ci} + R_{bi} = C_r(c_i W_{rover}) \quad (4.24)$$

C_r was computed in Equation (4.18) and the vehicle load (W_{rover}) distribution on the wheels is accounted for by the coefficient c_i :

$$\sum_{i=1}^N c_i = 1 \quad (4.25)$$

The moment of steering resistance M_{st} , which consists of the sum of lateral motion resistances (F_L) about the centre of gravity of the rover, must equal the total tractive forces about the same point as shown here:

$$M_{st} = \frac{B_{rover}}{2}(F_R - F_L) = \sum_{i=1}^N R_{L,i} \frac{L_{rover}}{2} \quad (4.26)$$

The lateral motion resistance on wheel i ($R_{L,i}$) is computed below, as shown in [119]:

$$R_{Li} = \mu_s(c_i W_{rover}) \quad (4.27)$$

where μ_s represents the coefficient of lateral resistance. A range of values for μ_s for various materials and soil type is available Table 4-2.

Table 4-2: Material-Soil lateral sliding coefficients [119]

Material	Concrete	Hard Ground	Grass
Steel	0.50-0.51	0.55-0.58	0.87-1.11
Rubber	0.90-0.91	0.65-0.66	0.67-1.14

A more accurate value of μ_s can be computed with knowledge of the wheel design, so that bulldozing resistances occurring along the lateral side of the wheel can be found. From Equations (4.26) and (4.27), the additional rolling resistances at wheel i caused by M_{st} becomes:

$$R_{st,i} = \frac{\mu_s c_i W_{rover} (L_{rover}/2)}{N \frac{B_{rover}}{2}} \quad (4.28)$$

The coefficient of steering resistance C_{st} can now be found as:

$$z_4 = C_{st} = C_r + \frac{R_{st,i}}{W_w} \quad (4.29)$$

The turning efficiency of the skid steer maneuver is computed, as in driving efficiency, as the ratio of the output energy (E_{out}) to input energy (E_{in}) to complete the turn, as shown below.

$$z_5 = \eta_{st} = \frac{([T_w(1-s)\omega] - E_v - E_T - E_L)}{T_w\omega} \quad (4.30)$$

The energy loss due to lateral deformation (E_L) can now be computed using:

$$E_L = \frac{R_L^2}{2K_L} \quad (4.31)$$

4.2.4 Simplified Rover Dynamics Model

A simplified quarter-car model of the vehicle and wheel is used here to analyse the response of the vehicle when travelling at a constant speed over irregular terrain [47] [112] [74]. Higher fidelity numerical models require additional knowledge of the terrain, vehicle and wheel designs. In the elastically compliant wheel pseudo-model, the wheel is simplified as a linear-spring damper system which ignores the rover suspension system in Figure 4.3.

The excitation of the system is caused by the constant forward velocity (v) of the vehicle and the surface elevation profile (ζ). The suspension system of the rover is neglected to represent the design of CSA's Juno-II [61] and Artemis Jr. rovers. The single degree-of-freedom (DoF) equation of motion for the wheel is given by:

$$m_w \ddot{Z} + C_D \dot{Z} + K_D(Z - \zeta) = 0 \quad (4.32)$$

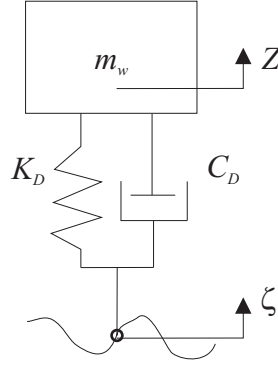


Figure 4.3: Simplified rover dynamics model

Ride comfort and road handling are measured by vehicle vertical acceleration (\ddot{Z}) and normal force acting on the ground (F_Z). Suspension travel, also described as a performance metric in Table 4–1, is restricted in this model to wheel deformation. In this case, it is directly related to F_Z through Hooke’s law. According to [47] and [46] both ride comfort and road holding performance are computed by finding the standard deviation of \ddot{Z} and F_Z . For ride comfort, the higher the standard deviation, the higher the discomfort. Similarly, for road holding a higher standard deviation of wheel radial force will lead to poor handling ability due to the loss of contact with the ground. From Equation (4.32), the response of the system is found for both \ddot{Z} and F_Z below:

$$H_1(j\omega) = \frac{\ddot{Z}(j\omega)}{\zeta(j\omega)} = \frac{-\omega^2 K_D}{m_w(j\omega)^2 + C_D(j\omega) + K_D} \quad (4.33)$$

$$H_2(j\omega) = \frac{F_Z}{\zeta(j\omega)} = \frac{-m_w\omega^2 K_D + (j\omega)K_D}{m_w(j\omega)^2 + C_D(j\omega) + K_D} \quad (4.34)$$

The imposed displacement, or road irregularity (ζ), can be represented by a random variable defined by a stationary and ergodic stochastic process with zero mean value

[119] [125]. The power spectral density (PSD), S_ζ , of the process is formulated as:

$$S_\zeta = \frac{G_0}{v^{N_S-1}\omega^{N_S}} \quad (4.35)$$

The values of used in the PSD function in Equation (4.35) are based on experimental measurements, where G_0 is the roughness constant (in $m^2/cycles/m$), v is vehicle velocity (in m/s), N_S is the slope constant and ω is the circular frequency (in rad/s). Some typical terrain roughness parameters are provided in Table 4–3, which are statistical terrain properties found experimentally. It should be noted that the terrain is modelled as non-deformable, which is not the case for lunar soil. More complex terrain modelling would be required to accurately model the dampening effects of a deformable soil.

Table 4–3: Terrain Roughness Parameters [94] [98]

Terrain type	G_0	N_S
Rough mare	0.000835	2
Smooth mare	0.00036	2
Hummocky upland	0.00003	2

For $l = 1, 2$, the PSD of the output of an asymptotically stable system (S_l) can be computed as:

$$S_l(j\omega) = |H_l(j\omega)|^2 S_\zeta(j\omega) \quad (4.36)$$

where $l = 1$ represents the PSD output for vertical acceleration (\ddot{Z}) and $l = 2$ represents the PSD output of the wheel radial force (F_z).

By definition, the variance of a random variable described by a stationary ergodic

process is given by:

$$\sigma_l^2 = \frac{1}{2\pi} \int_{-\infty}^{+\infty} S_l(j\omega) d\omega = \frac{1}{2\pi} \int_{-\infty}^{+\infty} |H_l(j\omega)|^2 S_\zeta(j\omega) d\omega \quad (4.37)$$

As shown in [87], if the transfer function is in the form:

$$H(j\omega) = \frac{(j\omega)B_1 + B_0}{-\omega^2 A_2 + (j\omega)A_1 + A_0} \quad (4.38)$$

then the closed-form solution can be found as:

$$\int_{-\infty}^{+\infty} |H_l(j\omega)|^2 d\omega = \pi \left(\frac{\frac{B_0^2}{A_0} A_2 + B_1^2}{A_1 A_2} \right) \quad (4.39)$$

Inserting Equations (4.33) and (4.34) into Equation (4.37) and manipulating to resemble the format of Equation (4.38), the closed-form expressions for both ride comfort and road holding can be written respectively as:

$$z_6 = \sigma_1^2 = \frac{G_0 K_D}{2m_w C_D} \quad (4.40)$$

$$z_7 = \sigma_2^2 = \frac{G_0 (C_D^2 + 3m_w K_D - 2m_w K_D)}{C_D K_D} \quad (4.41)$$

4.2.5 Mission Performance Models

To find optimal wheel designs for two mission scenarios describing a resource exploration and berm building mission, metrics expressing the available power, mission duration and driving distance are of interest. The metrics are quantified by mobility power (b_2), energy (b_3) and excavation (b_1) models described in this section, along with a set of environmental (\mathbf{c}_{env}), rover (\mathbf{c}_{rover}) and mission ($\mathbf{c}_{mission}$) parameters.

Mobility Power and Energy Models

Mobility power requirements of a mission concept can be estimated by knowing the required wheel torque (T_w) and rotational speed (ω). Although drivetrain, motor and motor controller design are ignored here, an estimate of mechanical power required to drive the rover can still be found. This formulation neglects the dynamic nature of the wheel-soil interaction by assuming a constant slip. Nonetheless, the computation of power is consistent throughout this analysis allowing for a qualitative comparison of the mobility power. Further, energy losses from driving over irregular terrain are ignored as the rover drives at low speed for both missions. As such, the simplified dynamics model presented in Section 4.2.4 is not considered in the mission power and energy models. A parametric investigation of the wheel on dynamic terrainability performance is presented in Appendix A as well as by the author in [38]. Mobility related power (P_{mob}) for a mission composed of four main driving segments: straight level driving, turning, excavating and climbing a slope, can be estimated by:

$$P_{mob} = P_{level} + P_{turn} + P_{ex} + P_{slope} \quad (4.42)$$

where

$$P_{level} = (R_b + R_c)v_{level} \quad (4.43)$$

$$P_{turn} = M_{st}\Omega_{st} \quad (4.44)$$

$$P_{ex} = (R_b + R_c + R_{ex})v_{ex} \quad (4.45)$$

$$P_{slope} = (R_b + R_c + R_{slope})v_{slope} \quad (4.46)$$

The total mobility energy for the mission can also be computed when the driving distances (L) for each segment is known, as seen below:

$$E_{mob} = P_{level} \frac{L_{level}}{v_{level}} + P_{turn} \frac{L_{turn}}{v_{turn}} + P_{ex} \frac{L_{ex}}{v_{ex}} + P_{slope} \frac{L_{slope}}{v_{slope}} \quad (4.47)$$

The coupling between rover performance metrics z_i and energy and power is evident. The power and energy metrics (f_j) in the system level optimization problems presented later in this chapter are a subset of each driving segment presented here.

Excavation Model

To compute the excavation forces R_{ex} of a rover scooping lunar regolith using the tool shown in Figure 4.4, the McKyes two dimensional excavation model was used [118]. The available drawbar pull (DP) determines the amount of material which can be excavated by the rover at each scoop.

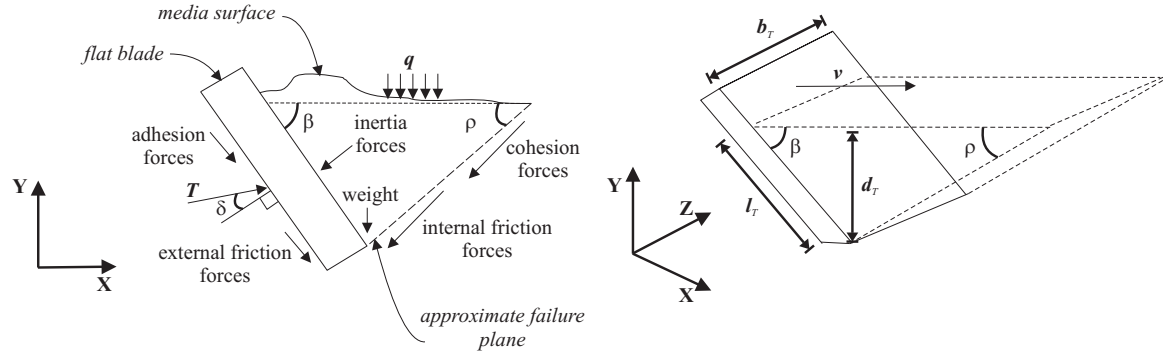


Figure 4.4: 2D McKyes Excavation Model [118]

The total excavation force (T) is given by:

$$\begin{aligned}
T = & \left[\frac{\gamma g d \cot \beta \cot \rho}{2} + gq(\cot \beta + \cot \rho) + c(1 + \cot \rho \cot(\rho + \beta)) \right. \\
& \left. + C_a(1 - \cot \beta \cot(\rho + \beta)) + \frac{\gamma v^2(\tan \rho + \cot(\rho + \phi))}{1 + \tan \rho \cot \beta} \right] \\
& \times \frac{wd}{\cos(\beta + \delta) + \sin(\beta + \delta) + \cot(\rho + \phi)}
\end{aligned} \tag{4.48}$$

For conciseness, the McKyes excavation model parameters are described in Table 4–6. The resulting horizontal and vertical load on the rover are computed respectively as:

$$R_{ex} = T \sin(\beta + \delta) \tag{4.49}$$

$$w_{ex} = T \cos(\beta + \delta) \tag{4.50}$$

To account for the change in rover vertical load during excavation, the excavation scenario is divided up into three drive segments:

- i *Unloaded vehicle mobility*: where the total vehicle weight is considered in the traction equations and no excavation occurs. This drive segment is concerned with driving to the excavation site;
- ii *Loaded vehicle mobility*: where the total vehicle weight and maximum payload weight are considered in the traction equations and no excavation occurs. This drive segment is concerned with transporting regolith to the berm site;
- iii *Excavating mobility (first scoop/last scoop)*: where the vehicle weight for the first scoop, and the vehicle weight and maximum payload weight for the last scoop are considered in the traction equations. The excavation forces that add

to the motion resistances (R_{ex}) and weight (w_{ex}) are considered here. This scenario is used for excavation tasks.

Accounting for the variation in rover mass caused by w_{ex} , the feasibility of excavating the soil is verified by:

$$DP - R_{ex} \geq 0 \quad (4.51)$$

From Equation (4.51) and some basic mission parameters ($\mathbf{c}_{mission}$), mission performance metrics (f_j) such as total driving distance or mission duration can be computed.

4.3 Wheel Optimization for Lunar Missions

System level optimization problems are formulated here for the resource prospecting and berm building scenarios described in Table 4–4. The prospecting mission parameters were adapted from ongoing NASA-CSA joint analog mission RESOLVE, while the excavating scenario was adapted from [99].

In both scenarios, it is of interest to minimize the mobility power and energy consumption for the total mission and individual driving segments. Additionally, given the nature of the excavation mission parameters, it is also desirable to reduce total mission duration and driving distance. The lunar environmental parameters \mathbf{c}_{env} used in this analysis are available in Table 4–5. Finally, the rover parameters (\mathbf{c}_{rover}) are obtained from CSA’s multi-purpose Juno-II rover in [61]. They are listed in Table 4–6.

Table 4–4: Mission Scenario Parameters ($\mathbf{c}_{mission}$)

	Prospecting	Excavating
Objective	Search for water ice in permanently shadowed craters	Build a 2.6m high 180° berm with 25m berm radius around landing site.
Target location	Lunar polar crater	Flat area Lunar polar region
Distance	5km (total)	50m (between excavation site and drop-off site)
	Level: 54%	Level: 100%
	5° slope: 15%	
Terrain type	10° slope: 10%	
	15° slope: 5%	
	20° slope: 1%	
Traverse	15% turning	10% turning
Tasks	Identify drilling sites of interest, drive to sites autonomously, extract and process samples.	Excavate regolith using a scoop and transport to berm area, unload, and repeat.

4.3.1 Prospecting Mission Optimization

Since the details of the prospecting mission architecture are unknown, a set of mission priorities are defined by the author. The following equations describe the objective functions of interest for the prospecting mission scenario.

$$f_1 = P_{total} \quad (4.52)$$

$$f_2 = E_{total} \quad (4.53)$$

$$f_3 = \frac{L_{slope}P_{slope} + L_{level}P_{level} + L_{turn}P_{turn}}{L_{total}} \quad (4.54)$$

$$f_4 = P_{slope} \quad (4.55)$$

Table 4–5: Lunar Environmental Properties (\mathbf{c}_{env})

Parameter	Value
Gravity - g (m/s^2)	1.63
Soil cohesion - C (Pa)	170
Soil internal angle of friction - ϕ ($^\circ$)	37
Soil exponent - n	1.0
Coefficient of passive earth pressure - N_C	1.5
N_γ	25
Soil specific mass - γ (kg/m^3)	1680
k_c (Pa/m^{n-1})	1400
k_ϕ (Pa/m^n)	820000

Table 4–6: Rover Parameters (\mathbf{C}_{rover})

Rover Parameters	Value
Total vehicle mass (kg) - m_{rover}	200
Payload mass (kg) - $m_{payload}$	<i>calculated</i>
Longitudinal wheel spacing (m) - L_{rover}	2
Lateral wheel spacing (m) - b_{rover}	1
Operating speed (m/s) - v	0.6
Excavation speed (m/s) - v_{ex}	0.1
Number of wheels - N	4
Steering mechanism	Skid
Scoop width (m) - b_T	1.5
Digging depth (m) - d_T	0.08
Soil-tool adhesion coefficient (Pa) - C_a	1930
Surcharge mass - q	1
Rake angle - β	45°
External friction angle - δ	10°
Shear plane failure angle - ρ	30°

$$f_5 = P_{level} \quad (4.56)$$

$$f_6 = P_{turn} \quad (4.57)$$

A single objective optimization problem is formulated below for each objective f_j . Constraint g_1 represents the maximum allowable wheel deformation limited by the wheel hub diameter, with D_h set to 0.3m. The upper and lower bounds of the design variable vector \mathbf{x}_{sys} , limited by the Juno-II rover design, are contained in g_2 and g_3 respectively. Finally, a limit was imposed on the available drawbar pull C_{DP} to ensure that the rover can climb slopes of 20° . The dynamic effects of the slow moving prospecting rover are neglected and therefore K_D and C_D are ignored here.

$$\begin{aligned} \text{Find} \quad & \mathbf{x}_{sys} = [D_W, b_W, K_V, K_T, K_L]^T \\ \text{to minimize} \quad & f_j = b_j(\mathbf{x}_{sys}, \mathbf{C}_{rover}, \mathbf{C}_{mission}, \mathbf{C}_{env}) \text{ with } j = 1 \text{ to } 6 \\ \text{subject to} \quad & g_1 = \frac{W_W}{K_V} - (D_W - D_h) \leq 0 \\ & g_2 : \mathbf{x}_{sys} \leq [0.6096, 0.254, 250, 100, 100]^T \\ & g_3 : \mathbf{x}_{sys} \geq [0.25, 0.1, 1, 0.5, 0.5]^T \end{aligned} \quad (4.58)$$

Two algorithms were used to solve the optimization problem presented in Equation (4.58). As the gradients of the objective functions listed in Equations (4.52) to (4.57) can be found and the Hessians estimated, a quasi-Newton sequential quadratic programming algorithm was used with an initial guess. However, to circumvent the possibility of converging to a local optimum, a genetic algorithm, described in more detail in [48], was also used to solve the optimization problems. The solution for

each single objective problem, which were identical for both algorithms used, is contained in Table 4–7. Figure 4.5 plots the normalized objective function values for each optimum wheel design to highlight the conflicting nature of the objectives.

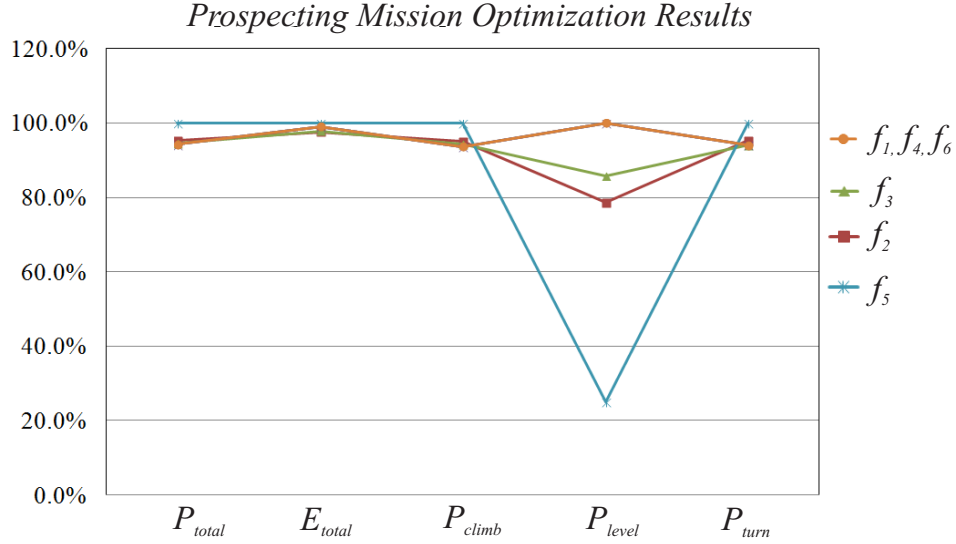


Figure 4.5: Prospecting Mission Objective Function Results Comparison

It is interesting to note that for all six objective functions, the maximum values for wheel diameter (D_W), width (b_W), torsional stiffness (K_T) and lateral stiffness (K_L) were found. The value of vertical stiffness, on the other hand, has different effects on the mission objectives. A stiffer wheel ($K_V=4.93\text{kN/m}$) results in the lowest total mobility power (min f_1), average slope climbing power (min f_4) and turning power (min f_6). To minimize the power consumed during straight level line driving (min f_5), however, a softer wheel ($K_V=2.09\text{kN/m}$) is preferred. A reduction in wheel stiffness by 58% results in a reduction in level driving power of nearly 80%. However, an

Table 4-7: Prospecting Mission Optimization Results

f_j	D_W (m)	b_W (m)	K_V (kN/m)	K_T (kNm/rad)	K_L (kN/m)	P_{total} (W)	E_{total} (kJ)	P_{climb} (W)	P_{level} (W)	P_{turn} (W)
f_1	0.61	0.254	4.93	100	100	247.4	135.7	59.1	2.8	8.0
f_2	-	-	3.35	-	-	250.1	133.7	60.0	2.2	8.1
f_3	-	-	3.87	-	-	248	134.0	59.5	2.4	8.0
f_4	-	-	4.93	-	-	247.4	135.7	59.1	2.8	8.0
f_5	-	-	2.09	-	-	262.5	137	63.1	1.7	8.5
f_6	-	-	4.93	-	-	247.4	135.7	59.1	2.8	8.0

increase in climbing and turning power ensues by 7% and 6% respectively. Minimizing overall mission energy consumption ($\min f_2$), which reduces the power system requirements of the rover, and minimizing the weighted power consumption ($\min f_3$) yields similar stiffness of 3.35kN/m and 3.89 kN/m respectively. Both these stiffness' appear to be a good trade-off as the level driving power is reduced by 15% and 21% for $\min f_3$ and $\min f_2$ respectively, with an almost negligible increase in climbing and steering power. With more detailed information on the mission scenario, each of the objectives may be of equal importance. As such, a multi-objective optimization problem can be formulated, as presented in [72], to illustrate the conflict between the mission performance objectives.

4.3.2 Excavation Mission Optimization

The excavation mission scenario outlined in Table 4–4 requires the rover to excavate and transport regolith to build a berm. In this case, total mission duration (t_{total}) and distance traversed (L_{total}) should be minimized as well as power and energy during various driving sequences. The following equations describe the objective functions of interest for the excavation mission scenario.

$$f_7 = L_{total} \tag{4.59}$$

$$f_8 = t_{total} \tag{4.60}$$

$$f_9 = P_{total} \tag{4.61}$$

$$f_{10} = E_{total} \tag{4.62}$$

$$f_{11} = \frac{L_{empty}P_{empty} + L_{full}P_{full} + L_{ex}P_{ex}}{L_{trip}} \quad (4.63)$$

$$f_{12} = P_{empty} \quad (4.64)$$

$$f_{13} = P_{full} \quad (4.65)$$

$$f_{14} = P_{ex} \quad (4.66)$$

Distance in kilometers (L_{total}) and time in (earth) days (t_{total}) are computed as the first two objectives in Equations (4.59) and (4.60). Then, total mobility power (P_{total}) and total energy (E_{total}) for the mission are also minimized in Equations (4.61) and (4.62). Given that the mission scenario is defined heuristically, it is of interest to weigh the importance of each drive segment power consumption. This is achieved in Equation (4.63) by averaging the mobility power according to the drive segment distance over entire mission drive distance. The effect of wheel parameters on empty (P_{empty}), full (P_{full}) and excavation (P_{ex}) power are also addressed in the objectives listed in Equations (4.64) to (4.66) respectively. An optimization problem is formulated below and is solved for each objective described in Equations (4.59) to (4.66).

$$\begin{aligned} \text{Find} \quad & \mathbf{x}_{sys} = [D_W, D_h, b_W, K_V, K_T, K_L]^T \\ \text{to minimize} \quad & f_j = b_j(\mathbf{x}_{sys}, \mathbf{C}_{rover}, \mathbf{C}_{mission}, \mathbf{C}_{env}) \text{ with } j = 7 \text{ to } 14 \\ \text{subject to} \quad & g_5 = \frac{W_W}{K_V} - (D_W - D_h) \leq 0 \\ & g_6 : \mathbf{x}_{sys} \leq [0.6096, 0.254, 250, 100, 100]^T \\ & g_7 : \mathbf{x}_{sys} \geq [0.25, 0.1, 1, 0.5, 0.5]^T \end{aligned} \quad (4.67)$$

Similarly to the prospecting mission, a genetic algorithm is used to verify the results of a modified SQP approach to solve the berm building scenario optimization problems [48]. The solutions to each optimization problem are outlined in Table 4–8, while Figure 4.6 plots the objective space of each optimum wheel design.

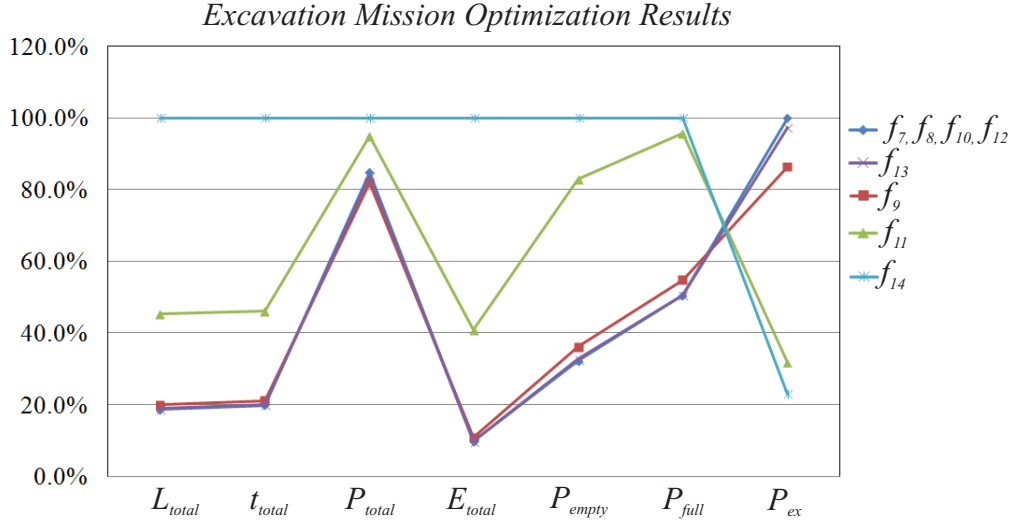


Figure 4.6: Excavation Mission Objective Function Results Comparison

Minimizing the total distance travelled (min f_7) yields the same solution as minimizing time (min f_8), total energy (min f_{10}) and power for empty driving (min f_{12}). This is because wheel parameters were optimized to excavate and transport the maximum amount of regolith per trip, thereby reducing the total energy, power and driving demands of the entire mission. Similarly to the prospecting mission, the maximum wheel size (D_W , b_W), torsional stiffness (K_T) and lateral stiffness (K_L) is preferred for these objective functions. Vertical stiffness is low, allowing for high

Table 4–8: Excavation Mission Optimization Results

f_j	D_W (m)	b_W (m)	K_V (kN/m)	K_T (kNm/rad)	K_L (kN/m)	L_{total} (km)	Time (days)	P_{total} (W)	E_{total} (kJ)	P_{empty} (W)	P_{full} (W)	P_{ex} (W)
f_7	0.61	0.254	2.09	100	100	289.1	6	53.8	7089.5	8.5	15.23	30.1
f_8	-	-	-	-	-	-	-	-	-	-	-	-
f_9	0.61	0.15	2.09	100	100	308.9	6.4	52	7855.3	9.5	16.5	26.0
f_{10}	-	-	-	-	-	-	-	-	-	-	-	-
f_{11}	0.4	0.1	6.51	100	100	701.6	14	60.2	29842	21.8	28.8	9.6
f_{12}	-	-	-	-	-	-	-	-	-	-	-	-
f_{13}	0.61	0.254	2.20	100	100	291.8	6.1	53.1	7099.3	8.6	15.22	29.3
f_{14}	0.37	0.1	8.1	100	100	1544.4	30.3	63.4	72840	26.3	30.1	6.9

traction to be developed. The total distance travelled is 289.1km resulting in a mission lasting 6 earth days.

Interestingly, minimizing total mobility power ($\min f_9$) results in a 13.4% decrease in excavation power, yet in a slight increase in empty and full driving power. This is achieved by reducing the wheel width to 15.4cm. The total mobility power is reduced by 4% and travel distance is increased by 19.8km compared to the minimum distance case (f_7).

Minimizing total mobility power as a function of drive segment distances ($\min f_{11}$) yields significant findings. A smaller, stiffer wheel ($D_W=0.4$, $b_W=0.1$, $K_V=6.51\text{kN/m}$) is found, which reduces the excavation power by close to 70% over the distance minimization case. However, solution minimizes the excavation power by reducing the available drawbar pull, thereby reducing the excavation distance driven per trip. As the empty and full driving distances remain constant per trip, only the excavation distance is affected (as well as the total number of trips). Therefore, an increase by close to 50% for $\min f_{11}$ is seen in the empty and full drive power over the minimum distance case ($\min f_7, f_8, f_{10}, f_{12}$). The mission distance and duration is over double, at 701.6km and 14 days respectively.

Minimizing the full drive power (f_{13}) results in a 5% increase in vertical stiffness over the minimum distance case. This is because a stiffer wheel provides less deflection on heavier loads, resulting in improved driving efficiency. The total distance increase is only 2.7km and approximately 2.5hrs of drive time. The resulting effect on power, however, is minimal. Full driving power is reduced by less than 1% while empty and excavating power increase by 1.2% and 2.7% respectively.

Minimizing excavation mobility power ($\min f_{14}$), much like weighted mobility power ($\min f_{11}$), favours a decrease in excavation power at the expense of empty and full driving power. The optimal wheel is even smaller and stiffer than for the weighted drive segment power minimization case, at $D_W=0.37$, $b_W=0.1$ and $K_V=8.1\text{kN/m}$. This results in a total mission duration of over 30 days to cover a distance of 1544.4km. The excavation mobility power is reduced by close to 80% over the minimum distance case, which comes at the cost of a 70% and 50% increase in empty and full driving power.

For this mission scenario, the minimum drive distance case ($\min f_7$) appears to yield the best trade-off between mission duration, distance, and mobility energy and power requirements. However, a change in mission priorities, such as more severe mobility power or energy constraints, will result in a change in the preferred trade-off solution.

4.4 System Level Analysis Discussion

The system level analysis assumes that wheel system design variables are independent of one another. The purpose of this assumption was to determine what the optimal wheel variables are, independent of wheel concept configurations. However, to achieve the performance described in this chapter, a wheel concept must be designed and fabricated to the prescribed size and stiffness requirements. Inevitably, vertical, torsional and lateral stiffnesses of the wheel are dependent on the structural configuration of the wheel. Furthermore, the mechanical reliability of the wheel will also become an important performance metric. The variable coupling, as well as reliability performance, are addressed at the component level analysis.

Nonetheless, the preceding analysis, as well as the parametric analysis presented in Appendix A, demonstrates the importance of elastic wheel design on rover and mission performance. Broadly, the following recommendations for developing wheel concepts and subsequently optimizing them for specific rover and mission scenarios can be made:

- i Wheel system design variables directly affect mission performance and should be determined as a function of the mission priorities and rover designs.
- ii Maximizing the diameter and width of the wheel is always desirable to improve rover performance, unless a decrease in mobility power is desired.
- iii Torsional and lateral stiffness should always be maximized to reduce energy losses while driving and turning, particularly for inefficient skid-steer maneuvers;
- iv Wheel vertical stiffness has the most conflicting effect on performance. Although low stiffness improves traction, rider comfort and road holding, it also serves to increase the power required to drive. A trade-off value is recommended which considers mission priorities. Excavating scenarios or higher speed operations favour wheels with more compliance, whereas long range missions where energy consumption is critical, favour stiffer wheels.

It should be noted that two important wheel parameters were considered out of scope in the context of this work: tread patterns and the number of wheels of a vehicle. Details on the effect of tread pattern are available in [17]. The number of wheels impacts rover design and should be considered in future work.

CHAPTER 5

Development, Testing and Modelling of Wheel Design Concepts

This chapter describes wheel concepts explored in the context of this research, both by prototyping and numerical modelling. A functional breakdown of a wheel is presented first, followed by a presentation of physical and numerical investigations of wheel concepts. Finally, a discussion on wheel concept selection criteria is presented.

5.1 Wheel Development

Chapter 2 presented a number of existing rover wheel concepts. Most wheels rely on linear-elastic deformation of the internal structure of the wheel, although some employ hyper-elastic deformation like the TWEEL [93] or plastic deformation like iRings [90]. A functional breakdown of the main components of a wheel is illustrated in Figure 5.1.

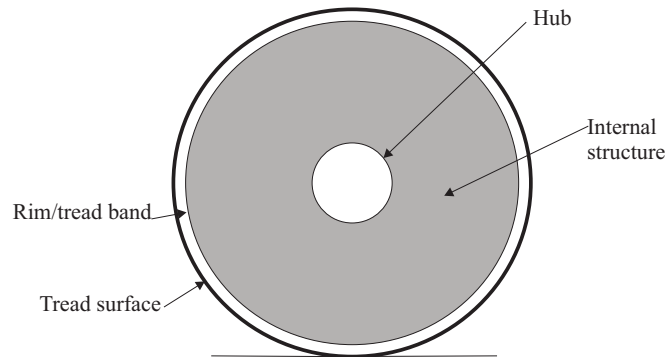


Figure 5.1: Wheel Configuration Functional Breakdown

The system level analysis presented in Chapter 4 established the importance of wheel compliance in achieving mission performance requirements. As such, it is of interest to investigate wheel concepts which employ novel materials, deformation mechanism and internal structural configurations. The following subsections describe a set of wheels which were developed in the context of, or concurrently with, this research.

5.1.1 Segmented Wheel Concept

The segmented wheel concept is a variation of the metallic flexible carcass and relies on linear elastic deformation for compliance. Instead of a continuous outer tread linking the deformation of the radial bands, each segment behaves like radially mounted spring legs.

Two distinct prototypes developed concurrently by the author and a team of undergraduate students and all-terrain vehicle manufacturer Ontario Drive and Gear (ODG) can be described as segmented wheels. The ODG wheel was illustrated in Figure 2.4(f). The McGill concept uses segments which bear the load of the vehicle, transmit torque and provide compliance. The shape of the individual segments was designed to minimize stress concentration yet provide adequate deformation. The segments themselves were fabricated from one piece of 0.018 inch stainless steel and formed to the desired shape. They were mounted to a commercial hub for remote control all-terrain vehicles. The manufacturing method and final prototype is shown in Figure 5.2.

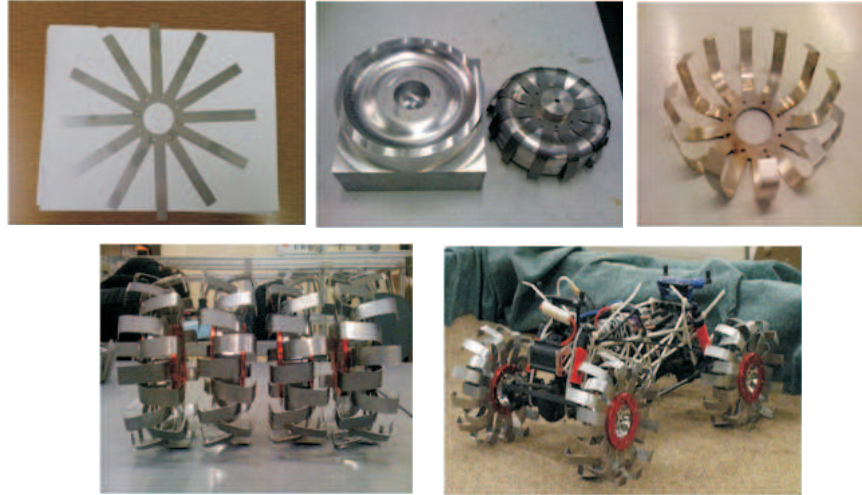


Figure 5.2: McGill Segmented Wheel Concept

5.1.2 Cellular Wheel Concept

Cellular materials offer a promising solution to designing flexible wheels as their microstructure can be tailored to achieve desirable mechanical properties. Hexagonal and circular cells are advantageous as they expand upon compression. Similarly to the hoop springs wheel illustrated in Figure 2.5, each individual unit cell provides elastic compliance to the overall wheel structure, while a continuous outer tread band distributes the load throughout the cells. Figures 5.3 and 5.4 illustrate examples of cellular wheels prototyped. Wheels were fabricated from aluminum hexagonal cells with 0.375 inch and 0.5 inch unit cells, and polypropylene circular 0.275 inch cells. The polypropylene allowed the cells to recover from cell wall buckling, given the hyperelasticity of the base material.

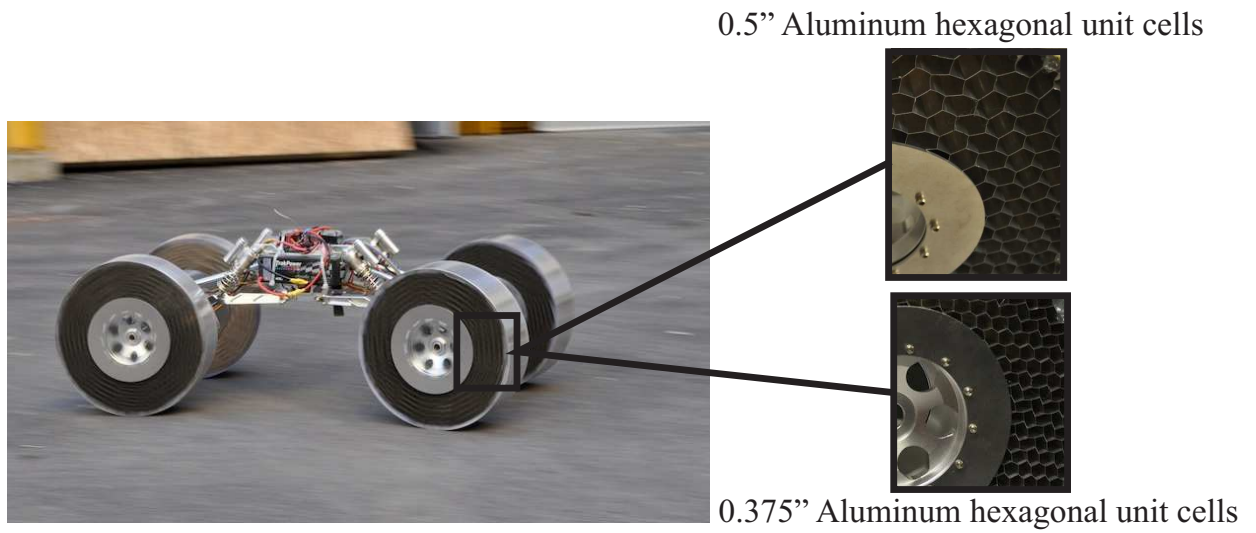


Figure 5.3: Cellular Wheel with aluminum Hexagonal Unit Cells

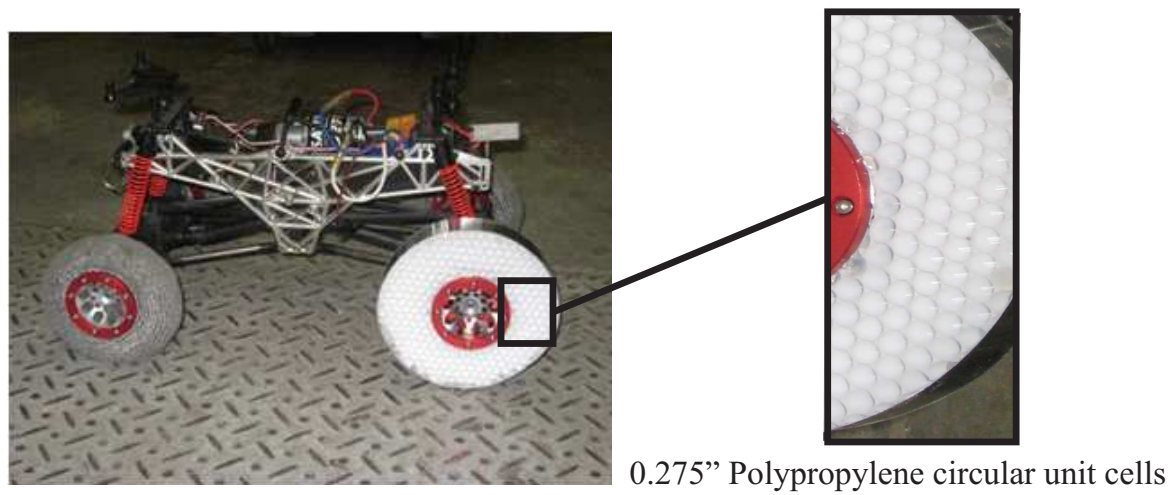


Figure 5.4: Cellular Wheel with Polypropylene Circular Unit Cells

5.1.3 iRings Wheel Concept

The iRings wheel presents a new class of wheels which rely on plastic, rather than elastic, deformation to provide compliance. The iRings wheel is composed of three main components: the hub, the outer tread and inner fill material. The outer tread is made of chain mail fabric, while the inner filler material is polypropylene balls. The iRings wheel mimics an under-inflated tire, where a filler material replaces the pressurized air. The filler material supports the vehicle load and provides a deformable volume to conform to surface irregularities. This deformation allows for a large contact area to be created between the wheel and ground. Additionally, the deformation mechanisms results in a overly damped wheel with no visible bounce if the wheel is dropped from a height.

The performance of the wheel can be modified by changing the fill material, the volume of the fill material, and the tire thickness to wheel diameter ratio. The iRings wheel, originally proposed in [90], has been designed to various scales and vehicles as shown in Figure 5.5.

5.1.4 Baseline Rubber Pneumatic Tire

Rubber pneumatic tires are presented here as they provide a comparison for physical testing. ODG's custom amphibious 24 inch (61cm) diameter wheels, seen in Figure 5.6, were used to compare the performance of compliant wheels on CSA's Juno II rover.



Figure 5.5: McGill's iRings on CSA's Juno II rover



Figure 5.6: ODG Rubber Wheels

To compare small scale wheel prototypes, the standard rubber wheels provided with a remote controlled (RC) vehicle were used. Both 5 inch (12.7cm) and 8 inch (20.3cm) diameter wheels are shown in Figure 5.7. These wheels rely solely on rubber carcass deformation to achieve compliance as they are not filled with pressurized air.



Figure 5.7: Small scale rubber non-pneumatic tires

5.2 Experimental Performance Investigation

The goal of this section is to compare the performance and identify limitations of the wheel concepts outlined above. The following subsections describe the results from three test campaigns undertaken to assess wheel prototype performance. First, a qualitative assessment of general mobility metrics was conducted on the RC vehicles. Then, quantitative testing was performed to assess the iRings wheel concept on rover trafficability, maneuverability and terrainability.

5.2.1 Qualitative Performance Comparison

The RC vehicles used for the 5 inch and 8 inch wheel diameter wheel prototypes are depicted in Figure 5.7. The platforms are commercially available, and are controlled by a user using a radio-frequency hand-held controller. Because of the low accuracy control method, the performance assessments using the RC cars were

qualitative in nature.

Four performance metrics were assessed for the small scale wheels: trafficability, maneuverability, terrainability and reliability. Trafficability testing consisted of driving on sandy surfaces while pulling a load and climbing slopes. Maneuverability testing investigated turning behaviour of the RC car using the wheel prototypes. Terrainability was addressed by quasi-static testing of obstacle climbing and driving over irregular terrain. Reliability was assessed by inspection for any permanent deformation in the wheel after testing. The qualitative comparison of wheel prototype performance is shown in Table 5–1. Some testing images are available in Figure 5.8. A relative scale of 1 to 5 was used, where 1 indicates poor performance and 5 indicates excellent performance. In Table 5–1, Cell-1, -2 and -3 represent the 0.375 inch 3003 aluminum hexagonal unit cell, 0.5 inch aluminum hexagonal unit cell and 0.275 inch polypropylene circular unit cell wheels respectively.

Table 5–1: Qualitative Wheel Performance Evaluation

Performance Metric	Cell-1	Cell-2	Cell-3	Segmented	iRings	Rubber
Trafficability	3	3	4	3	5	5
Maneuverability	5	5	5	4	2	5
Terrainability (static)	3	4	4	5	5	5
Reliability	3	2	5	3	4	5
Rank	5	5	2	4	3	1

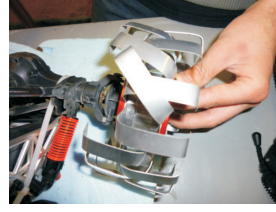
The baseline rubber wheel concept consistently performs well in all four metrics. However, as described in Chapter 2, rubber compounds are impractical on the lunar surface. The iRings and polypropylene cellular wheel (Cell-3) have similar overall performance. Given the low stiffness and high damping, the iRings wheel develops

excellent traction and conforms well to irregular surfaces and obstacles. This, however, results in considerable lateral deformation in the wheel during steering thereby reducing maneuverability. No failures were seen during testing as the wheel does not rely on elastic deformation of the wheel structural components. Both aluminum cellular wheels (Cell-1 and Cell-2), however suffered permanent plastic deformation during testing. The larger hexagonal cells (Cell-2) achieves a lower stiffness and therefore improved irregular terrain performance over the smaller hexagonal cells (Cell-1). The stiffer Cell-1 demonstrates less overall plastic deformation but exhibits considerable vibration during irregular terrain traversal. Cell-2 circumvents plastic deformation given the hyperelastic behaviour of polypropylene. The lateral stiffness of the cellular wheel concepts lead to a responsive and highly maneuverable rover. The segmented wheel also offers a good trade-off between the performance metrics. The discontinuous outer tread emulates grousers, yielding excellent traction in irregular terrain, soft soil and obstacle negotiation. The segments deformed permanently, however, during the testing where high loads were applied. The plastic deformation which occurred during testing for the segmented and Cell-2 wheels are seen in Figure 5.8(b) and (d).

The wheel cellular and segmented wheel concepts are investigated numerically in more detail in Sections 5.3.2 and 5.3.1 respectively. The behaviour of the iRings wheel, however, is difficult to model numerically, as such, this concept underwent extensive testing as described in Sections 5.2.2 and 5.2.3. Although not presented in this work, it should be noted that reliability of iRings was assessed by successfully driving over 200km.



(a) Slope climbing



(b) Segment plastic deformation



(c) Driving



(d) Cellular material plastic deformation

Figure 5.8: Wheel Testing

5.2.2 Trafficability and Maneuverability Testing

A quantitative measurement of the trafficability and maneuverability performance is presented here. CSA's Juno II rover [61] was used with two traction systems: the iRings wheels and the ODG rubber pneumatic tire.

First, the rover is commanded forward to pull an eight-wheeled Argo vehicle, provided by ODG, and a load cell is used to measure the tension in the cable linking the two vehicles. The test set-up is shown in Figure 5.9. Sinkage is not measured during this test campaign. The slip is estimated by averaging the forward velocity of the rover at 2m intervals and measuring the motor rotational velocity using motor encoders. The tests are repeated to compare the drawbar pull coefficient of the rubber and iRings wheels. The pressure of the rubber wheels was regulated at the nominal operating condition of 5 psi. The experimental drawbar pull coefficient plotted in Figure 5.10, as defined in Equation (4.17) of Chapter 4.



Figure 5.9: Drawbar pull Test Set-up

Typical rover operating scenarios should see slippage between 0-20% [10], therefore, the C_{DP} of the various traction systems in this range are compared. At 20% slip, where drawbar pull is typically at its maximum, both traction systems operate at a $C_{DP} \approx 0.55$, which is equivalent to climbing a 28° slope. At 100% slip, the experimentally computed C_{DP} increases to values of 0.7 for iRings and 0.8 for rubber wheels. This increase is caused by an increase in sinkage, and therefore increase in ground contact area, when the traction system digs into the ground.

The rolling resistance coefficient (C_r) of each traction system is also estimated, by dragging the rover using the Argo and measuring the load cell output. This results in a range of rolling resistances shown in Table 5–2.

To assess the wheel design effect on the tractive efficiency, the rover is driven over a 10m distance using various payload mass, at various speeds and over various terrain slopes. The results are shown in Table 5–3, where the power required to drive the rover is compared to a baseline value of the power required to drive the rover using rubber wheels on level terrain in low and high gear. The results yield a qualitative

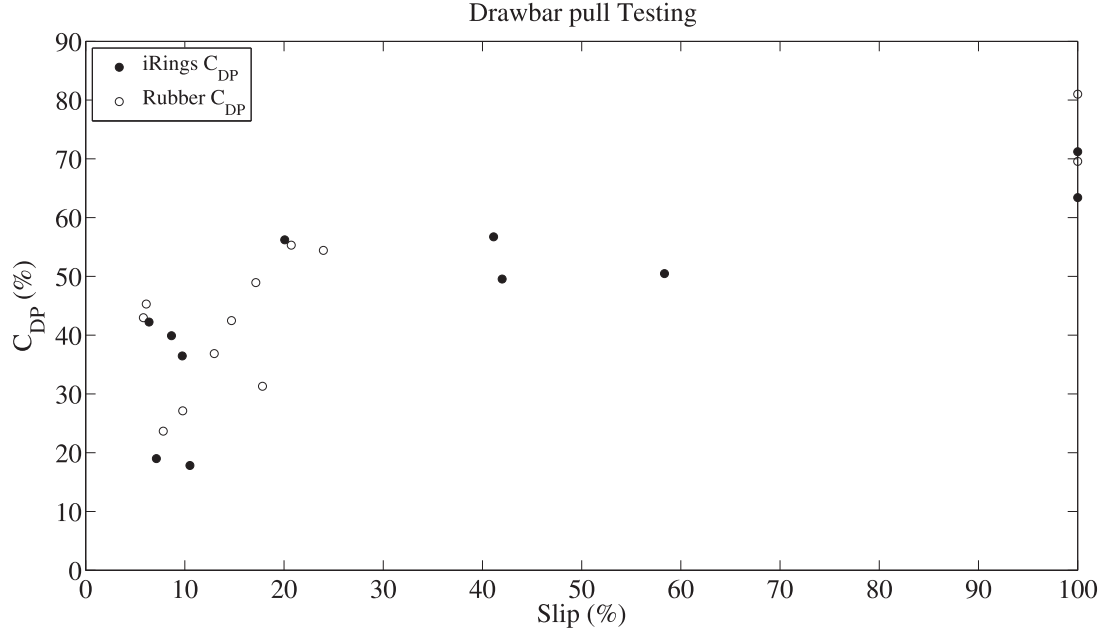


Figure 5.10: Drawbar pull Testing

Table 5–2: Traction system C_r

Wheel Type	$C_{r(lower)}$	$C_{r(upper)}$
Rubber wheels	0.03	0.08
iRings wheels	0.2	0.26

comparison of the driving and turning efficiency. The level terrain testing was conducted on a sandy terrain, while slope testing was conducted on a clayey loam with some vegetation. Further, the slopes in a natural environment are not consistent, and therefore vary in angle throughout the length of the test.

Table 5–3: Driving efficiency η_{DP}

Case	Rubber	iRings
0°, w/payload, low gear	-	x3
0°, w/ payload, high gear	-	x3.3
15-20°, w/ payload, low gear	x2.5	x6.25
18-29°, w/ payload, low gear	x3.75	x6.25

The maneuverability performance is assessed for each traction system type during the trafficability tests. At the end of each driving sequence, the rover is commanded to complete a skid-steer maneuver turning the rover in place 180°. The estimated relative steering efficiency for each driving scenario is shown in Table 5–4.

Table 5–4: Turning efficiency η_{st}

Case	Rubber	iRings
0°, w/payload, low gear	x5	x10
0°, w/ payload, high gear	x5	N/A
15-20°, w/ payload, low gear	x6.25	x10
18-29°, w/ payload, low gear	x6.25	x10

The values shown in Tables 5–3 and 5–4 are approximate, as the power draw throughout the testing is dynamic due to the user input commands and motor controller design. Nevertheless, the results demonstrate the inefficiencies of the iRings concept

over the rubber wheels. Given the large deformations in the wheel, tractive and steering efficiency is approximately doubled for the iRings. Additionally, skid-steering is shown to be approximately 5 times less efficient than straight line driving for rubber wheels on level ground. In high gear, the rover has insufficient torque to skid steer with the maximum payload mass in sand using the iRings. Figure 5.11 illustrates the excessive lateral loads on the rubber wheels while conducting a turning maneuver on a slope, with a payload mass.



Figure 5.11: Lateral Deformation on Under-inflated Rubber Tires

5.2.3 Dynamic Terrainability Testing

As described in Chapter 4 and Appendix A, low stiffness and high dampening contribute to improved rider comfort and road holding ability. A dynamic terrainability test campaign is presented here to investigate the benefits of the iRings deformation mechanism. The iRings and benchmark rubber wheels suspension properties were characterized by means of a standard drop test [119] for which the properties are shown in Table 5–5. Although the iRings wheels achieve compliance primarily through plastic deformation, some elasticity is observable during the drop test.

Table 5–5: Wheel Dynamic Properties

Wheel type	Stiffness (kN/m)	Damping coefficient (Ns/m)	Mass (kg)
iRings	5.71	194.5	3.62
Rubber	1.54	15.8	0.91

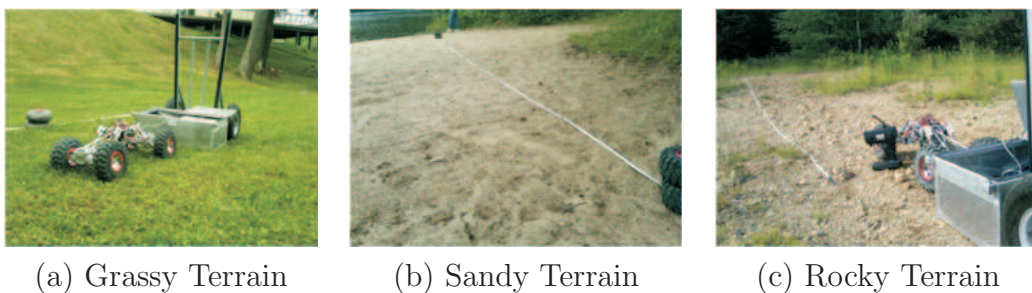
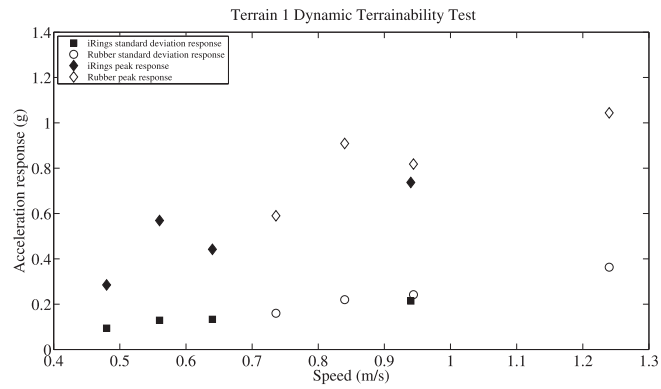


Figure 5.12: Terrain Types

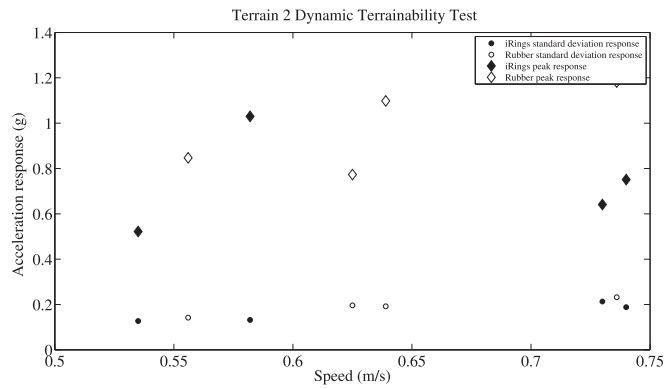
The iRings wheels are stiffer, in terms of elastic deformation, than the benchmark rubber wheels, yet have a higher damping coefficient by an order of magnitude. The wheels were tested repeatedly over three terrain types: grass (terrain 1), soft sand (terrain 2), and hard sand/gravel (terrain 3) depicted in Figure 5.12.

An accelerometer was mounted vertically on the axle between the two rear wheels in order to measure the vertical acceleration of the unsprung mass. This allowed the evaluation of the rider comfort metric for the various wheels in different terrain and speed conditions. The road holding ability was not measured here given the complexity required for measurement of the nominal ground force during driving.

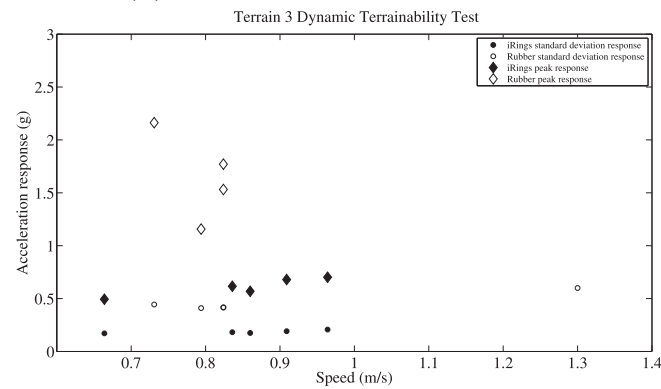
The vehicle was driven over a 10m distance four times on each terrain using both sets of wheels. A summary of the results for Terrain 1 is shown in Figure 5.13(a). It should be noted that the speed was controlled by the user input to a joystick, so the speed average speed is shown here. An increase in speed causes an increase in vertical



(a) Terrain 1-Grass Testing



(b) Terrain 2-Soft Sand Testing



(c) Terrain 3-Hard sand/gravel Testing

Figure 5.13: Dynamic Terrainability Results

acceleration. The performance variation between the wheel types at the same speeds is not clear in Figure 5.13(b), as speed was difficult to control accurately. The iRings wheels still demonstrate a lower value of standard deviation of vertical acceleration, which is the rider comfort metric. This is evident in Figure 5.13(a) where at 0.94m/s, the rider comfort value is improved by 12% for iRings wheels. Peak acceleration seen by the rover chassis is also measured and results in improvements up to 30%.

Terrain 2 is comparatively a much softer terrain than terrain 1. The terrain slows the rover, resulting in speeds lower than in terrain 1. Figure 5.13(b) illustrates the rider comfort metric over rover speed.

In this test, the average speed was more consistent between tests, allowing a better comparison between the two wheels. The response of the iRings over terrain 2 shows an improvement of 7% at 0.75m/s. The lower difference in vertical acceleration between the two wheels is due to two main factors:

1. At a reduced speed, the acceleration will be lower;
2. On a soft soil like terrain 2, a significant amount of damping is provided by terrain deformation thus reducing the impact load on the wheel.

Unfortunately, only terrain elevation as a function of frequency is considered in the power spectral density for irregular terrains as described in Equation (4.35). Thus, for a full characterization on the dynamic performance of wheel suspension properties, a more detailed consideration of soil properties is necessary.

Terrain 3 results presented in Figure 5.13(c) demonstrate a clear improvement in rider comfort with iRings wheels, as the terrain is a comparatively more rigid and rougher than terrains 1 and 2. In terrain 3, the iRings wheels improve rider comfort

by up to 57%. Shock loads were shown to have been reduced by up to 70% over the rubber wheels. Thus, it appears that an increase in wheel damping has more benefit than a reduction of wheel stiffness in rough terrain, which confirms the predictions in Appendix A.

5.3 Preliminary Numerical Investigation

Preliminary wheel prototyping requires a selection of size, shape and material of wheel structural components. These structural components determine the load bearing capacity and flexibility of the wheel. For example, the thickness of the segments in the segmented wheel concept of Figure 5.2 will determine the deformation, and therefore contact area and tractive properties of the wheel. As such, two distinct wheel concepts cannot be compared equally unless they are optimized to perform similarly, even though they may be of similar mass or size. Therefore, the ability to tailor a given wheel concept to perform as required is an important factor in the selection of a wheel concept. To optimize the performance of the wheel concept, as it will be shown in Chapter 6, a wheel must be parameterized into a set of discrete design variables. Additionally, the ability to simulate the behaviour of a wheel is important if numerical modelling tools are used to quantify the performance of the design. This section discusses the numerical investigation of two wheel concepts: the segmented wheel and cellular wheel.

5.3.1 Segmented Wheel Structural Optimization

The segmented wheel shown in Figure 5.2 was adapted to accommodate the heavier loading conditions of a larger scale wheel. The evolved segmented wheel concept is illustrated in Figure 5.14.

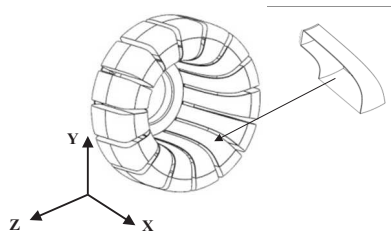


Figure 5.14: Segmented Wheel Concept

Taking advantage of wheel symmetry, the analysis is simplified to a structural analysis of the segment. Three Lamé curves are selected to parameterize the wheel segment, as illustrated in Figure 5.15. The Lamé curves are defined by three independent parameters, η , b_x and b_y , as shown in Equation (5.1).

$$\left| \frac{x}{b_x} \right|^\eta + \left| \frac{y}{b_y} \right|^\eta = 1 \quad (5.1)$$

where b_x and b_y are the x - and y -axis dimensions of the curve. With an exponent of $\eta = 2$ and $(b_x/b_y) = 1$, Equation (5.1) represents the equation of a circle with radius b_x . An advantage of using Lamé curves is that when $\eta > 2$, the curvature vanishes at the intersection of the axis [32]. This signifies that G^2 continuity is ensured along the curve and at the intersection between the curves, thereby reducing stress concentrations. Alternative curve parameterization techniques can be employed here, however the Lamé curves provide a convenient method for ensuring G^2 continuity. A cross-sectional view of the parameterized segment with various values of η is shown

in Figure 5.15, where S_1 corresponds to the outer segment curve, S_2 is the inner segment curve, and S_3 is the bottom surface.

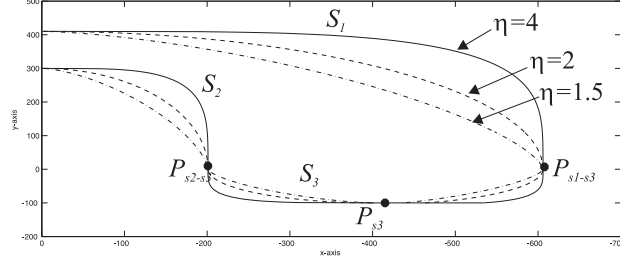


Figure 5.15: Parameterization of Wheel Segment into Lamé curves

Once the wheel segment is parameterized into the set of size and shape design variables, a finite element model of the segment can be created. The FE model is created using Altair Hyperworks' pre-processing software Hypermesh before being solved in Altair's RADIOSS solver. The material properties for AISI 1025 carbon steel and 3750 shell elements were used to mesh the wheel segment. Three loading conditions were considered: a vertical load F_N , a lateral load F_{st} and a horizontal load F_r . F_{st} represents the steering resistance seen at the ground interface acting along the x -axis; and F_r is the forward motion resistance along the z -axis; F_N is the normal force from the rover weight along the y -axis. The loading conditions result in torsion about the x -axis, and a bending moment about the y -axis and z -axis at the hub interface of the segment. These bending moments translate to the vertical deflection in the y -axis and twist about the x -axis of the wheel assembly. To investigate the segmented wheel concept, a structural optimization can now be conducted with a FE model defined by a set of shape and geometric design variables.

Structural Optimization

Discontinuities and high curvatures in mechanical shapes cause stress concentrations and reduce fatigue life under dynamic loading conditions. Second order geometric continuity G^2 is desired at the blending point between curves to avoid localized stresses [107]. As a compliant wheel will undergo large deformation, areas of stress concentration should be minimized to improve reliability performance. Compliant mechanisms are prone to fatigue failure caused by repetitive loading and large deformations. In this research, the wheel segment behaves as the compliant element of the wheel and undergoes large deformations. To improve the reliability and life of the wheel, the curvature and stress concentrations are minimized using the single objective shape optimization problem described below.

$$\begin{aligned}
&\text{Minimize } y_s(\mathbf{x}_{comp}) = \frac{1}{n} \sum_1^n w_k \kappa_k^2 \\
&\text{where } \kappa(x, y) = \frac{(\eta - 1)(xy)^{\eta-2}(x^\eta + y^\eta)}{(x^{2\eta-2} + y^{2\eta-2})^{3/2}} \\
&\text{and } w_k = \frac{\bar{\sigma}_k}{\bar{\sigma}_T}
\end{aligned} \tag{5.2}$$

Equation (5.2) was first presented in Desrochers, Pasini and Angeles for a shape synthesis problem using Lamé curves in [32]. In Equations (5.2), the objective function $y_s(\mathbf{x}_{comp})$ represents the sum of squares of the weighted curvature of n supporting points along the segment. w_k and κ_k represent the normalized weighting factor and curvature at the k^{th} supporting point respectively. The weighted curvature is minimized for the design variable vector \mathbf{x}_{comp} , defined in Equation (5.4) and shown in Figure 5.15. The values for $b_{x,i}$ and $b_{y,i}$, where the subscript i identifies the curve, are constrained by the wheel width, diameter and hub diameter. To ensure second

order geometric (G^2) continuity, η must be greater than 2. This allows the blending points between curves 1, 2, and 3 to have a smooth change in curvature without causing stress concentrations. In the case of the single objective optimization problem defined below, the thickness of the segment (t) is fixed to a nominal value of 5mm. The normalized weight factor of supporting point k is computed using the rms value of the von Mises stress at the k^{th} supporting point ($\bar{\sigma}_k$) normalized by the rms von Mises stress along the Lamé curve ($\bar{\sigma}_T$). The normalized weighting factor satisfies the relationship shown below.

$$\sum_{k=1}^n w_k = 1 \quad (5.3)$$

If a purely geometrically optimum segment shape is desired, the weighting factors can be determined simply by normalizing the curvature with a known number of supporting points n . The resulting geometrically optimum ($y_{g,1}$) will minimize the segment curvature with no consideration on stress distribution. Minimizing the curvature in a compliant mechanism has a direct effect on its fatigue life; however to estimate life, the resulting stress in the segment cannot be ignored. Therefore, the FE model must be solved at each objective function evaluation. Using the relationship described in Equation (5.2) to compute the stress related weight factors, solving the SOO will result in a so-called structurally optimum segment shape ($y_{s,1}$). This signifies that the resulting design variable vector \mathbf{x}_{comp} will be found by minimizing k^{th} supporting point curvature as a function of stress distribution in the segment. As discussed in Chapter 4, it is also of interest to maximize torsional and lateral stiffness while minimizing vertical stiffness. The stresses in the component must also

remain below the yield value to ensure deflection remains in the elastic range of the material. The multi-objective optimization problem is formulated below. This formulation allows for the system level design variables to be coupled through the FE model and address wheel reliability performance.

$$\begin{aligned}
&\text{Find} && \mathbf{x}_{comp} = [\eta_i, b_{xi}, b_{yi}, t]^T \text{ where } i = 1, 2, 3 \\
&\text{to minimize} && \mathbf{y}_{seg} = \left[\frac{N}{\sum_{p=1}^N \delta_{Y,p}}, \frac{\sum_{p=1}^N \delta_{X,p}}{N}, \frac{\sum_{p=1}^N \delta_{Z,p}}{N} \right]^T \\
&\text{subject to} && \sigma_v < \sigma_Y \\
&&& \eta_i > 2 \\
&&& 2.5mm \leq t \leq 10mm \\
&&& 2b_{x3} = b_{x1} - b_{x2} = W_w = 400mm \\
&&& b_{y1} = b_{y3} - b_{x2} = \frac{D_W - D_h}{2} = 300mm \\
&&& b_{y1} - b_{y3} = 10mm
\end{aligned} \tag{5.4}$$

The design variable vector \mathbf{x}_{comp} , shown in Equation (5.4), contains the shape variables describing the three Lamé curves as well as the thickness (t) of the segments. The three objective functions are selected to be the rms value of the deflection in the x -, y -, and z -directions at N points along the bottom surface of the wheel segment. The objective function vector \mathbf{y} is described in Equation (5.4). The constraints, shown in Equation (5.4), limit the material to linear-elastic deformation, while relating the segment design variables to the wheel dimensions D_w , D_h and W_w . These constraints are imposed by the rover design. The wheel segment material, in this problem, is carbon steel with a Young's Modulus of 210 GPa and yield strength of

250 MPa. The von Mises failure criterion is used to determine the allowable stress in the segment. The thickness of the segment is constrained between 2.5mm and 10mm. The remaining constraints relate the segment geometry to the wheel geometry to achieve a wheel width and diameter of 400mm and 800mm respectively.

To solve the SOO problem, a genetic algorithm (GA) in Matlab is run in a co-simulation with the finite element solver Altair RADIOSS. The GA is selected as it avoids computing the gradient of the objective function, which can be cumbersome for structural analysis requiring a FE model. Additionally, a population based search that maintains diversity in the solutions avoids converging to a local optimum. The parameters of the GA were tuned heuristically to enable faster convergence and are available in Table 5–6, while details on the algorithm itself are available in [24]. For the structurally optimum shape, a FEA is conducted at each iteration to solve the stress distribution along the segment and determine the weight factors w_k . For the geometrically optimum case, stress distribution in the segment is ignored and the FEA is not required in the optimization loop. The SOO described in Equation (5.2) is solved twice to find the geometrically and structurally optimum segment shape.

To solve the MOO problem, the multi-objective genetic algorithm (MOGA) implemented in Matlab is used to solve for a set of non-dominated solutions. A brief description of the MOGA algorithm is available here, while further details can be found in [41]. First, a set of 25 designs are randomly generated using the Matlab code. The designs are then modelled, pre-processed and solved by the finite element code. The results of the FEA are interpreted by the Matlab code to evaluate the objective functions and constraints. A fitness value to each design is assigned based

on the rank of the respective solutions. In multi-objective problems, non-dominance is considered in the ranking, and therefore several solutions can be of the same rank. To avoid an increase in the density of the solutions in the same area of the Pareto front, a niching count is implemented based on the distance between neighbouring solutions. This ensures that a wider spread of possible solutions is found. The remaining fit solutions are then crossed-over and mutated to generate the offspring to fill the population size. The optimization loop is then complete, and the solutions can then be evaluated using the FE solver once again. This process continues until a pre-determined number of generations have been evaluated. The optimization loop was allowed to run for 12hours on a 2.40 GHz Core 2 Duo CPU. Table 5–6 outlines both the single and multi-objective genetic algorithm parameters which were tuned heuristically to converge to optimal solutions efficiently. The population sizes were selected to ensure population diversity during the optimization process, and the mutation and crossover parameters were tuned to reduce the total number of generations needed to find optimal solutions.

Table 5–6: Genetic algorithm properties

Property	GA values	MOGA values
Population Size	20	25
Crossover fraction	0.8	0.8
Elite Count	2	2
Tournament size	4	4
Migration fraction	0.2	0.2
Pareto fraction	-	0.35
Maximum Generations	50	30

The results from the two single objective optimization (SOO) problems are shown in Table 5–7. Note that the component thickness was fixed at 5mm. To compare the SOO results, the objective space of the geometrically and structurally optimum solutions are illustrated in Figure 5.16(a) and (b) along with the MOO results.

Table 5–7: Solution for geometrically and structurally optimum segments

\mathbf{x}_{comp}	Geometric optimum $y_{g,1}$	Structural optimum $y_{s,1}$
η_1	2.11	2.28
b_{x1}	800mm	580mm
b_{y1}	242mm	250mm
η_2	2.16	2.07
b_{x2}	605mm	385mm
b_{y2}	199mm	222mm
η_1	5.05	4.5
b_{y3}	58mm	50mm

The MOO objective space for each solution is shown in Figure 5.16(a) and (b). The objective function values are normalized with respect to the maximum displacements. It should be noted that the geometrically optimum solution $y_{g,1}$ yields a result above 100% . This is explained by the nature of the objective function for the geometric SOO ($y_{g,1}$), where structural analysis is ignored. The consequence is that the maximum von Mises stress is above the material yield strength, resulting in an infeasible design.

After 30 generations, the MOGA was able to find a Pareto front. The conflict between the deflection in the y -direction and x -and z -directions are apparent in the distribution of the design variable space, where there is a clear set of non-dominated

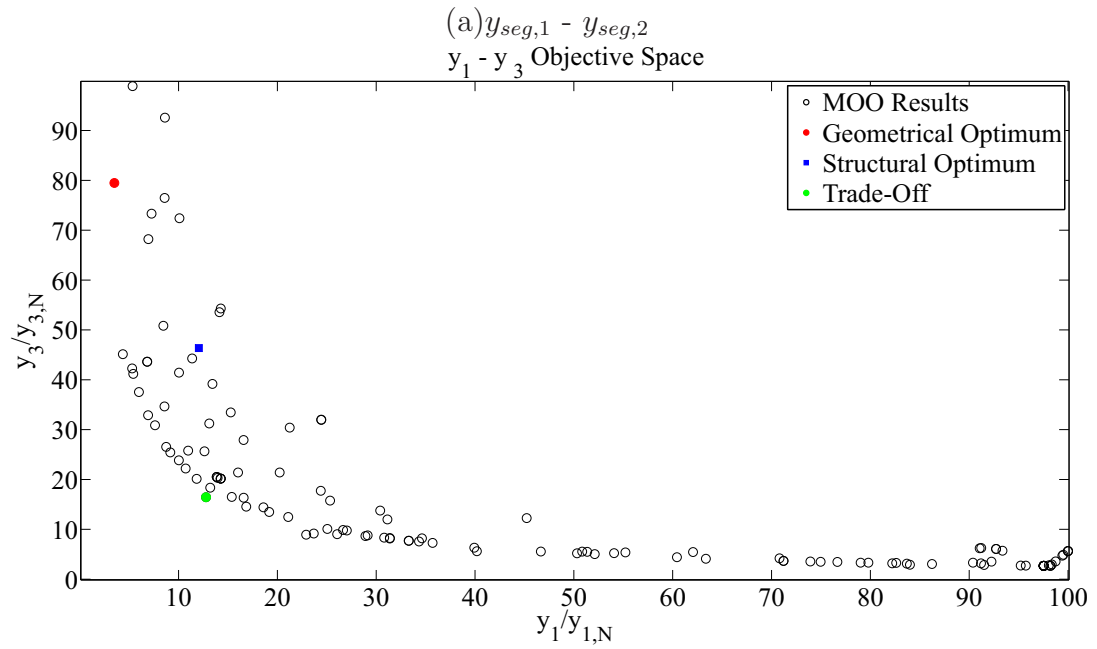
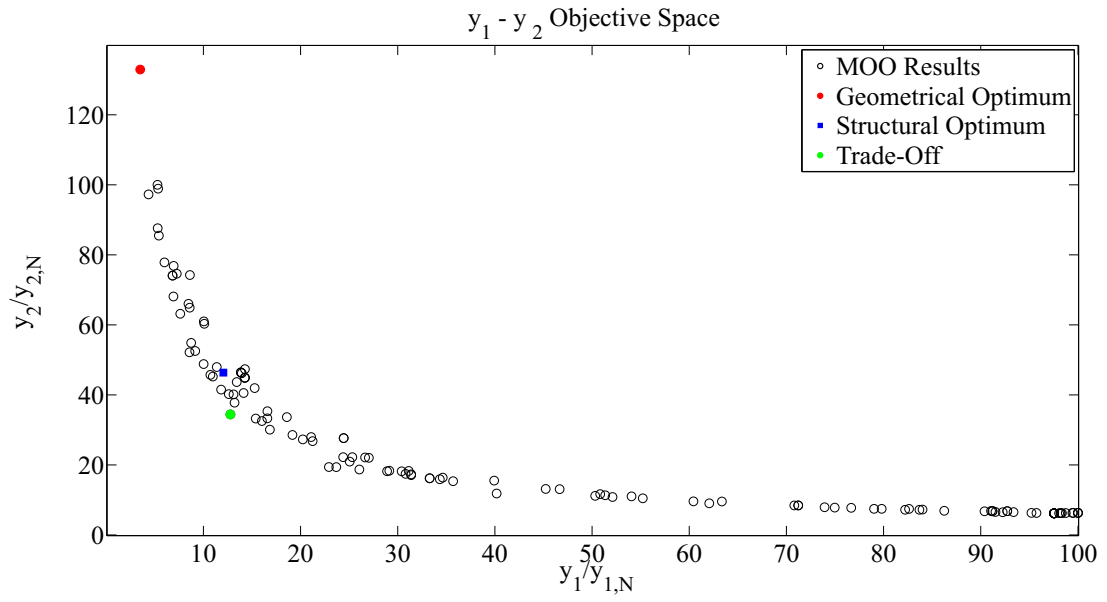
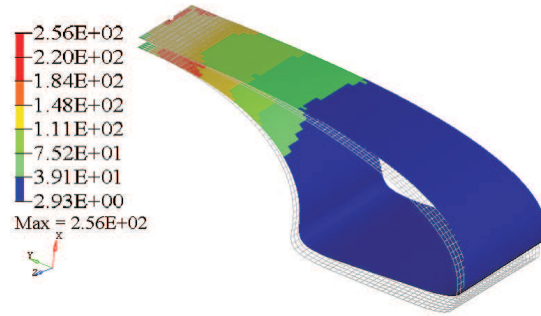


Figure 5.16: Objective Space

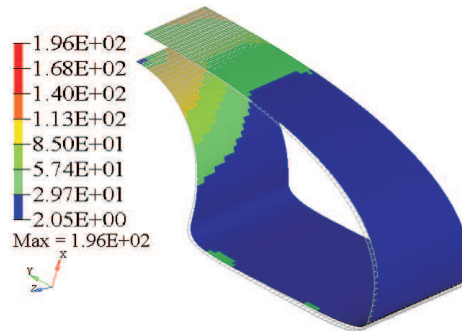
solutions. From the Pareto set, a trade-off design was selected to compare with the structurally and geometrically optimum segments. This trade-off is selected to have an equal importance of each objective function. A comparison between the von Mises stress distribution (in MPa) of the FEA results of the geometrically, structurally and trade-off solutions are shown in Figure 5.17(a), (b) and (c) respectively. A discernible difference in the shape of the wheel segments is observed. The undeformed wheel segment is shown as a mesh to illustrate the resulting compliance.

The trade-off solution of Figure 5.17(c) improves stiffness in the z -axis by 12% in comparison to the structurally optimum design, while producing a minimal reduction in compliance in the y -axis of 4%. Further, no noticeable reduction in stiffness is seen in the x -axis. The maximum von Mises stress in the trade-off wheel segment is 40% lower than the structurally optimum, even though stress minimization was not an explicit objective in the MOO. As neither solution dominates the other, both solutions are considered optimal. Therefore, the structurally SOO found one solution in the subset of Pareto optimal solutions of the MOO problem. The geometrically optimum design, on the other hand, will plastically deform under the prescribed loading conditions.

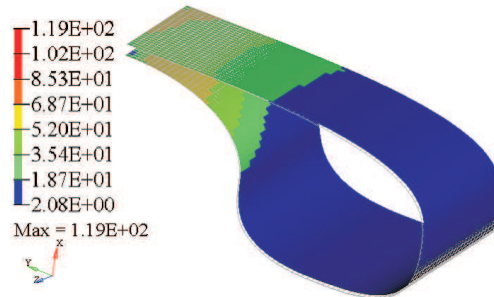
The segmented wheel numerical analysis demonstrates that a variation in wheel design variables directly affects wheel compliance. The results are dependent on the nature of the problem formulation, and careful consideration of the objectives and constraints is necessary. The nature of the wheel concept itself limits the feasible design space, whereas the values of wheel design variable determine the performance of the wheel. Therefore, a concept should be selected based on the deformation



(a) Geometrically Optimum



(b) Structurally Optimum



c) Pareto Optimal Trade-off

Figure 5.17: Optimal Segments

mechanism and design parameterizability such that the optimal shape and size of the structural components can be determined through numerical analysis.

5.3.2 Cellular Wheel Parametric Analysis

Lattice materials offer significant advantages for wheel designs. Unit cell topology, size and base material can be tailored to achieve desirable mechanical properties. Homogenization techniques can also be used to obtain average mechanical properties of a cellular material, thereby significantly simplifying FE models. As such, a wheel can be modelled as a homogeneous material.

The cellular wheel prototypes shown in Figures 5.3 and 5.4 were fabricated based on unit cell size, shape and material availability. Additional unit cell types, for which constitutive material models for the linear range exist, are illustrated in Figure 5.18.

As discussed in Chapter 2, closed-form expressions for the homogeneous cellular material properties in the linear range of behaviour are further developed then for the non-linear range. Therefore, modelling non-linear materials, such as polypropylene used in Cell-3, is not considered here. The homogeneous material properties of some 2D unit cells for relative cell densities (ρ) below 0.3 in the linear range are available in Table 5–8. The properties include the Young’s modulus (\bar{E}), shear modulus (\bar{G}) and Poisson’s ratio ($\bar{\nu}$) in the xy -plane defined in Figure 5.18. The relative density in this case refers to the ratio between the density of the cellular material and the solid material from which the cells are made. The open faced cubic, face centered cubic (FCC), body centered cubic (BCC) and open faced cuboctahedron closed-form

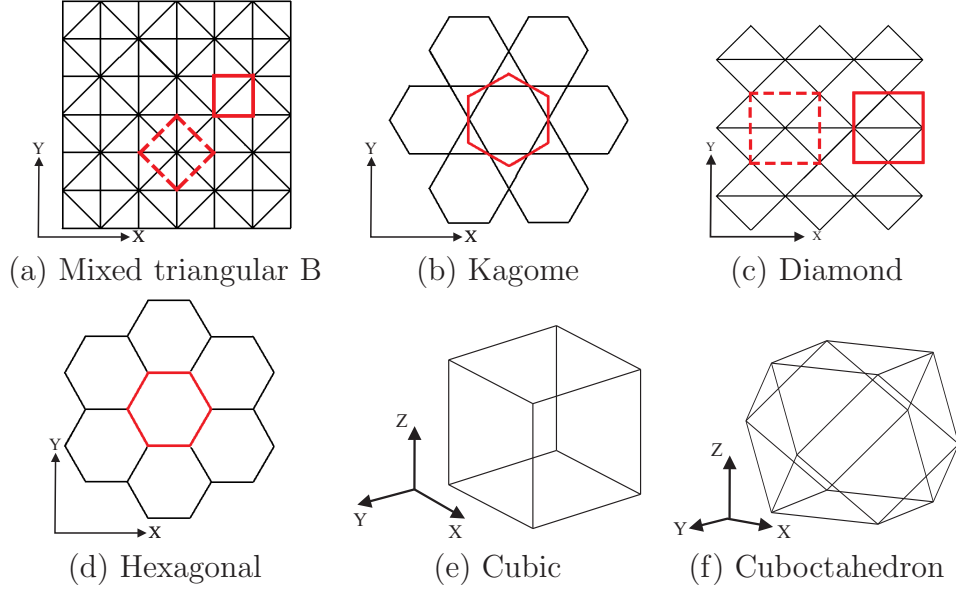


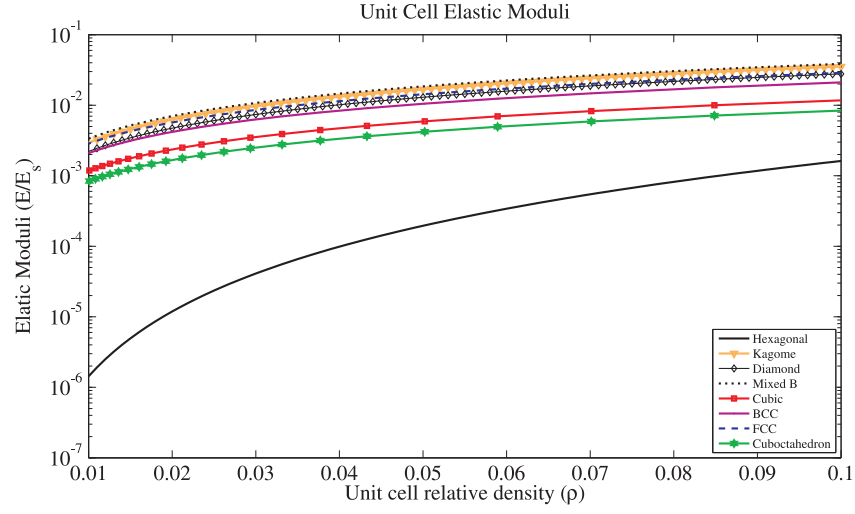
Figure 5.18: Unit Cell Topology Designs

expressions of material constitutive models are available in Appendix B, for the coordinate reference frames illustrated in Figure 5.18.

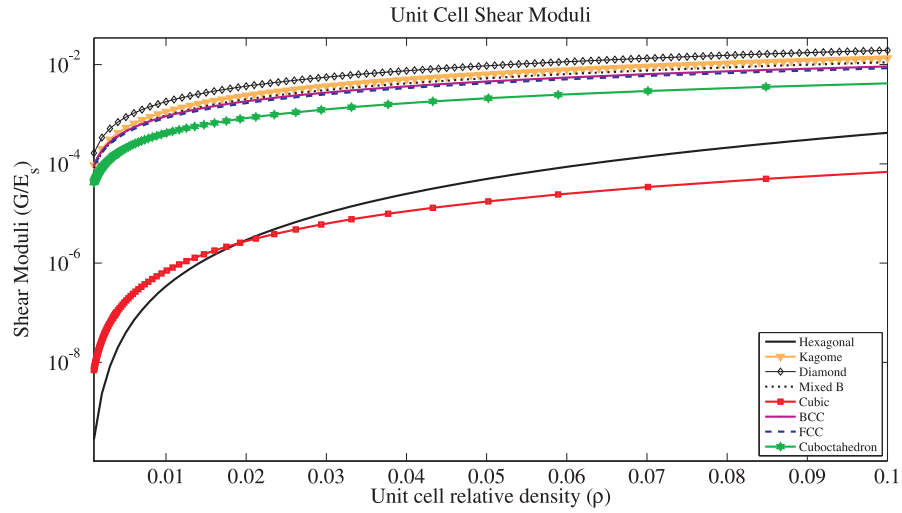
Figure 5.19(a) and (b) illustrate the material density effect on the mechanical properties for unit cells illustrated in Figure 5.18. Typical applications of cellular materials warrant high stiffness and low mass. Most of the unit cells available in literature offer such properties. For flexible wheel designs, however, compliance in the unit cell is desirable. The elastic and shear moduli of hexagonal cells are shown to be several order of magnitude below those of the alternative cells. The 3D cuboctahedron and cubic cells, however, offer lower elastic moduli than the Kagome, Diamond, Mixed B, body centered cubic (BCC) and face centered cubic (FCC). Both hexagonal and cubic unit cells offer the lowest shear moduli, while the cuboctahedron yields lower shear than the remaining unit cells.

Table 5–8: Unit cell 2D homogenized properties found in [65]

Unit cell type	Elastic moduli (\bar{E})	Shear moduli (\bar{G})	Poisson's ratio ($\bar{\nu}$)
Regular hexagons	$\bar{E}/E_s = 0.58\rho^{1.046}$	$\bar{G}/E_s = 0.52\rho^{3.091}$	$\bar{\nu}/\nu_s = -6.7\rho^2 - 0.54\rho + 3$
Kagome	$\bar{E}/E_s = 0.42\rho^{1.076}$	$\bar{G}/E_s = 0.16\rho^{1.076}$	$\bar{\nu}/\nu_s = 1$
Diamond	$\bar{E}_{xx}/E_s = 0.35\rho^{1.1}$ $\bar{E}_{yy}/E_b = 0.16\rho^{1.134}$	$\bar{G}/E_s = 0.21\rho^{1.035}$	$\bar{\nu}_{xy}/\nu_s = -0.11\rho + 1.24$ $\bar{\nu}_{yx}/\nu_b = -\rho + 3$
Mixed B	$\bar{E}/E_s = 0.443\rho^{1.06}$	$\bar{G}/E_s = 0.13\rho^{1.068}$	$\bar{\nu}/\nu_s = 0.28\rho + 0.78$



(a) Elastic Moduli



(b) Shear Moduli

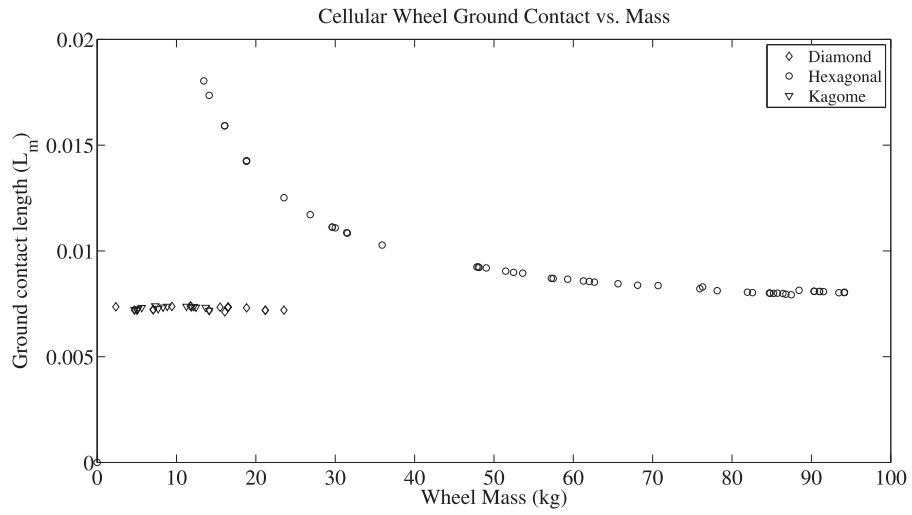
Figure 5.19: Unit cell macroscopic properties

To investigate the applicability of the design of unit cell topologies in a wheel concept, a parametric analysis of a 2D homogeneous wheel rolling on a rigid surface is conducted. The homogeneous material properties are defined by the Kagomé, Diamond and Hexagonal material models outlined in Table 5–8. First, a nominal load is applied to the wheel hub followed by an applied forward velocity at the hub resulting in a rolling motion of the wheel. The relative density is varied to verify the resulting contact area created between the wheel and rigid ground. The results are illustrated in Figure 5.20, where wheel mass and contact area are compared. The simulation model parameters, derived from the small scale wheel prototyping activities outlined in Section 5.2.1, are listed in Table 5–9.

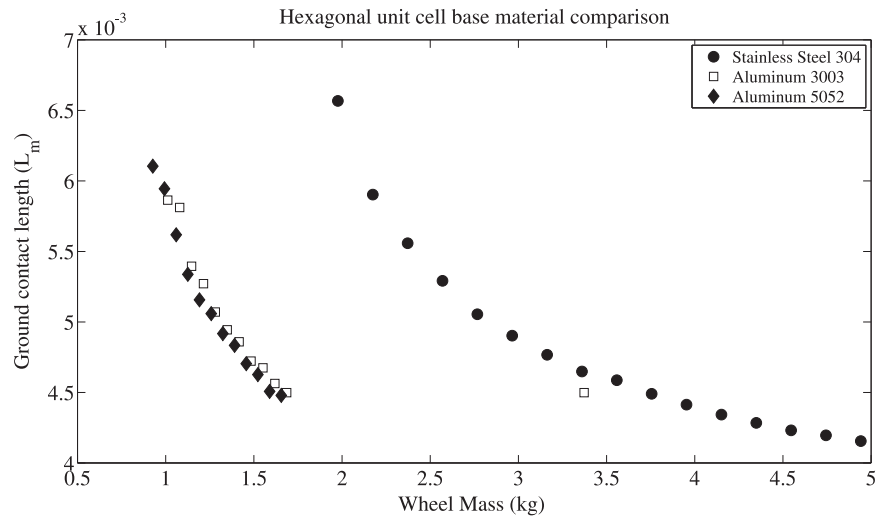
Table 5–9: Homogeneous Cellular Wheel Parametric Analysis

Parameter	Value
Wheel diameter in mm (D_W)	203.2 (8 inches)
Wheel hub diameter in mm (D_h)	33.3
Hub applied mass in kg (m_r)	5
Gravity in m/s^2 (g)	9.81
Applied forward velocity in m/s (v)	1
Soil type	Rigid ground
Wheel-ground friction coefficient (μ)	0.3

Figure 5.20(a) illustrates that the hexagonal wheel is the most sensitive to relative density (ρ). Reducing ρ reduces the mass of the wheel and increases the deformation, resulting in a larger contact with the ground. Both Kagomé and Diamond unit cells require low ρ to achieve the hexagonal wheel contact length. The ground contact area achieved by a hexagonal wheel weighing 90kg is produced by a Kagomé or Diamond wheel weighing 10kg.



(a) Cellular wheel unit cell comparison



(d) Cellular wheel base material comparison

Figure 5.20: Cellular Wheel Numerical Investigations

The base material of the unit cell also effects performance. Figure 5.20(b) illustrates the results of the hexagonal cellular wheels with three materials: Stainless Steel-304, Aluminum 3003 and Aluminum-5052.

From Figure 5.20(a) and (b), it is clear that cellular materials can offer a wide range of elastic wheel behaviour. In particular, hexagonal unit cells offer a good trade-off between mass and compliance. Reducing ρ will result in thin walls of the unit cell. To ensure the feasibility of the wheel design, however, the cell wall von Mises and axial stress must be verified. From the macroscopic constitutive material models, the macroscopic stresses and strains in the homogeneous material can be related to the microscopic stresses and strains in the unit cell walls. Although computing the resulting cell wall deformation in a representative volume element of the cellular material can be time consuming, the homogenization technique still offers a reduced computational effort compared to direct FE modelling of the cellular wheel microstructure.

5.4 Selection of Wheel Concepts

This chapter described the wheel concept development and analysis. The results presented do not identify a single wheel concept which is clearly superior to the others. Instead, this investigation has given insight into the selection criteria of wheels suitable for performance optimization. The selection criteria are listed here:

- i Parameterizability: the wheel concept must be described by a set of variables which dictate the resulting wheel structure. In this work, these variables are dubbed the component level design variables.

- ii Scalability: the wheel concepts should be scalable to accommodate a variety of mission and rover concepts, without significant modifications to the baseline concept.
- iii Computational feasibility: to optimize a set of design variables describing the wheel concept, numerical models simulating wheel behaviour are solved iteratively. As such, the computational effort required to solve the numerical models is of interest.
- iv Wide objective function space: the behaviour of the wheel should vary directly as a function of the component level design variables to achieve discernible improvements in performance. This is especially useful when the same wheel concept is optimized for various mission or rover applications.

The iRings wheel, while offering a novel wheel deformation mechanism and promising performance, is difficult to model numerically. As such, optimizing iRings performance at a mission and rover level requires extensive experimental investigations to develop empirically based surrogate models relating design variables to performance objectives. It should be noted that significant improvements to the iRings concept has been achieved through experimental testing beyond the scope of this thesis.

The segmented wheel was shown to be both parameterizable and computationally feasible. Additionally, experimental investigations presented in Section 5.2.1 and in yet to be published work by ODG demonstrated good mobility performance. Through the MOO presented in Section 5.3.1, the relationship between component level design variables and wheel behaviour was shown. However, the scalability of the concept required significant modifications to the concept. As such, the component

level design variables considered for various scales would be different. Nonetheless, optimization of segmented wheel concept is still possible.

Cellular wheel concepts can achieve a wide range of mobility performance by tailoring the cellular microstructure. The component level design variables are a function of unit cell topology, and hence directly scalable to any wheel size. Employing homogenization techniques also enables simplification of the numerical models, reducing overall simulation time. In the context of this research, cellular wheels offer a suitable concept for developing a systematic approach for wheel optimization. As such, the cellular wheel is selected to develop the component level analysis in the following chapter. The generalized optimization approach presented in Figure 3.1 is applicable to alternative wheel concept, provided that the wheel is parameterizable into a set of component level design variables and can be modelled numerically.

CHAPTER 6

Component Level Optimization

This chapter presents the component level analysis, applied to a cellular wheel concept. The homogeneous wheel multi-objective optimization and cellular material optimization problems are solved and verification and discussion of the results are provided.

6.1 Homogeneous Wheel Multi-Objective Optimization

In the first step, the wheel internal structure is modelled as a homogeneous material. Employing a homogeneous material over direct modelling of a cellular microstructure greatly reduces computational efforts, which is of interest when simulations must be solved iteratively within the optimization problem. To further reduce computational efforts in solving the MOO, the ground is assumed to be rigid. This assumption affects the quantitative analysis of the system level objectives, and is addressed in more detail in Section 6.3.3. To evaluate the wheel trafficability, maneuverability and terrainability performance, two separate drive scenarios are modelled in a time-domain FEA. The first scenario simulates a skid-steering maneuver of a lunar wheel, where a vertical load is applied to the wheel hub, as well as a rotational and lateral velocity. The second scenario consists of driving the wheel forward and surmounting a step obstacle, where a vertical load is applied to the wheel hub along

with a rotational and forward velocity. The loading conditions and modelling parameters of both FE models are summarized in Table 6–1 while Figure 6.1(a) and (b) depict the drive scenarios in Altair Hyperworks’s HyperView FE pre-processor. The RADIOSS Block explicit FE solver is used in both cases to compute the resulting wheel behaviour.

Table 6–1: Wheel Simulation Parameters

Simulation	W_w (N)	ω_w (rad/s)	v_w (m/s)	μ
Maneuverability	490.5	0.29	0.3 (y -axis)	0.3
Trafficability/Terrainability	490.5	0.29	0.1 (x -axis)	0.3

Rigid 1D bar elements are used to link the wheel hub attachment point with the inner structure of the cellular wheel. As described above, the cellular structure is idealized using 3D BRICK elements with a linear-elastic orthotropic material model. Finally, the outer surface of the wheel is modelled by a thin steel outer shell, composed of 1548 2D SHELL elements. Two contact interfaces are defined: one between the wheel shell and rigid ground using the shell nodes as slave nodes to the rigid ground master surface; and a second between the outer surface of the wheel 3D elements and the nodes of the outer wheel shell. For the wheel-ground interface, a Coulomb friction model was used to simplify the rolling resistance coefficient, introduced in Equation (4.18).

The loading conditions outlined in Table 6–1 were selected based on the resource prospecting mission and rover design of Chapter 4. The size and shape of the wheel was defined based on the system level analysis results, i.e. maximum wheel diameter

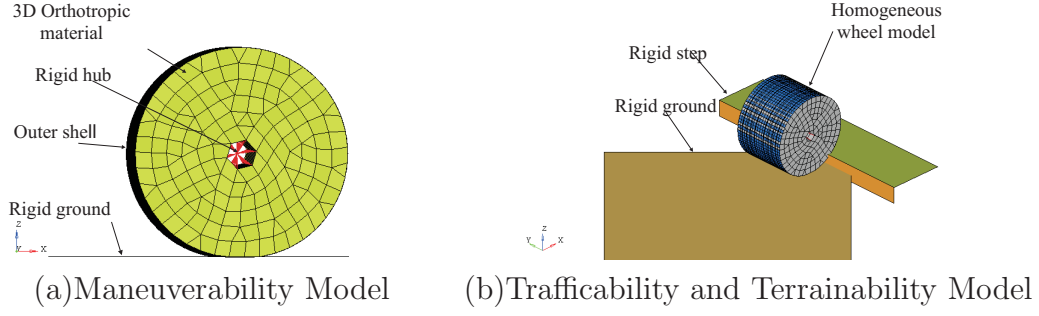


Figure 6.1: FE Simulation Models

and width. The vertical, lateral and torsional wheel stiffness found at the system-level become targets for the component level optimization problem.

6.1.1 Wheel MOO Problem Formulation

Ideally, rover performance metrics z_i , introduced in Chapter 4, are directly at the component level analysis. This is impractical due to the rigid ground assumption used for computational efficiency. Therefore, the system and component level analyses are linked through a set of shared system design variables ($\mathbf{x}_{sys,S}^*$) and component-level objectives (y_k). In this case, $\mathbf{x}_{sys,S}^*$ constrains the wheel geometry through D_w , D_h and b_w . The objective functions of the component level MOO, y_k , are defined as wheel-ground contact area (A_{wheel}), lateral deflection (δ_{lat}) and torsional deflection (θ_{tors}). The component level objectives y_k are directly related to the local system design variables ($\mathbf{x}_{sys,l}^*$) vertical (K_V), lateral (K_L) and torsional stiffness (K_T). To verify the effectiveness of this approach, an additional error analysis step is conducted using coupling equations q_k . Thus, system level objectives (z_i and f_j) are implicitly considered at the component level through objectives y_k . Although the stress and strain in the wheel elements are computed in the wheel MOO problem, mechanical reliability is only considered at the microscopic scale when solving

for feasible unit cell designs. The wheel MOO problem is formulated as:

$$\begin{aligned}
& \text{Find} && \mathbf{x}_{comp} = [\bar{\rho}, \bar{E}_{xx}, \bar{E}_{yy}, \bar{E}_{zz}, \bar{G}_{xy}, \bar{G}_{yz}, \bar{G}_{zx}, \bar{\nu}_{xy}, \bar{\nu}_{yz}, \bar{\nu}_{zx}]^T \\
& \text{to minimize} && \mathbf{y}(\mathbf{x}_{comp}) = [\delta_{lat,MAX}, \frac{1}{A_{wheel,RMS}}, \theta_{tors,MAX}]^T \\
& \text{subject to} && \forall \mathbf{x}_{comp} \exists \bar{\mathbf{K}}^{-1} \\
& && 0 \leq \bar{\rho} \leq 0.91 \\
& && \bar{E}_{ij} \leq 10^7 Pa \\
& && \bar{G}_{ij} \leq 10^7 Pa \\
& && -0.5 \leq \bar{\nu}_{ij} \leq 0.5
\end{aligned} \tag{6.1}$$

where design variable vector \mathbf{x}_{comp} consists of the homogeneous wheel orthotropic material properties, $\delta_{lat,MAX}$ represents the maximum lateral deformation, $A_{wheel,RMS}$ is the root mean square value for ground contact area and $\theta_{tors,MAX}$ is the maximum torsional deformation. The resulting compliance matrix $\bar{\mathbf{C}}$ of a homogeneous 3D or 2D orthotropic material can be found respectively with [2]:

$$\bar{\mathbf{C}}_{3D} = \bar{\mathbf{K}}_{3D}^{-1} = \begin{bmatrix} 1/E_{xx} & -\nu_{yx}/E_{yy} & -\nu_{zx}/E_{zz} & 0 & 0 & 0 \\ -\nu_{xy}/E_{xx} & 1/E_{yy} & -\nu_{zy}/E_{zz} & 0 & 0 & 0 \\ -\nu_{xz}/E_{xx} & -\nu_{yz}/E_{yy} & 1/E_{zz} & 0 & 0 & 0 \\ 0 & 0 & 0 & 1/G_{xy} & 0 & 0 \\ 0 & 0 & 0 & 0 & 1/G_{yz} & 0 \\ 0 & 0 & 0 & 0 & 0 & 1/G_{zx} \end{bmatrix} \tag{6.2}$$

$$\bar{\mathbf{C}}_{2D} = \bar{\mathbf{K}}_{2D}^{-1} = \begin{bmatrix} 1/E_{xx} & -\nu_{zx}/E_{zz} & 0 \\ -\nu_{xz}/E_{xx} & 1/E_{zz} & 0 \\ 0 & 0 & 1/G_{zx} \end{bmatrix} \quad (6.3)$$

The design variable vector \mathbf{x}_{comp} is normalized to values between 0 and 1. To ensure material feasibility in the finite element solver, a constraint was imposed such that the inverse of the orthotropic material stiffness matrix can be solved. The bounds of the material properties were limited based on the preliminary analysis presented in Section 5.3.2. Additionally, a large discrepancy between stiffness matrix entries results in numerical failure in the finite element solver. Auxetic materials, such as re-entrant honeycombs, are considered in the problem formulation by allowing negative values for Poisson's ratio.

6.1.2 MOO Algorithm

To solve the multi-objective optimization problem formulated in Equation (6.1), the non-dominated sorting genetic algorithm (NSGA-II) was used [28]. NSGA-II is advantageous over non-evolutionary approaches as it does not require knowledge of the gradient or Hessian of the objective function, which is difficult to compute when finite element methods are required to compute the objective function. Additionally, the population based approach of evolutionary algorithms allow for the Pareto front to be computed in one single optimization simulation run. NSGA-II has been shown to outperform other multi-objective evolutionary algorithms (e.g. MOGA) in terms

of efficiently finding a diverse set of solutions and in converging near the true Pareto-optimal set [28], as it uses both elitism and crowd distancing. The steps of the NSGA-II are described below, while more details can be found in [28]:

- i A random parent population is created, P_0 .
- ii Each solution of the initial parent population, P_0 , is assigned a fitness level based on the non-domination level. Elitism is introduced after the initial generation.
- iii A binary tournament selection, recombination and mutation operators are used to create the offspring Q_0 the size of N_p . This gives a new combined population R_0 , consisting of P_0 and Q_0 .
- iv A fast non-dominated sorting approach is used to: a) find the domination count n_p , which is the number of solutions which dominate the solution p ; and b) the set of solutions S_p that the solution p dominates. This step ranks each member of the population of solutions into dominated fronts.
- v Crowding distance is computed to preserve diversity in the non-dominated set of solutions. An estimation on density of solutions surrounding a particular solution in the population is made by calculating the average distance between it and surrounding points.
- vi The solutions are then ranked first based on their non-domination fronts, then based on their crowding distance such that non-domination solutions are preferred that are located in lesser crowded regions.

- vii Then, a binary tournament selection, recombination and mutation operators are used to create an offspring population Q_t of size N_p . This selection operator is now based both on non-domination and crowding distance.
- viii Steps 4-7 are repeated for a specified number of generations.

While NSGA-II offers considerable advantages in terms of simplicity, efficiency and diversity of solutions; a large number of function evaluations are still required to converge to the Pareto front. Additionally, unlike gradient-based approaches, NSGA-II cannot prove mathematically that the true Pareto set of solutions have been found. The parameters outlined in Table 6–2 were used in the wheel MOO NSGA-II algorithm. The parameters were tuned heuristically such that a large population is searched at each generation, while the optimal solutions are found within 1000 function evaluations by modifying the mutation and crossover parameters.

Table 6–2: NSGA-II Algorithm Parameters

Parameter	Value
Crossover distribution index	20
Mutation distribution index	20
Crossover probability	0.8
Mutation probability	0.2
Tournament size	2
Population size	10
Maximum function evaluations	1000

6.1.3 Wheel MOO Results

Two separate wheel optimization problems were formulated to find the optimal homogeneous orthotropic material properties. First, a wheel composed of a single

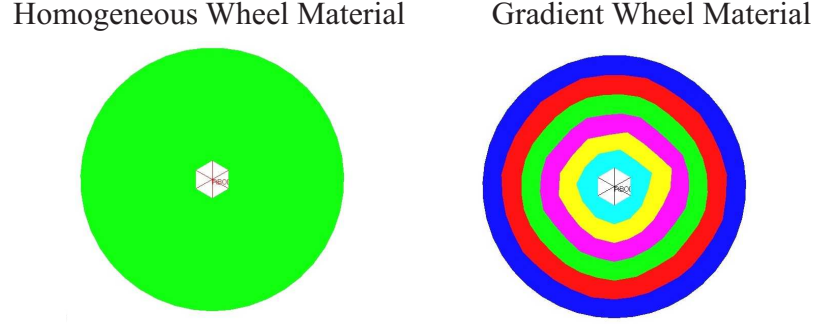


Figure 6.2: Homogeneous and Gradient Material Wheels

homogeneous material is solved. A gradient internal structure of six distinct material types are used for the wheel elements in the second problem, however the optimal solutions were not found given the computational effort required. Figure 6.2 depicts the homogeneous and gradient material wheel concepts.

Single layer wheel MOO results

The results of the single material wheel MOO, after 1000 function iterations, are depicted in Figure 6.3. The total simulation time was estimated at 407hrs on a four core 2.66GHz processor with 4GB RAM, or approximately 17 days. Each point on the objective function space represents a distinct solution found by the NSGA-II algorithm. The results shown in Figure 6.3 are normalized according to the largest value of each objective function. Given the conflicting nature of wheel elasticity, a set of trade-off solutions are selected for further investigation which achieve the maximum lateral and torsional stiffness, while minimizing vertical stiffness. Six a posteriori trade-off solutions are identified by coloured circular markers which represents the solution of: the minimum lateral displacement (ML), the maximum contact

area (MA), the minimum torsional displacement (MT) and three trade-off solutions (TO-1,-2,-3) consisting of a weighted sum of the three objective functions as shown in Equation (6.4). The values of the weighting factors for each objective function in the trade-off solutions are outlined in Table 6–3.

$$TO = \min_k \frac{1}{k} \sum_{k=1}^3 w_k y_k \quad (6.4)$$

where $\sum_{n=1}^3 w_k = 1$

Table 6–3: Weighting coefficients for trade-off solutions

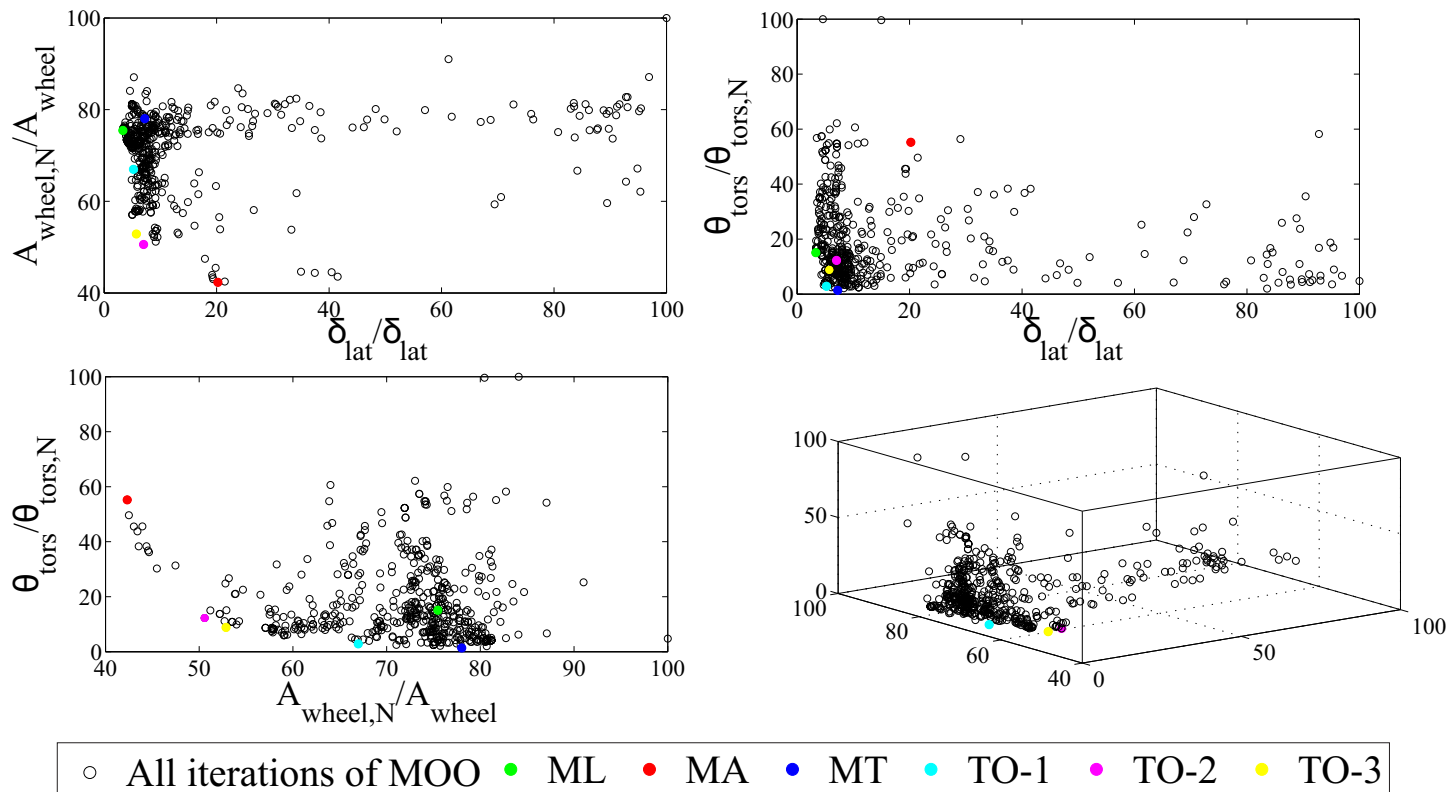
Solution	w_1	w_2	w_3
Trade-off 1 (TO-1)	1/6	1/6	2/3
Trade-off 2 (TO-2)	1/6	2/3	1/6
Trade-off 3 (TO-3)	0.25	0.5	0.25

The objective space can be gleaned from Figure 6.3. The conflicting nature of maximizing contact area and minimizing torsional displacement is characterized by a clear Pareto frontier. All solutions of interest, except ML, lay on the $A_{wheel}-\theta_{tors}$ objective space Pareto front. A good spread of solutions in the Pareto front is achieved in all three objective spaces, which illustrates NSGA-II’s ability to sort based both on non-dominance and crowding distance.

In the $\delta_{lat}-A_{wheel}$ objective space, TO-2, TO-3, MA and ML lay on the Pareto front. TO-3, which favours θ_{tors} , and MT are not of interest in the $\delta_{lat}-A_{wheel}$ objective space. The conflict between objectives δ_{lat} and A_{wheel} not clear. Since properties in

Figure 6.3: Single Layer MOO Results

120



the material stiffness matrix affect wheel elasticity, this suggests that some stiffness matrix elements influencing contact area do not affect lateral displacement. The influence of material properties on elastic wheel behaviour are discussed later in this section, which gives additional insight into optimal wheel design. It is important to note that the design variables describing the material properties of a homogeneous orthotropic material are defined independently here. Invariably, the elements of the stiffness matrix of a real orthotropic material, such as a cellular or composite material, will be coupled by their geometry. This does indicate, however, that three dimensional cellular materials which can be tailored to achieve directional compliance are of interest for cellular wheel designs.

The conflict between δ_{lat} and θ_{tors} is also not apparent. Although TO-3, ML and TO-1 lay on the δ_{lat} - θ_{tors} Pareto front, the set of solutions appear to form vertical and horizontal lines at both δ_{lat} and θ_{tors} minima. Given the evolutionary nature of NSGA-II, it is possible that with an increase in the number of function evaluations, a single optimal solution would emerge in the δ_{lat} - θ_{tors} objective space. However this would require a significant amount of computational investment. Nonetheless, a lack of conflict in the objective space indicates the independent or complimentary behaviour of the design variables. The design variable vectors of the six solutions of interest are outlined in Table 6–4, while their objective function values are illustrated in Figure 6.4.

Minimizing lateral displacement results in a lateral deformation of 1.1cm, a torsional displacement of 0.63° and a contact patch of $0.029m^2$. MA yields an area

Table 6-4: Trade-off solutions from single layer MOO

Solution	$\bar{\rho}^*$	E_{xx}^* (MPa)	$\bar{\nu}_{xy}^*$	E_{yy}^* (MPa)	$\bar{\nu}_{yz}^*$	E_{zz}^* (MPa)	$\bar{\nu}_{zx}^*$	G_{xy}^* (MPa)	G_{yz}^* (MPa)	G_{zx}^* (MPa)
ML	7.7	0.02	0.09	0.63	0.20	0.82	0.22	0.60	0.04	1.41
MA	51.0	0.02	0.11	1.12	0.23	0.01	0.08	2.33	0.01	1.57
MT	20.3	1.13	0.13	1.67	0.24	0.61	0.08	2.08	1.14	2.01
TO-1	31.7	0.02	0.11	0.63	0.20	0.81	0.10	0.02	0.01	0.26
TO-2	61.7	0.02	0.09	0.29	0.22	0.68	0.04	0.02	0.01	0.01
TO-3	51.5	0.02	0.09	1.1	0.22	0.68	0.04	0.05	0.01	0.01

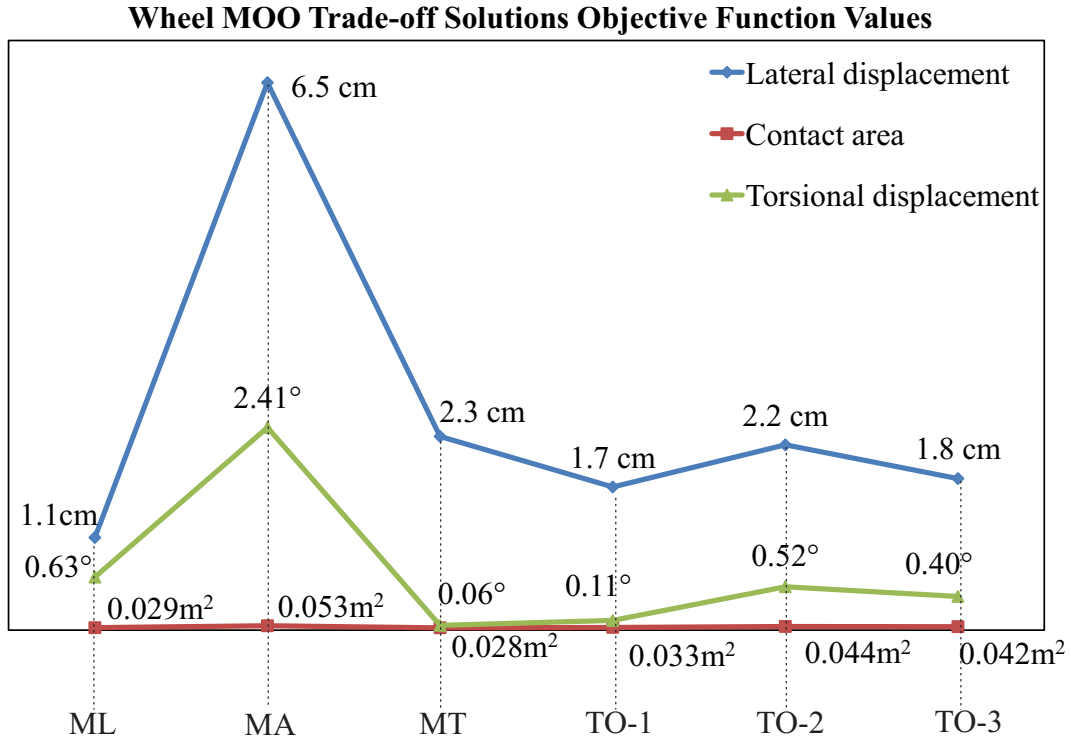


Figure 6.4: Trade-off Solutions Objective Function Values

of $0.053m^2$, nearly double the ML solution contact area. Consequently, a six fold increase in lateral displacement (6.5cm) and a fourfold increase in torsional displacement (2.4°) is seen in the MA solution. The MT solution yields a 0.06° torsional displacement, with a lateral displacement and contact area of 1.7cm and $0.0285m^2$ respectively. The trade-off solutions offer a compromise between the objectives. The lateral displacements of the trade-off solutions lay within a 5mm range, while no torsional displacement exceeds 0.5° . A more significant variation is apparent in the contact area, most notably for TO-1. As described previously, TO-1 emphasizes a lower torsional displacement, which sacrifices contact area by 33% and 27% compared to TO-2 and TO-3 respectively. These results highlight the conflicting nature of maximizing contact area and minimizing torsional displacement.

The material properties consequence on wheel performance can be gleaned directly from Table 6–4. The density of the material appears to play a role in minimizing lateral displacements, as seen in the ML solution. Reducing material density generates a lower load on the wheel. Increasing the contact patch is also directly affected by an increase in material density, resulting in a larger vertical deformation and therefore contact area. A low elastic modulus signifies a reduction in stiffness, which also benefits contact area. This is clear from Table 6–4, where the optimal elastic modulus in the z -direction is lowest for the MA solution. An increase in shear modulus contributes to lowering torsional displacements, as seen in the MT solution. The trade-off solutions in Table 6–4 give insight into the relationship between objective functions and design variables as well. TO-1 has the highest G_{zx} of the trade-off solutions as it emphasis minimizing torsional displacement. TO-3 has higher G_{xy}

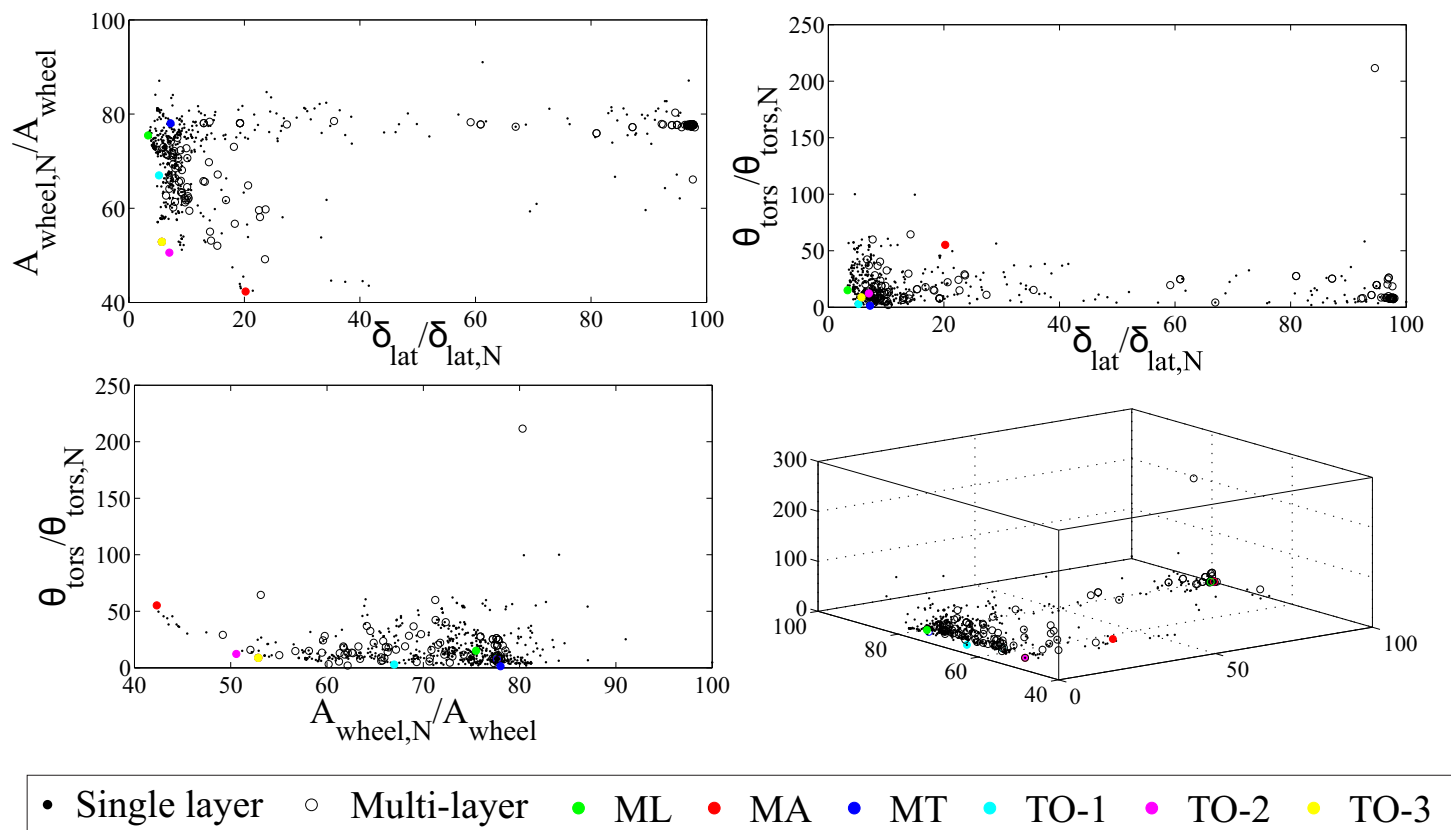
and E_{yy} than TO-2 given the weighted importance on minimizing torsional and lateral displacements over contact area. The most evident conflict is seen in the elastic moduli and shear moduli in the x - z plane. Minimizing torsional displacement favours higher values of both G_{zx} and E_{zz} , resulting in a stiffer wheel. Conversely, low values of G_{zx} and E_{zz} in a larger wheel-ground contact area. Optimized Poisson's ratio does not vary significantly for any solutions of interest. In sum, the wheel MOO results demonstrate that directional compliance of the orthotropic material dictates macroscopic elastic wheel behaviour, and implicitly, rover and mission performance.

Multi-layer wheel MOO results

Functionally gradient lattice materials are widely investigated in cellular material design [66]. Given the radial symmetry of the wheel, six layers of different materials properties were selected arbitrarily for a gradient cellular concept, as depicted in Figure 6.2. The resulting multi-layer MOO problem contains 60 design variables (i.e. 6x10 material properties to define an orthotropic material). The maximum number of objective function evaluations set at 1000 was effective at finding the Pareto optimal solutions for the single material case presented previously. For comparison, the multi-layer wheel MOO results are depicted by circular markers in Figure 6.5 along with the single layer MOO results and trade-off solutions, depicted by black filled and coloured circular markers respectively. The results are normalized to the single layered wheel MOO results.

The size of the design variable vector reduces the effectiveness of the NSGA-II algorithm. This is evident in Figure 6.5, where no multi-layered wheel MOO solutions appear to be contained in the Pareto front found in the single layer wheel, with the

Figure 6.5: Multi-Layer MOO Results
125



same number of function evaluations. The results shown are inconclusive, and it is unclear whether a multi-layer composite wheel would yield improved results over a single layer wheel. Significantly more function evaluations are required to adequately determine the objective function space. 1000 function evaluations appeared to yield a Pareto front for the single layered results. With the increase in the design variable vector size, a total of 6000 function evaluations are estimated to take 1995 hours or approximately 2 months and 23 days on a platform with similar computational power.

6.2 Cellular Material Optimization

The cellular material optimization problem is described in this section, where optimal unit cell designs are solved to meet the optimal homogeneous material properties of the cellular wheel.

6.2.1 Unit Cell Designs

As discussed in Chapter 2, lattice materials microstructure can be related to their macroscopic mechanical properties by closed-form expressions and numerical techniques homogenization techniques. The intent of this research is to develop a methodology to optimize wheel designs given both system and component level requirements. Consequently, developing homogenization techniques to obtain macroscopic properties of novel cellular materials is considered out of scope. Nonetheless, the wheel MOO results presented previously indicate that developing directionally compliant cellular topologies is of interest for future work in cellular wheel design.

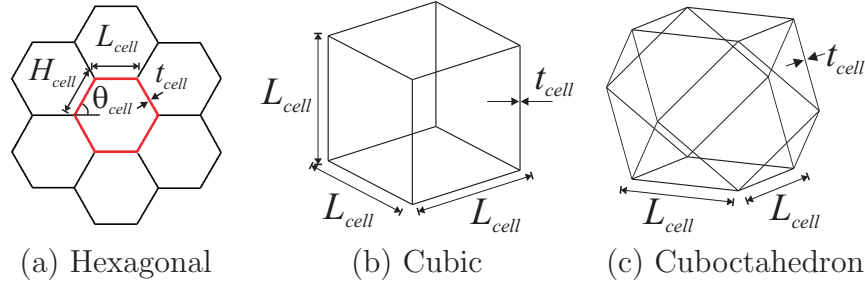


Figure 6.6: Cellular Wheel Unit Cell Topologies of Interest

To obtain the optimal lattice microstructure, both macroscopic and microscopic properties are required. Macroscopic material properties of the topologies should match those found by the wheel MOO, while microscopic stresses and forces acting on the cell microstructure must be kept below the failure thresholds. Two failure modes are considered here, yield and buckling of the cell walls. Open cells are considered here as they achieve lower stiffness than closed-cell topologies, as shown in [114].

The unit cells investigated are limited to those with closed-form expressions of the micro and macroscopic material properties. These include a hexagonal 2D unit cell, as well as the 3D open-cell cubic and cuboctahedron unit cells illustrated in Figure 6.6. As discussed in Section 5.3.2, these cell topologies yield lower values for elastic and shear moduli than the Kagomé, diamond, mixed B, FCC and BCC. The closed-form expressions, provided by [45] and [114], which relate unit cell design with homogeneous mechanical properties and express internal forces in the unit cells in terms of the macroscopic loading on the homogeneous material are outlined in detail in Appendix B.

It should be noted that although these closed-form expressions allow for a direct relationship between unit cell design variables and macro and microscopic material

properties, they are limited in scope. Directional symmetry is assumed in the formulation for simplicity, where the cell wall thickness' and lengths are equal in the unit cell. This need not be true in numerical homogenization techniques. Additive manufacturing techniques for lattice materials also do not limit variable cell wall length or thickness. As such, the cellular material optimization presented here does not provide an inclusive analysis of all possible unit cell configurations. Nonetheless, as it will be presented in subsequent sections, insight into cellular material design for cellular wheel concepts is still provided.

6.2.2 Cellular Material Optimization Problem Formulation

The goal of the cellular material optimization is to find the unit cell design variables such that the macroscopic material properties of the cellular material match those of the optimal homogeneous wheel MOO results. Additionally, the cellular material must withstand the loading conditions imposed on the elements of the homogeneous material in the wheel MOO simulation. The cellular material optimization problem can be formulated as follows:

$$\begin{aligned}
&\text{Find} && \mathbf{x}_{cell} = [t_{cell}, L_{cell}, \theta_{cell}, H_{cell}]^T \\
&\text{to minimize} && e_s = \frac{1}{|\mathbf{x}_{comp}|} \sum_{i=1}^{|\mathbf{x}_{comp}|} (x_{i,comp}^* - x_{i,comp})^2 \\
&\text{subject to} && \sigma_{VM} \leq \sigma_Y \\
&&& \sigma_{axial} \leq \sigma_{buckling} \\
&&& 0.35mm \leq t_{cell} \leq 8mm \\
&&& L_{cell} \leq \frac{D_W - D_h}{10}
\end{aligned} \tag{6.5}$$

where \mathbf{x}_{cell} is the unit cell design variable vector described in Figure 6.6 for each combination of base material \mathbf{x}_{mat} and unit cell type \mathbf{x}_{type} , e_s represents the average error between the optimal ($x_{i,comp}^*$) and feasible material properties ($x_{i,comp}$), and σ_{VM} and σ_{axial} represent the von Mises and axial stress in the cell struts of the unit cells respectively. σ_Y and $\sigma_{buckling}$ describe the yield stress and buckling limit of the base material and cell struts. Cell relative density $\bar{\rho}$ is not considered in \mathbf{x}_{comp} as it can be easily computed as a function cell topology. θ_{cell} and H_{cell} are used in describing the hexagonal unit cell. The closed-form expression of the homogeneous macroscopic properties described in Appendix B are used to compute the feasible cellular material properties $x_{i,comp}$. This permits the objective function e_s , which is a least square error between the feasible and ideal wheel material, to be computed. To verify the failure in the unit cells, the resulting forces in the beam elements of the unit cell from the homogeneous wheel simulation must be found. The formulation relating microscopic beam (or strut) forces F_b in beam b for each beam in the cubic and cuboctahedron unit cells to the macroscopic strain ϵ_h is available in Appendix B. In the cellular material optimization routine, F_b is verified to ensure that the microscopic forces do not exceed the yield (σ_Y) and buckling stress ($\sigma_{buckling}$), for each beam element b of each unit cell, for each homogenous element h at every time step of both wheel simulations. For hexagonal unit cells, Ashby and Gibson developed the equivalent macroscopic stress to ensure buckling and yield in the cell walls do not occur [45]. This formulation is also available in Appendix B.

A bound on the unit cell design variables was imposed to ensure the micro/macro scale assumption for homogenization is valid. In this case, a maximum unit cell size

of 1/10th of radius composed of the cellular material. For the 2D cellular unit cells, the objective function was reduced in complexity to account for 2D wheel properties only: \bar{E}_{xx} , \bar{E}_{zz} , \bar{G}_{zx} , $\bar{\nu}_{zx}$. The base material properties of the unit cell, in this case 304 Stainless Steel, are available in Table 6–5.

Table 6–5: 304 Stainless Steel Material Properties

Property	Value
Density	7804 Kg/m ³
Young’s Modulus	210 GPa
Poisson’s ratio	0.33
Yield Stress	860 MPa

The single objective optimization problem formulated in Equation (6.5) is a non-linear over-determined optimization problem, with inequality constraints. Given the complexity of the of the material constitutive model formulations, as seen in Appendix B, the gradient and Hessian of the objective function are not suitable to provide a priori into the optimization algorithm. The constraints are handled by solving the Karush-Kuhn-Tucker (KKT) necessary conditions, using Sequential Quadratic Programming (SQP). SQP is a quasi-Newton method, which is iterative in nature. The Hessian of the Lagrangian function is estimated by the Broyden-Fletcher-Goldfarb-Shanno (BFGS) method, which is used to generate a quadratic programming sub-problem to form a search direction for a line search procedure. More details on the optimization algorithm can be found in [88].

6.2.3 Cellular Material Optimization Results

The six results of interest from the wheel MOO, presented in Table 6–4, were used to formulate six optimization problems. For each trade-off solution, the design

variables describing 3D and 2D unit cells are solved.

For the 3D unit cells, the optimal design variables were identical for each of the six solutions of interest: $t_{cell} = 0.35mm$ and $L_{cell} = 3cm$. The error in the homogeneous properties for each solution is shown in Table 6–6. Negative error values are used to highlight cases where the cellular material optimization result are below that of the target value from the wheel MOO.

The results in Table 6–6 show a large discrepancy between the target homogeneous and feasible material properties. The feasible solutions presented are limited by the unit cells investigated, as well as the material constitutive models. As discussed in Chapter 5, cubic unit cells achieve low shear stiffness while the axial stiffness remains high. Therefore, the solutions to the cubic unit cell are skewed to minimize the elastic modulus error, resulting in a shear modulus below the target value. The cuboctahedron achieves a lower axial stiffness than shear, as such; the error in elastic modulus is lower than in the shear modulus in Table 6–6.

In [111], an optimization of the TWEEL’s shear band was conducted to determine a target effective shear modulus for a hexagonal honeycomb. To illustrate the ability of the 3D unit cells to achieve a single directional stiffness property, the objective function of the cellular material optimization presented in Equation (6.5) is modified. The cubic unit cell can be optimized to meet the least square error in shear (\bar{G}_{zx}^*), while the cuboctahedron unit cell is tailored to match the effective elastic modulus \bar{G}_{zz}^* . The results for the cubic cell are presented in Table 6–7.

Table 6–6: Cubic and Cuboctahedron cellular material optimization solutions

Solution	$e_{E_{xx}}$ (%)	$e_{\nu_{xy}}$ (%)	$e_{E_{yy}}$ (%)	$e_{\nu_{yz}}$ (%)	$e_{E_{zz}}$ (%)	$e_{\nu_{zx}}$ (%)	$e_{G_{xy}}$ (%)	$e_{G_{yz}}$ (%)	$e_{G_{zx}}$ (%)
Cubic, ML	1.3x10 ⁵	-100	4459	-100	3408	-100	-100	-95	-100
Cubic, MA	1.4x10 ⁵	-100	2444	-100	2.4x10 ⁵	-100	-100	-85	-100
Cubic, MT	2433	-100	1608	-100	4588	-100	-100	-100	-100
Cubic, TO-1	1.4x10 ⁵	-100	4457	-100	3416	-100	-91	-87	-99
Cubic, TO-2	1.3x10 ⁵	-100	9716	-100	4109	-100	-92	-85	-86
Cubic, TO-3	1.3x10 ⁵	-100	2484	-100	4109	-100	-96	-85	-86
Cuboc, ML	-63	460	-99	145	-99	123	1580	2.8x10 ⁴	617
Cuboc, MA	-59	354	-99	118	-32	551	334	7.6x10 ⁴	544
Cuboc, MT	-99	299	-100	105	-99	544	385	790	403
Cuboc, TO-1	-61	354	-99	145	-99	417	4.5x10 ⁴	7.0x10 ⁴	3754
Cuboc, TO-2	-63	457	-97	124	-99	1287	4.4x10 ⁴	7.7x10 ⁴	7.4x10 ⁴
Cuboc, TO-3	-62	457	-99	124	-99	1287	2.2x10 ⁴	7.7x10 ⁴	7.4x10 ⁴

Table 6–7: Cubic cellular material solutions for \bar{G}_{zx}

Solution	$t_{cell}(mm)$	$L_{cell}(cm)$	$e_{G_{zx}}$
Cubic, ML	1.12	1.85	0.0%
Cubic, MA	1.28	2.05	0.0%
Cubic, MT	1.39	2.09	0.0%
Cubic, TO-1	0.59	1.50	0.0%
Cubic, TO-2	0.35	1.84	0.0%
Cubic, TO-3	0.35	1.84	0.0%

The results indicate that the cubic unit cell achieves the trade-off solution shear modulus \bar{G}_{zx} . The results from the cuboctahedron unit cell optimization also show good agreement with meeting \bar{E}_{zz} as shown in Table 6–8.

Table 6–8: Cuboctahedron cellular material solutions for \bar{E}_{zz}

Solution	$t_{cell}(mm)$	$L_{cell}(cm)$	$e_{E_{zz}}$
Cuboc, ML	0.5	1.36	0.0%
Cuboc, MA	0.35	2.73	0.0%
Cuboc, MT	0.56	1.65	0.0%
Cuboc, TO-1	0.5	1.35	0.0%
Cuboc, TO-2	0.98	2.79	1.1%
Cuboc, TO-3	1.1	3.00	23.0%

The 2D hexagonal cell is optimized in a simplified cellular material optimization problem to solve for the 2D material properties shown in Equation (6.3). The solutions are presented in Table 6–9. Negative error values are used in Table 6–9 to highlight solutions below the target from the wheel MOO.

The hexagonal unit cell is better suited to attain the directional stiffness requirements of the cellular wheel. For the MA and MT cases, the axial and shear moduli errors are relatively low compared to the cubic and cuboctahedron results presented

Table 6–9: Hexagonal cellular material optimization solutions

Solution	t_{cell} (<i>mm</i>)	L_{cell} (<i>cm</i>)	H_{cell} (<i>cm</i>)	Angle ($^{\circ}$)	$e_{E_{xx}}$ %	$e_{\nu_{xz}}$ %	$e_{E_{zz}}$ %	$e_{G_{xz}}$ %
Hex, ML	0.35	1.23	2.79	35.1	1800%	757%	-49%	0%
Hex, MA	0.35	1.17	2.99	37.9	-20%	798%	33%	0%
Hex, MT	0.39	1.36	2.10	33.0	-23%	583%	43%	0%
Hex, TO-1	0.39	3.00	3.00	28.3	1871%	640%	-49%	0%
Hex, TO-2	0.35	3.00	3.00	28.0	1501%	772%	-48%	1255%
Hex, TO-3	0.35	3.00	3.00	28.0	1537%	772%	-48%	1255%

in Table 6–6. The solutions converge to the target homogeneous shear modulus \bar{G}_{zx}^* for all solutions of interest, except TO-2 and TO-3. The elastic modulus error $e_{E_{zz}}$ is below 50% in all solutions, whereas Poisson’s ratio error, $e_{\nu_{xz}}$, is high in all cases. The results in Table 6–9 confirm the selection of a hexagonal microstructure in the design of cellular wheels in [62] and [78].

The wheel MOO results illustrated the importance of the elements of the homogeneous orthotropic stiffness matrix $\bar{\mathbf{K}}$ in achieving system level performance. The material constitutive models limit the complexity of the unit cells investigated here, as the cell wall lengths and thickness are assumed identical for each cell wall of the unit cell. Moreover, alternative unit cell designs may offer more suitable directional stiffness properties. As such, the success of the unit cells investigated are limited in achieving $\bar{\mathbf{K}}^*$. Nonetheless, some wheel designs with cubic cells found here are modelled subsequently for results validation.

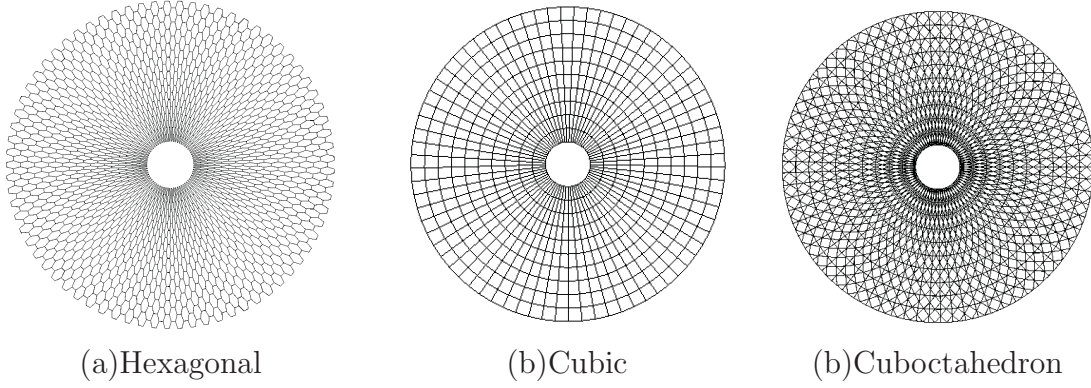


Figure 6.7: Cellular Wheels

6.3 Error Analysis

The effectiveness of the proposed approach to optimize wheel structural design for mission objectives is verified by error analyses between system-component levels and within the component level. These error analyses, outlined in Figures 3.1 and 3.3 respectively, is presented in this section along with verification of the rigid ground assumption.

6.3.1 Component Level Error Analysis

At the component level, the cellular material optimization results are verified by comparing the objective function errors e_k between the homogeneous wheel trade-off solutions y_k^* and feasible cellular wheels $y_{k,feasible}^*$. $y_{k,feasible}^*$ is computed by direct modelling of the cellular wheel in a FEA of the two wheel drive scenarios described in Section 6.1. Figure 6.7 presents the cellular wheel concepts generated by the hexagonal, cubic and cubocatahedron unit cells. Given the computational effort involved in modelling and simulating the wheels, only the cubic unit cell results were verified.

The deformed cubic cellular wheel, with $t_{cell} = 0.35mm$ and $L_{cell} = 3cm$, at one

time step of the FE is illustrated in Figure 6.8(a). As discussed in Section 6.2.3, the unit cell designs are limited by the material constitutive models. As such, the optimal cubic cellular wheel for all six trade-off solutions of interest is identical, and identified by e_s . The objective function values for e_s , as shown in Table 6–10, are $\delta_{lat,MAX} = 10.7cm$, $A_{wheel,RMS} = 0.125m^2$ and $\delta_{tors,MAX} = 13^\circ$. From the wheel MOO results presented in Figure 6.4, a large discrepancy is seen between the cellular material solution and trade-off solution targets. The optimal objective function values from Figure 6.4 are used in the error estimate of the e_s case in Table 6–10, since the cubic cell design is identical for each of the six trade-off solutions from the wheel MOO. In Figure 6.4, the optimal objective function values are $\delta_{lat,MAX} = 1.1cm$, $A_{wheel,RMS} = 0.053m^2$ and $\delta_{tors,MAX} = 0.06^\circ$. Evidently, an increase in contact area is attained at the expense of high torsional and lateral displacements. The cubic cellular material minimizes the total error in the objective function by reducing the shear stiffness, leading to large deformations. It should be noted, however, that the von Mises stress remains below the material yield limit ensuring mechanical reliability.

To verify the effect of the simplified cellular material optimization problem, the cubic cell designs shown in Table 6–7 which achieve \bar{G}_{zx}^* were also simulated. The objective function results from direct modelling of the Cubic- \bar{G}_{zx}^* cases are also shown in Table 6–10. The error, however, is computed for individual trade-off solutions, unlike the e_s case discussed previously. Negative errors indicate that objective function values computed by direct modelling of the cellular wheel are below the target value from

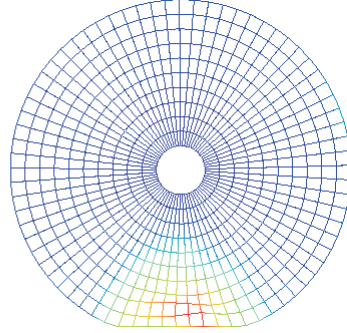
the wheel MOO. The deformed wheels at one time step of the simulation are illustrated in Figure 6.8.

Table 6–10: Cubic Wheel Designs Component Level Error Analysis

Solution	$\delta_{lat,max}$ (m)	$A_{wheel,RMS}$ (m ²)	$\theta_{tors,max}$ (°)	e_{y1}	e_{y2}	e_{y3}
Min e_s	107.0	0.125	13.00	873%	138%	296%
ML- \bar{G}_{zx}^*	0.0	0.013	0.05	-100%	-56%	-92%
MA- \bar{G}_{zx}^*	0.0	0.020	0.04	-100%	-43%	-98%
MT- \bar{G}_{zx}^*	0.0	0.015	0.03	-100%	-47%	-48%
TO-1- \bar{G}_{zx}^*	0.7	0.018	0.40	-96%	-47%	249%
TO-2- \bar{G}_{zx}^*	4.0	0.018	3.30	-82%	-60%	532%
TO-3- \bar{G}_{zx}^*	4.0	0.018	3.30	-78%	-58%	713%

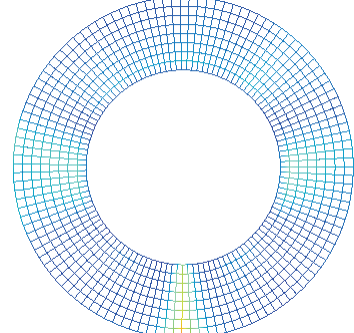
From Table 6–10, it is evident that orthotropic material properties play a significant role in achieving optimal elastic behaviour y_k . Minimizing total material property error e_s was poor at meeting y_k . A large contact area was achieved at the expense of high torsional and lateral deformation. Optimizing the cubic unit cell for \bar{G}_{zx}^* reduces the error in y_k , particularly for lateral and torsional displacement. It should be noted, however, that the Cubic- \bar{G}_{zx}^* wheels were simplified by increasing the hub diameter to reduce the number of elements, making the simulations computationally feasible. In all six cubic cellular wheel solutions which minimize \bar{G}_{zx}^* , the lateral displacement is lower than the target. Therefore, the large negative value for e_{y1} does not limit wheel performance. Conversely, the contact area achieved by the cubic wheels is below the target value. Torsional displacement for MA, ML and MT is below the target value, whereas it is higher for TO-1, TO-2 and TO-3.

Von Mises
Simple Average
3.763E+08
3.013E+08
2.263E+08
1.513E+08
7.628E+07
1.283E+06



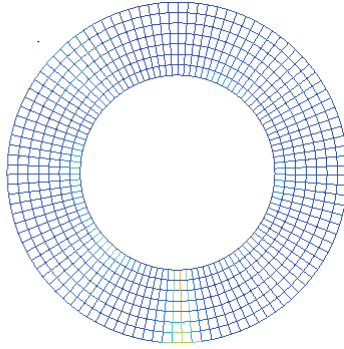
(a) Nominal cubic cell solution: e_s case

Von Mises
Simple Average
1.446E+07
1.157E+07
8.674E+06
5.783E+06
2.891E+06
0.000E+00



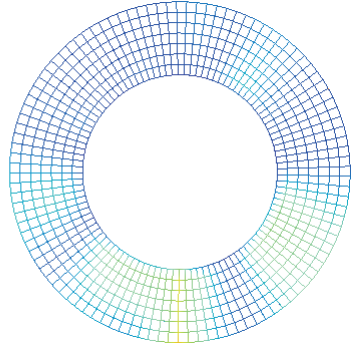
(b) $ML-G_{zx}^*$ case

Von Mises
Simple Average
9.979E+06
7.983E+06
5.987E+06
3.991E+06
1.996E+06
0.000E+00



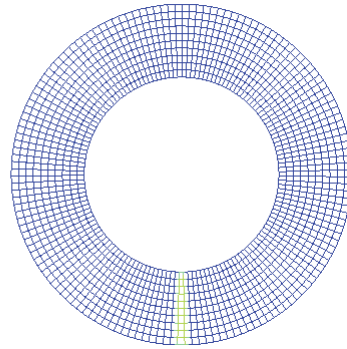
(c) $MA-G_{zx}^*$ case

Von Mises
Simple Average
3.559E+06
2.847E+06
2.135E+06
1.424E+06
7.118E+05
0.000E+00



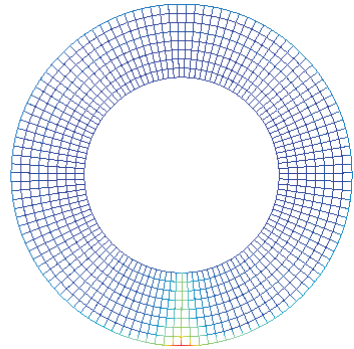
(d) $MT-G_{zx}^*$ case

Von Mises
Simple Average
1.168E+07
9.344E+06
7.008E+06
4.672E+06
2.336E+06
0.000E+00



(e) $TO-1-G_{zx}^*$ case

Von Mises
Simple Average
1.088E+08
8.712E+07
6.547E+07
4.381E+07
2.215E+07
4.931E+05



(f) $TO-2/3-G_{zx}^*$ case

Figure 6.8: Optimal Cubic Wheel Designs

The error between the objective functions suggest that the effective orthotropic material properties are necessary to meet the target performance. Optimizing unit cells for axial or shear modulus alone is insufficient for cellular wheel design. As described above, the cubic unit cell is appropriate when low shear modulus is desired, whereas cuboctahedron unit cells achieve low elastic modulus. Hexagonal cells have superior elastic and shear compliance, and are better suited for compliant wheel applications. Investigating additional unit cell topologies requires more sophisticated homogenization techniques than employed here.

6.3.2 System-Component Level Error Analysis

The optimal elastic behaviour of the wheel from the system level was considered implicitly by the peak lateral deformation, average contact area and peak torsional deformation metrics at the component level. To verify the effectiveness of the trade-off solutions found at the component level to achieve system level performance, coupling equations q_k are used. In the case of lateral and torsional stiffness, the elastic wheel pseudo-model in Equations (4.4) and (4.5) presented in Chapter 4 are used respectively. These equations are modified to account for the component level results below:

$$q_1 : y_{1,sys}^* = \delta_{lat} = R_L/K_L \quad (6.6)$$

$$q_3 : y_{3,sys}^* = \theta_{tors} = T_w/K_T \quad (6.7)$$

The vertical stiffness in the compliant wheel pseudo-model and numerical cellular

wheel are coupled by the ground contact patch. The ground contact patch is computed directly in the numeric analysis, whereas it can be approximated by combining Equations (4.2) and (4.7) into:

$$q_2 : y_{2,sys}^* = 2\sqrt{D_w(K_V/W_w) - (K_V/W_w)^2 b_w} \quad (6.8)$$

This method is approximate, as a deformable soil is considered at the system level and rigid soil at the component level. This implies that qualitative correlation between the system and component level is achieved. Finite element modelling of a deformable soil with a compliant cellular wheel is required for adequate system-component level verification. Preliminary work towards simulating a homogeneous wheel on a deformable soil is presented in Section 6.3.3. Nonetheless, to verify the component-system level correlation, the error between the trade-off solutions $y_{k,comp}^*$ and system analysis $y_{k,sys}^*$ is provided in Table 6–11. The target values from the system level analysis are $y_{1,comp}^* = 5mm$, $y_{2,comp}^* = 0.151m^2$ and $y_{3,comp}^* = 0.006^\circ$.

Table 6–11: System-Component Level Verification

Solution	$\delta_{lat,max}$ (mm)	$A_{wheel,RMS}$ (m ²)	$\theta_{tors,max}$ (°)
Target ($y_{k,sys}^*$)	5.00	0.151	0.006
Cubic Min e_s	107.00	0.125	13.00
Cubic ML- \bar{G}_{zx}^*	0.05	0.013	0.05
Cubic MA- \bar{G}_{zx}^*	0.05	0.062	0.05
Cubic MT- \bar{G}_{zx}^*	0.06	0.015	0.03
Cubic TO-1- \bar{G}_{zx}^*	0.07	0.037	0.40
Cubic TO-2- \bar{G}_{zx}^*	4.00	0.018	3.26
Cubic TO-3- \bar{G}_{zx}^*	4.00	0.018	3.26

Since the system level optimization limited the bounds of the lateral stiffness, where as it was not limited by the component level analysis, the cubic cell achieves a lower lateral displacement in all Cubic- \bar{G}_{zx}^* cases. Torsional stiffness, on the other hand, is exceeded by one order of magnitude for ML, MA and MT, two orders of magnitude higher for TO-1 and over three orders of magnitude in TO-2/3. Convergence to the target torsional displacement of 0.006° is limited as result of a high torsional stiffness target at the system-level. The resulting component level torsional displacement may in fact be acceptable.

The cubic unit cell is poor at achieving high ground contact area when optimizing for the shear modulus. As such, the error is high in Table 6–11. The cubic wheel e_s case, which minimizes the effective material properties error at the component level analysis, results in an error of only 17%. However, the lateral and torsional stiffness error suffer accordingly, yielding values two and four orders of magnitude higher, respectively, than the system level targets. In the case of MA- \bar{G}_{zx}^* , where the shear modulus is optimized, the area error is lower than in other Cubic- \bar{G}_{zx}^* cases at 59%. The system-component level error analysis demonstrates that although some objectives are met, significant errors exist due to the unit cells considered. As stated earlier, more sophisticated constitutive material models are required to investigate alternative unit cell designs capable of meeting the system level target performance. Since the methodology is a two-step sequential approach, coupling between the component and system level analysis is considered only implicitly. Additionally, error convergence is not addressed within the design framework itself. Extensions of the

current methodology to address error convergence by means of multi-disciplinary optimization methods is discussed in Chapter 7.

6.3.3 Rigid Ground Verification

Modelling deformable soil using the FEM assumes the soil behaves as a continuum, as discussed in Chapter 2. Since the lunar soil behaves like a granular solid, this assumption is inherently inaccurate and considerable model parameter tuning is required to ensure simulation results accurately represent physical behaviour. Furthermore, FE modelling of wheel-soil behaviour is computationally expensive.

To verify the applicability of modelling the soil as a continuum in the wheel MOO, the drucker-prager material model built into the RADIOSS explicit FE solver is used to model the lunar soil. A reduction in model size is achieved by considering only 1/10th the width of the flexible wheel. The values of lunar soil simulant GRC-1 are considered, as described in [85]. The soil parameters used in the model are outlined in Table 6–12, while the pressure-strain relationship of the lunar soil simulant GRC-1 is compared to common sandy soils in Figure 6.9.

Table 6–12: GRC-1 Lunar Regolith Soil Simulant Properties [85]

Parameter	Value
Density	1690 Kg/m ³
Young’s Modulus	182 MPa
Poisson’s ratio	0.28
Angle of Friction	46°
Cohesion	900 Pa

In the first step, a gravitational load is applied to the wheel hub and a 5kg mass

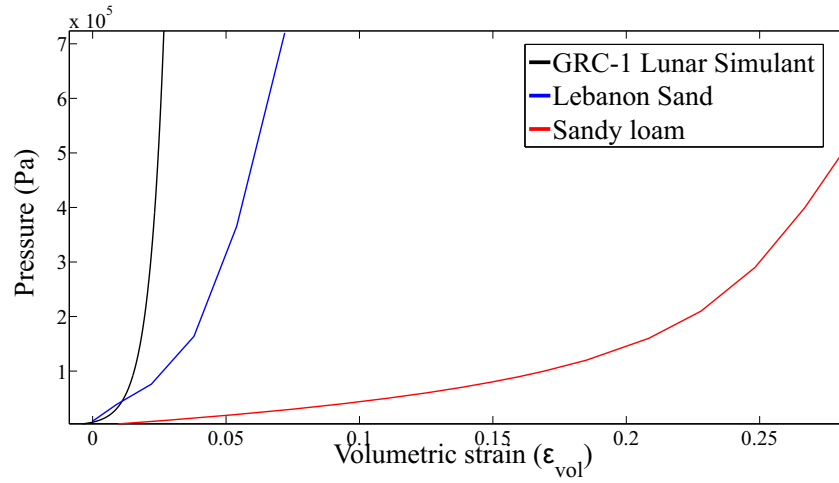


Figure 6.9: Pressure-Strain Relationship for common sandy soils and GRC-1 [85]

was added representing 1/10th the nominal load on the wheel. Once the wheel and soil reach a steady state, forward and rotational velocities are applied at the wheel centroid. A depiction of the FE model of the deformable soil case is illustrated in Figure 6.10. The legend shows the soil displacement in the z direction, or sinkage.

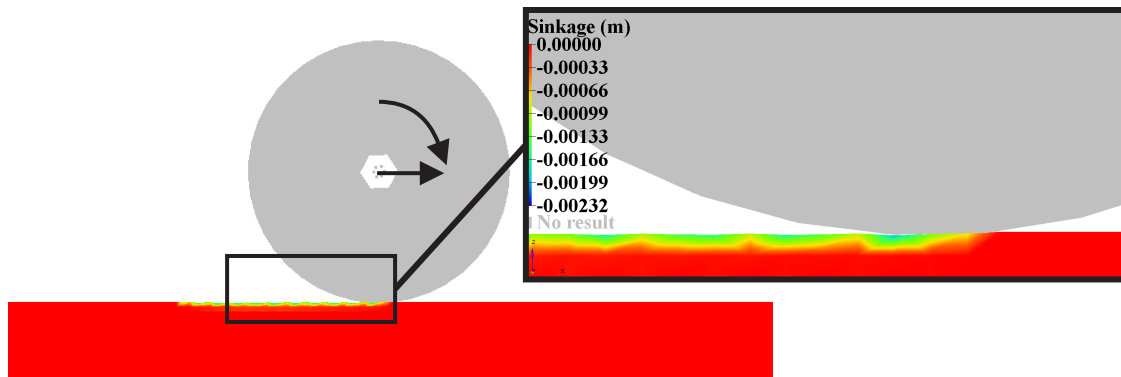


Figure 6.10: Soft soil FE results

Although the results differ considerably between the rigid and soft soil simulations, some results are compared in Table 6–13, including model size and total simulation

run time. In Table 6–13, wheel-ground contact lengths are compared since contact area will differ due to the variation in wheel width.

Table 6–13: Rigid vs. Soft Soil Results Comparison

Simulation	No. Elements	Time	L_w	σ_{VM}	θ_{tors}
Rigid ground	3270	3hrs	3.3cm	26.1kPa	0.05°
Soft Soil	11521	29.5hrs	6.6cm	3.0kPa	0.08°

The results in Table 6–13 illustrate a large discrepancy between the simulations. Although both wheels employed identical material properties, the soft soil doubles the contact length given the sinkage effects. Higher torsional displacement is seen as a result of increased motion resistance in the soft soil simulation. The maximum von Mises stress was an order of magnitude larger in the rigid ground case, caused by poor ground pressure distribution beneath the wheel. Finally, the computational time is an order of magnitude higher for the soft soil case, making the soft soil model computationally impractical for the MOO problem. In addition to the large computation time required, accurately simulating physical behaviour requires the soil parameters to be validated experimentally.

6.4 Discussion of Component Level Optimization

The component level analysis presents a multi-scale approach to determine optimal homogeneous orthotropic wheel material properties for multiple objectives, investigates the conflicting nature of material properties on wheel performance and finds feasible cellular material designs which attempt to match the optimal wheel

design. Separating the component level analysis into a macro and microscopic problem and employing a rigid ground assumption results in a computationally practical problem. An error analysis is conducted separately from the optimization framework to investigate the effectiveness of the multi-scale approach, as well as the sequential approach of the separate system and component level analyses.

In this work, the cellular materials investigated were limited to bending dominated with closed-form constitutive material models. This poses a limitation on the results presented here, as a search of alternative unit cells was not possible. Achieving the optimal homogeneous wheel properties is therefore limited with the unit cells investigated. Constraining the design variables in the MOO to feasible properties using cellular material constitutive models can circumvent the limitations of the solutions. Although the MOO would yield only feasible solutions, the computational efficiency of the optimization problem would be greatly reduced. Additionally, only one unit cell type can be investigated per simulation run.

Alternatively, the MOO results presented here can be employed to design an optimal cellular material which matches the desired properties. In [111], the objective was to create a material with an emphasis on achieving a specific shear modulus in 2D whereas this work demonstrated the importance of orthotropic material properties in 3D. Directional compliance of cellular materials was shown to be the most critical factor in achieving optimal wheel performance. Although some cellular materials attain desirable material properties, cell wall buckling and yield must be verified to ensure feasibility. As such, cellular materials with closed-form expression of effective material properties were selected. Investigating more complex unit cells requires the

use of numerical homogenization methods to relate macro and microscopic material properties.

Finally, the component level optimization problem presented here is limited to cellular wheel concepts. As discussed in Chapter 5, cellular materials can be tailored to specific material properties and therefore control wheel elastic behaviour. However, the component level optimization can be extended for alternative wheel concepts, provided their design can be parameterized into a set of component level wheel design variables. Preliminary work on the segmented wheel presented in Section 5.3.1 demonstrates the applicability of the MOO approach to alternative wheel concepts. The segmented or other wheel concepts can be modelled directly in a dynamic FE environment to evaluate the objective functions described in this chapter. The homogeneous wheel model would be unsuitable since infinite periodicity of the wheel internal structure cannot be assumed as was the case for cellular materials. Therefore, cellular material optimization and component-level error analysis steps would not be required. The verification step between the system-component level analyses, however, would still be needed to ensure system-level objectives are met. Applying this method to non-cellular wheel concept would serve to improve the performance of an existing wheel concept, whereas the homogeneous wheel approach presented here allows for more insight into the desirable mechanical properties of the wheel internal structure.

CHAPTER 7

Conclusions and Recommendations

The research objectives presented in Chapter 1 were satisfied through the development of a novel design framework for the multi-objective optimization of compliant lunar wheels. More specifically:

- i An exhaustive literature review of mobility performance measures for off-road, planetary and robotic vehicles has been conducted. In Chapter 4, a comprehensive list of mobility related performance metrics is presented. Broadly, these metrics can be classified by the following performance categories: trafficability, maneuverability, terrainability (quasi-static, dynamic), reliability and mission and environmental compatibility.
- ii The relationship between the aforementioned performance metrics and wheel design are identified in Chapter 4 through mathematical models describing: wheel-soil terramechanics, rover steering, rover-terrain dynamics and mission performance criteria. These models were selected from literature, and in some cases, modifications were presented to account for the relevant mission or rover cases.
- iii The critical system level wheel design variables are investigated through a parametric analysis of rover and mission performance metrics. Maximizing the diameter, width, lateral and torsional stiffness is generally preferred for improving trafficability, maneuverability and terrainability. Vertical stiffness causes

conflict, as an increased stiffness serves to improve traction while decreasing driving efficiency. Wheel damping, for high speed driving, is shown to be critical for absorbing vehicle-terrain induced vibrations. The optimal wheel system level design variables for a prospecting and excavating lunar mission scenario were also found. The mission objectives were shown to influence the value of the optimal wheel design variables. A change in vertical stiffness changes the prospecting mission mobility power and energy. The optimal vertical stiffness will depend on the scenario details, such as the travel, slope climbing or turning distances. For an excavation scenario where the rover must build a berm, the wheel diameter, width and vertical stiffness, were shown to be critical. Although maximizing traction will result in lower mission duration and driving distances, lowering the excavation capacity of the rover can lower driving power requirements. Driving power requirements influence both rover and mission architecture design. In both the excavation and prospecting cases, the wheel design was shown to play a crucial role in achieving mission objectives.

- iv As no preferred wheel design concept exists in literature, an investigation of wheel concepts was presented in Chapters 2 and 5. Reduced scale wheel prototypes were developed and qualitative testing was conducted on a polypropylene cellular wheel, two aluminum cellular wheels, a segmented wheel concept and the iRings wheel. The iRings wheel was further investigated experimentally, while both the segmented and cellular wheels were investigated numerically. In addition to exploring novel wheel concepts, selection criteria for wheels suitable for optimization were identified. These included: the parameterizability

of wheel structural designs, the scalability of the wheel design, the computational feasibility of the wheel concept and the design variable-objective space relationship. These criteria led to the selection of the cellular wheel concept as the preferred wheel for component level optimization in Chapter 6.

- v A component level analysis for the structural design of a specific wheel concept, where system level design variable dependence is considered, is presented in Chapter 6. This is achieved by developing two finite element simulation models of a wheel coupled with a multi-objective optimization (MOO) algorithm, namely the Non-dominated sorting genetic algorithm (NSGA-II). The MOO algorithm solves the Pareto frontier of wheel optimal structural designs.
- vi For verification, the aforementioned methodology is applied to the cellular wheel concept. To improve computational efficiency, several modifications are necessary. The ground is modelled as rigid and the cellular structure is modelled as a homogeneous orthotropic material to improve. Homogenization of the cellular material requires the addition of a secondary cellular material optimization step to determine optimal unit cell designs. The MOO results demonstrate the conflicting nature of objectives, and a set of six solutions of interest are selected from the Pareto frontier for further investigation. The cellular material optimization is conducted using material constitutive models for cubic, cuboctahedron and hexagonal unit cells. The assumptions are verified, and direct modelling of wheels with cubic unit cells is conducted. Ultimately, the limitations of the material models are shown; however the methodology is sound for the multi-objective optimization of compliant lunar wheel designs.

7.1 Contributions

The work presented here provides several contributions, namely:

- i A novel systematic approach to the design of compliant wheels for planetary exploration vehicles is proposed. The approach decomposes the problem into system and component level analyses and employs multi-objective optimization to optimize the structural wheel designs to achieve rover and mission objectives.
- ii A system level analysis for compliant wheels is presented which demonstrates the importance of elastic wheel design in mission and rover performance, and recommends wheel design variables for specific lunar missions and rover designs.
- iii Novel wheel concepts are presented and investigated through experimental and numerical techniques.
- iv A multi-objective optimization of a three dimensional wheel-terrain finite element analysis is formulated and solved, providing recommendations for homogeneous orthotropic wheel material properties.
- v A cellular material optimization problem is formulated and solved for several unit cell types for a cellular wheel. Insight into optimal unit cell designs for cellular wheels is provided.

7.2 Limitations of Current Methodology and Future Work

Decomposition of the wheel optimization problem succeeded in finding the optimal wheel material properties for a cellular wheel concept. However, by not limiting the structural multi-objective optimization to feasible cellular materials, a secondary step, namely the cellular material optimization of unit cell types, is required to find the final microstructural design of the wheel. The cellular wheels presented

here are limited by the constitutive material models. Therefore, the cellular material optimization results are unsuccessful at matching the optimal homogeneous material properties. The effectiveness of the proposed methodology, however, was demonstrated by simplifying the cellular material optimization problem to one material property of interest (i.e. shear stiffness for cubic case, and axial stiffness for cuboctahedron case). Future work should address more complex unit cell designs by including a numerical homogenization step in the cellular material optimization problem. Alternatively, a homogenization step can be included within the structural MOO problem, eliminating the need for a separate cellular material optimization. Topology optimization of a representative volume element of a periodic structure can also provide insight into the optimal unit cell design to achieve the prescribed material properties.

The current approach limits the quantitative analysis of the component level optimization due to the rigid ground assumption. In this work, the lateral, torsional and vertical wheel stiffness were used qualitatively to couple the component and system level analyses. Future work should address the deformable wheel-soil case, where rover performance metrics can be computed directly from the component level analysis. Computational efficiency of the model must be considered, however, if a finite element based compliant wheel-soft soil model is to be solved iteratively within the multi-objective optimization problem.

The component level analysis presented here is limited to cellular concepts. As discussed in Chapters 2 and 5, a wide range wheel concepts can provide promising preliminary designs. To apply the proposed methodology, alternative wheel concepts

must meet the criteria described in Chapter 5, namely: parameterizability, scalability, computational feasibility and a large objective function-design variable space. Preliminary static structural multi-objective optimization of a segmented wheel concept in Chapter 5 was promising, and future work can address applying the proposed methodology to this wheel concept.

The wheel design methodology presented in this thesis is limited to linear-static deformation models. Non-linearity can be introduced at the component level analysis through the FE model of the wheel, provided it can be modelled accurately. The iRings wheel is an example of a challenging wheel to model numerically. In this case, empirically based surrogate models relating iRings design variables to performance metrics are preferred. Non-linear cellular material behaviour such as elastic buckling can be achieved by employing polymeric materials in the wheel design concept. This can be especially useful for dynamic loading cases. Future work should address non-linear behaviour of cellular materials in the constitutive material models.

The gradient cellular MOO results presented in Section 6.1.3 were limited by the total number of function evaluations. To solve for a multi-layer cellular material wheel, parallelization of the optimization algorithm can be made to take advantage of multi-core processors to reduce overall simulation run time. Alternatively, non-evolutionary optimization algorithms which can solve large problems, such as the generalized pattern search method, can also be employed.

The error between system and component level analyses demonstrated the limitations of the proposed approach. As discussed in Section 6.3.2, the component level exceeds or fails to achieve the target by several orders of magnitude. This indicates

that system level targets may be unrealistic, and error analysis should be included within the optimization framework. This can be accomplished by adopting a multi-disciplinary optimization approach, where component and system level optimization problems are coupled and solved simultaneously. This would allow system-level targets to be adjusted during the optimization routine. Convergence between the system and component level solutions ensures that system targets are feasible. Such an approach is particularly relevant when the mission scenario, rover design and wheel concept are well developed and specific performance requirements are known.

7.3 Recommendations for Flight Rover Wheels

The work presented here demonstrates the importance of a systematic approach to wheel design. The wheel plays a critical role in rover performance and therefore planetary exploration mission success. Wheel design should be taken into account early in rover design phases, and future wheel development should consider a system level and multi-objective approach. Deformable soil models, novel unit cell topologies, non-linear material models and alternative wheel concepts will also serve to extend the proposed approach to tailor wheel structural design for specific rover and mission objectives.

APPENDIX A

Parametric Mission and Rover Mobility Performance Analysis

A parametric analysis on the effect of the system level wheel design variables on mobility performance is presented here. First, the importance of mobility performance metrics on mission scenario indices of performance is investigated, followed by the investigation on the wheel design on an inclusive set of mobility performance metrics. The elastic wheel pseudo-model and multi-disciplinary performance models described in Chapter 4 are used.

A.1 Mission Performance Analysis

This section presents a parametric analysis of rover mobility performance metrics (z_i) on mission performance metrics (f_j). Two missions are investigated in this section: a lunar resource prospecting and berm building scenario. The mission parameters $\mathbf{c}_{mission}$ are outlined in Table 4–4, while the lunar environmental parameters \mathbf{c}_{env} used in this analysis are shown in Table 4–5.

A.1.1 Prospecting Mission Scenario

The rover performance metrics z_i investigated in the prospecting scenario are the coefficients of steering (C_{st}) and rolling resistance (C_r), as shown in Table A–1. A nominal tractive effort coefficient (C_{DP}) was used to ensure that the rover can surmount 20° slopes without more than 20% wheel slip. The nominal values of the steering and rolling resistance were taken from the Juno II rover using rubber all-terrain vehicle pneumatic tires. It should also be noted that the nominal rolling

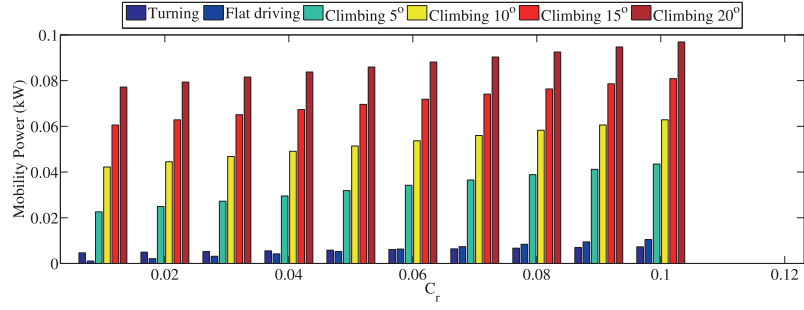
resistance nominal value is equivalent to climbing a 0.57° slope. According to [Peters ASTRO], the LRV wheels rolling resistance $C_r = 0.026$, or equivalent to climbing a 1.5° slope.

Table A–1: Prospecting Scenario Rover Parameters (\mathbf{C}_{rover})

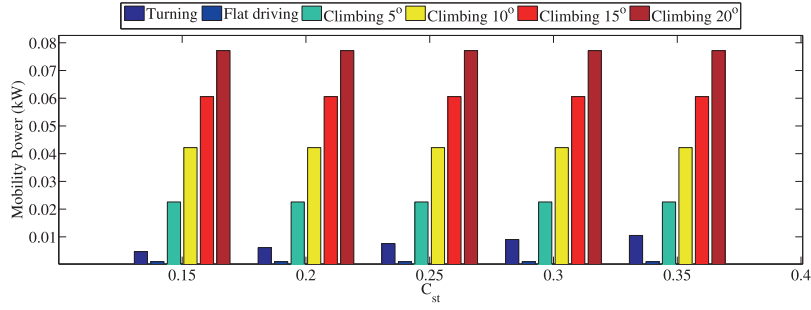
Rover Parameters	Nominal	Min	Max
Total Vehicle mass (kg) - m_{rover}	200	-	-
Longitudinal wheel spacing (m) - L_{rover}	2	-	-
Lateral wheel spacing (m) - b_{rover}	1	-	-
Operating speed (m/s) - v	0.6	-	-
Number of wheels - N	4	-	-
Steering Mechanisms	Skid	-	-
Coefficient of steering resistance (C_{st})	0.15	0.15	0.35
Coefficient of rolling resistance (C_r)	0.01	0.01	0.1
Tractive effort (C_t) @20% slip	0.53	-	-
Drawbar coefficient (C_{DP}) @20% slip	$0.53-C_r$	$0.53-C_{rmin}$	$0.53-C_{rmax}$

The prospecting mission metrics f_j of interest here are the energy and power consumption for the total mission duration (E_{total} , P_{total}) and each driving mode (E_{mode} , P_{mode}). The results of the parametric analysis are presented in Figure A.1.

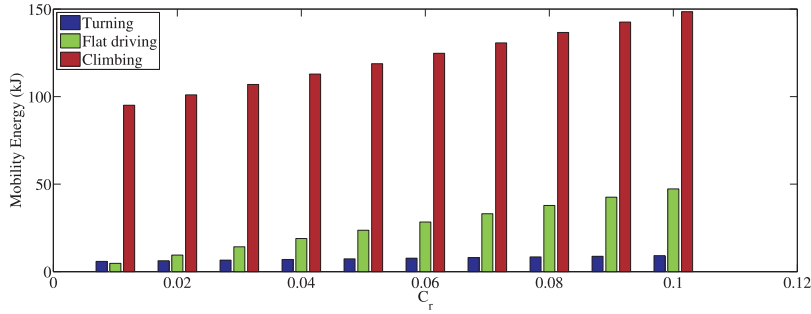
Increasing the resistance during rolling and steering directly causes an increase in the power and energy requirements during climbing, driving and turning. The high power and energy demand during slope climbing is evident, though it should be noted that in this analysis, a constant speed was used during all driving operations. Nonetheless, climbing 5° and 20° slopes require over 20 and 90 times more power than driving on level ground using the nominal rolling and steering resistance coefficients. A turning manoeuvre requires approximately 4 times more power than level driving at the nominal values. Increasing the nominal rolling resistance results



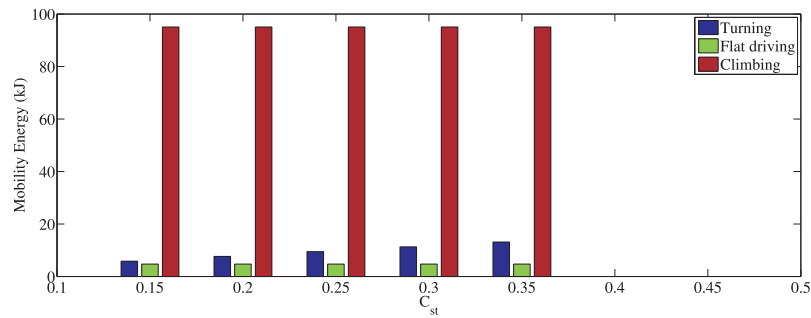
(a) P_{mode} vs. C_r



(b) P_{mode} vs. C_{st}



(c) E_{mode} vs. C_r



(d) E_{mode} vs. C_{st}

Figure A.1: Prospecting Mission Performance

in an increase of the driving power requirements. The increase is most significant in climbing and flat driving. Increasing steering resistance will affect only the power required during a turning manoeuvre, as seen in Figure A.1 (b). The power demands during steering increase from roughly x4 to over x10 times the flat driving power. Therefore, the turning manoeuvres conducted in a rover mission become important from both a mission planning and rover design perspective.

Similarly to power, the energy demands of climbing exceed those of level driving and turning. At $C_r = 0.01$ and $C_{st} = 0.15$, the energy of steering is 20% higher than flat driving even though it constitutes only 750m of the total 5km traverse. For $C_r > 0.1$, however, driving energy demand is higher than turning energy. Steering resistance, as was discussed previously, only affects the requirements on turning. However as illustrated in Figure A.1(d), the energy demand increases from x1.2 to x2.7 over the level driving energy demands. This is worth noting since turning manoeuvres constitute only 15% of the total mission.

Finally, the total energy E_{total} consumed as a function of the two rover performance metrics, C_r and C_{st} , is shown in Figure A.2. Energy and the coefficients are normalized to visualize the importance of the two metrics given the prospecting scenario outlined above. Although both C_r and C_{st} increase mobility energy linearly, rolling resistance is more critical.

The prospecting mission scenario demonstrated that:

- i Minimizing C_r and C_{st} will reduce power and therefore energy consumed during the mission.

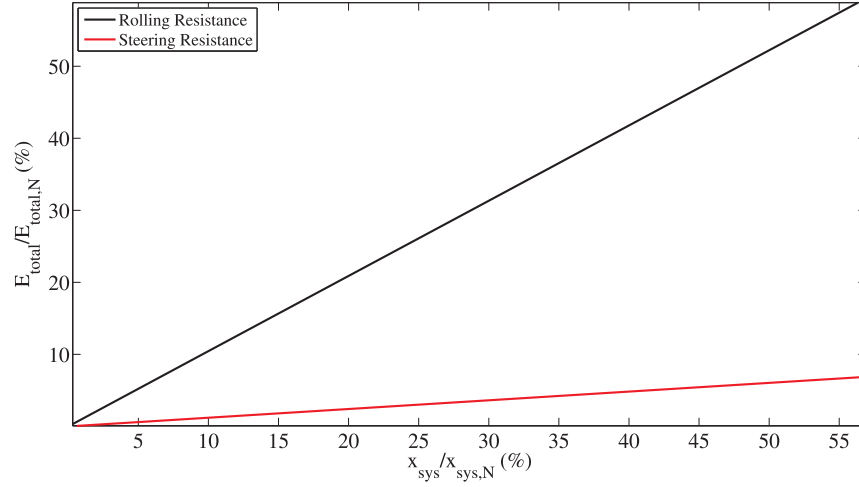


Figure A.2: Prospecting scenario energy

- ii The relative importance of C_r and C_{st} is dependent on mission operations and path planning.
- iii Skid-steer is highly inefficient and careful consideration of C_r , C_{st} and path planning is required if this steering mode is employed by the rover.
- iv The tractive effort limits the maximum slope climbing ability of the rover but is otherwise less important than C_r and C_{st} for prospecting type missions.

A.1.2 Excavating Mission Scenario

The rover parameters $\mathbf{C}_{\text{rover}}$ used in this analysis listed in Table A-2. The tool size was designed to fit the rover, whereas the properties were obtained from [118]. A parametric investigation of the role of the coefficient of rolling resistance (C_r), steering resistance (C_{st}) and tractive effort (C_t) on mission performance is presented here. Two additional rover parameters were played a key role in this investigation, notably: available payload mass (m_{payload}) and tool digging depth (d_T). The tool

depth was fixed and the available payload mass was found from Equations (4.17) and (4.48) describing the available drawbar pull and excavation forces respectively. A more accurate depiction of the available payload mass must consider available motor torque.

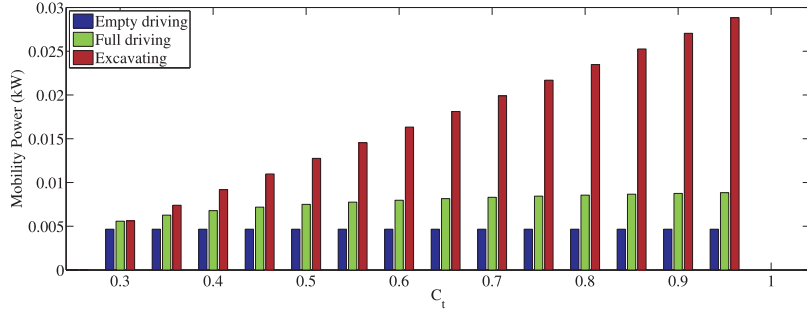
The excavation task is divided into three main driving modes: driving to the excavation site without a payload, excavating regolith using the scoop and transporting the regolith to the berm site. The scenario parameters, listed in Table 4–4, assume a distance of 50m between the excavation site and the berm site. 10% of the driving distance consists of skid-steer turn manoeuvres, both for the empty and full rover. As such, the mission metrics of interest for the berm building scenario f_j are the total driving distance ($L_{mission}$), mission duration ($t_{mission}$), total and modal mobility power (P_{total} , P_{mode}) and energy consumption (E_{total} , E_{mode}) for each driving mode. Unlike the prospecting mission, the total excavation driving time is not specified and therefore dependent on rover performance metrics (z_i).

With a fixed tool depth, the upper bound of the maximum payload mass is determined by the the available drawbar pull. Therefore, both excavation and full driving are directly affected by C_t . According to Figure A.3(a), an increase of C_t from 0.25 to 0.95 yields close to 6 and 1.6 times P_{full} and P_{ex} . C_t does not affect empty driving, since only motion resistance is considered. For $C_t < 0.3$, the available drawbar pull is insufficient for excavating at a depth of 8.0cm. At $C_t=0.95$, the payload mass corresponds to 178.7kg or 90% of the empty mass of the vehicle.

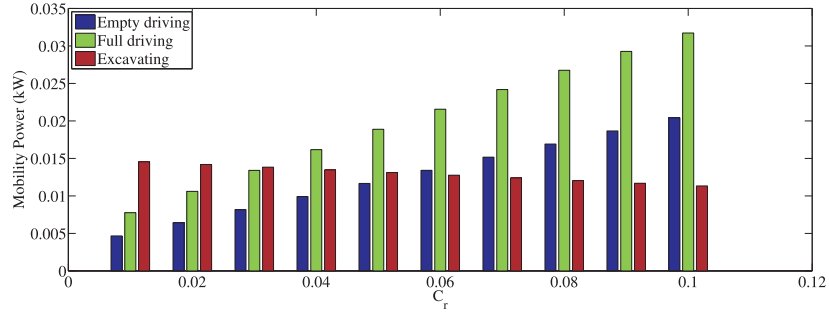
Increasing the C_r by 10 times, while C_t and C_{st} remain constant, yields an increase

Table A-2: Excavating Rover Parameters (C_{rover})

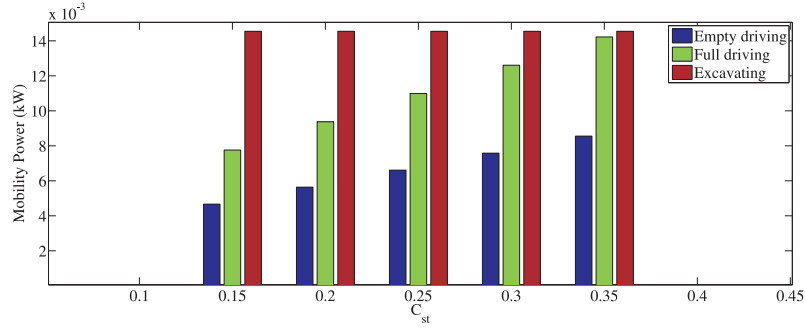
Rover Parameters	Nominal	Min	Max
Total vehicle mass (kg) - m_{rover}	200	-	-
Payload mass (kg) - $m_{payload}$	<i>calculated</i>	<i>calculated</i>	<i>calculated</i>
Longitudinal wheel spacing (m) - L_{rover}	2	-	-
Lateral wheel spacing (m) - b_{rover}	1	-	-
Operating speed (m/s) - v	0.6	-	-
Excavation speed (m/s) - v_{ex}	0.1	-	-
Number of wheels - N	4	-	-
Steering mechanism	Skid	-	-
Scoop width (m) - b_T	1.5	-	-
Digging depth (m) - d_T	0.08	-	-
Soil-tool adhesion coefficient (Pa) - C_a	1930	-	-
Surcharge mass - q	1	-	-
Rake angle - β	45°	-	-
External friction angle - δ	10°	-	-
Shear plane failure angle - ρ	30°	-	-
Coefficient of steering resistance - C_{st}	0.15	0.15	0.35
Coefficient of rolling resistance - C_r	0.01	0.01	0.1
Tractive effort - C_t @20% slip	0.55	0.25	0.95
Drawbar coefficient - C_{DP} @20% slip	$0.55 - C_r$	$C_{T,min} - C_{r,min}$	$C_{T,max} - C_{r,max}$



(a) P_{mode} vs. C_t

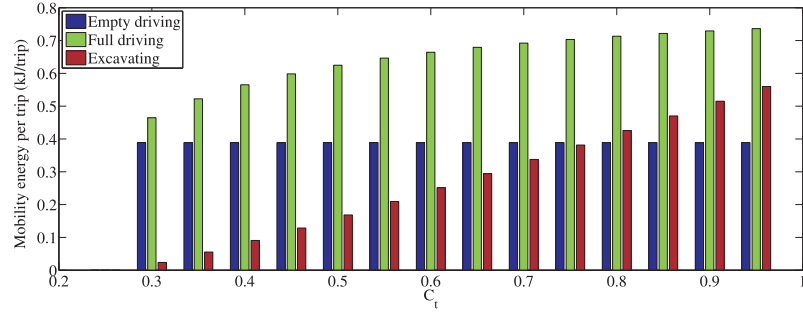


(b) P_{mode} vs. C_r

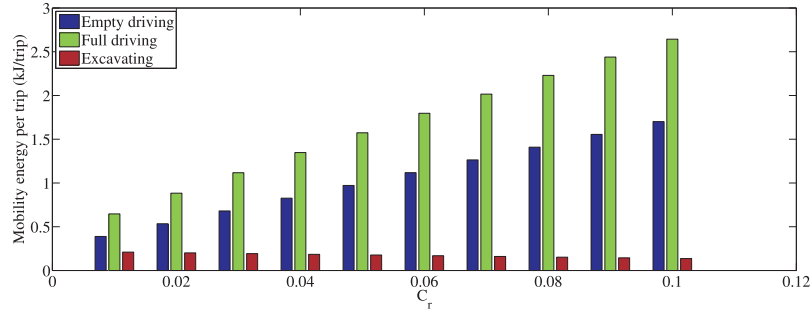


(c) P_{mode} vs. C_{st}

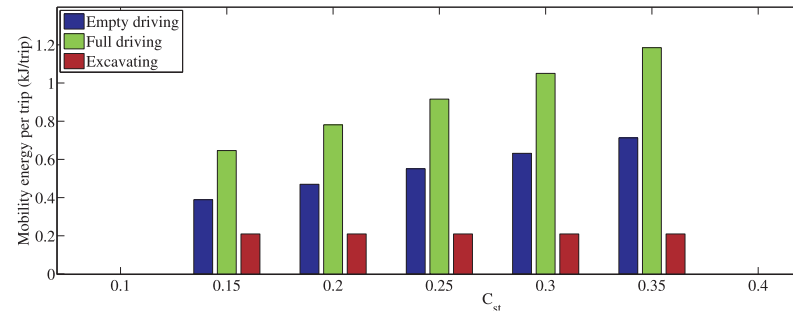
Figure A.3: Berm Building Power Mission Performance



(a) E_{mode} vs. C_t



(b) E_{mode} vs. C_r



(c) E_{mode} vs. C_{st}

Figure A.4: Berm Building Energy Mission Performance

of 4.3 times P_{empty} and P_{full} as shown in Figure A.3(b). P_{ex} per trip decreases for an increase in C_r , since the available drawbar pull decrease results in less excavating per trip. C_{st} will only effect the empty and full driving cases, as the rover will not conduct turning manoeuvres during excavation. However, C_{st} is less important for the excavation scenario than the prospecting scenarion presented previously, as an increase in C_{st} by 2.3 times results in approximately a 1.8 times increase in mobility power demand, as seen in Figure A.3(c).

The amount of regolith to transport and the distance between the excavation and berm site are fixed in the mission investigated here. However, the amount of regolith transported per trip, and therefore the number of trips, is determined by the available drawbar pull. As illustrated in Figure A.4(d), an increase in the C_t directly increases E_{full} and E_{ex} per trip. At $C_t = 0.25$, E_{full} is almost 20 times higher than P_{ex} ; whereas at $C_T = 0.95$, it is only 1.6 times. This is caused by the increase in excavation distance per trip to fill the heavier regolith payload. Beyond $C_t = 0.7$, E_{ex} per trip is greater than the E_{empty} empty driving energy required for the 50m traverse. It should be noted that the per trip energy is compared here, as infrastructure for recharging the rover between trips is assumed. C_r simultaneously increases E_{full} and E_{empty} by over 4 times per trip. E_{ex} is lowered, as discussed previously, due to a decrease in available drawbar pull, resulting in a lowering of excavated regolith payload per trip. At $C_r = 0.01$ the rover can excavate and transport an additional 21.7kg per trip than at $C_r = 0.1$.

The mobility related energy requirements per trip are important, however, as the objective of this excavation scenario is to move regolith to build a berm, the total

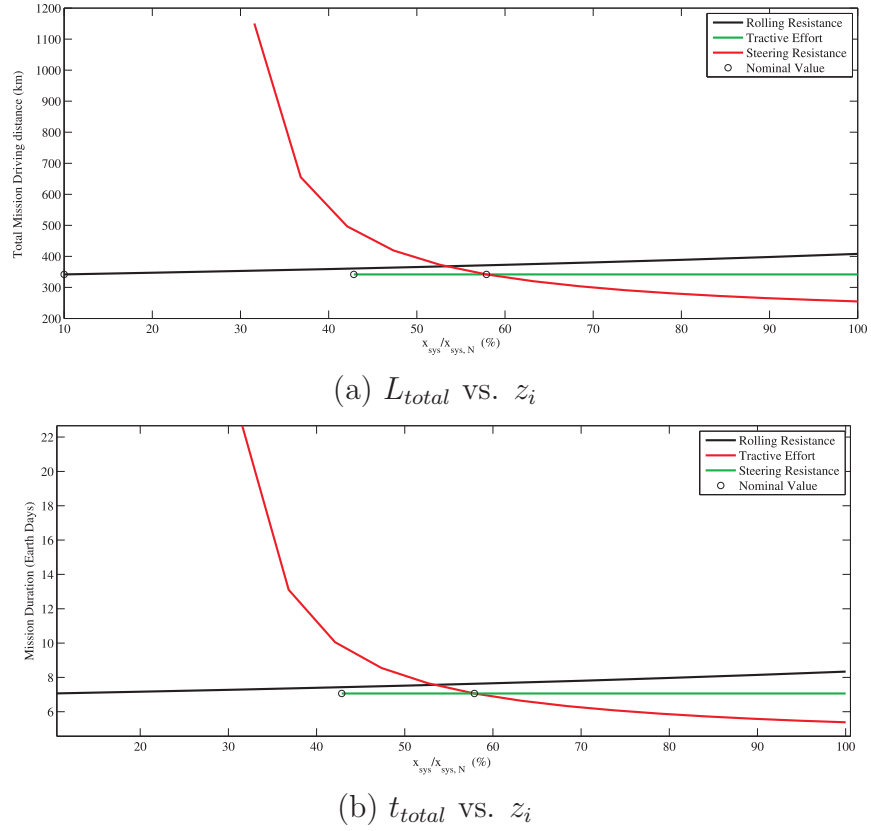


Figure A.5: Berm Building Mission Performance

mission duration and distance travelled are also germane. L_{total} , governed by the number of trips required to build the berm is therefore important in this analysis. Figure A.5(a) and (b) illustrate the relative importance of z_i on total mission driving distance and time, respectively. The coefficients are normalized to their maximum value listed in Table 4–4, and the nominal case is identified by a circular marker.

Nominally, the rover must drive a total of 342km to build the berm. The role of the tractive effort is evident. At the minimum and maximum values of C_t , 0.03 (since

0.025 has insufficient traction for digging at a depth of 0.08m) and 0.95 respectively, the total driving distance varies from 1150km to 255km. The increase in C_r causes an increase from 342km to 408km, whereas steering resistance does not influence the total distance travelled.

Mission duration is computed in earth days in Figure A.5(b) and consists of the distance divided by speed of the rover for each driving mode. C_t once again plays the most significant role in mission duration ranging from 22.6 to 5.4 days. C_r causes an increase in mission duration from 7 to 8.3 days. C_{st} has no affect in this analysis.

Although an accurate assessment on rover mobility performance metrics cannot be made without a more detailed mission scenario or rover design, it is clear that:

- i Increasing C_T allows the rover to excavate and transport more regolith thereby reducing total mission time and duration. However, this causes an increase in the excavation requirements on power and energy.
- ii Reducing C_r improves the drawbar pull allowing more regolith to be excavated and transported. Additionally, it reduces the requirements on power and energy during empty and full driving.
- iii Reducing C_{ST} reduces the power and energy demands on the rover mobility system during empty and full driving. Although this plays no role in total mission drive distance, it can contribute to lowering mission time if the rover must recharge less frequently.

A.2 Rover Performance Analysis

This section investigates the effect of the wheel system variables \mathbf{x}_{sys} on rover mobility performance metrics z_i . The parametric analysis on rover trafficability and

manoeuvrability metrics is presented in Section A.2.1, while Section A.2.2 presents the rover dynamic terrainability parametric analysis.

A.2.1 Rover Trafficability and Manoeuvrability Analysis

Table A–3 describes the nominal and range of the design variables and environmental parameters used in the analysis, and Figure A.2.1 illustrates the results.

Table A–3: Trafficability and Manoeuvrability Analysis Parameters (\mathbf{x}_{sys} and \mathbf{c}_{rover})

Parameters	Nominal	Min	Max
Vehicle mass (kg) - m	200	-	-
Vehicle length (m) - L_{rover}	2	-	-
Vehicle width (m) - b_{rover}	1	-	-
Forward speed (km/hr) - v	5	-	-
Wheel slip (%) - s	20	-	-
Number of wheels - N	4	-	-
Wheel Coefficient of lateral resistance - μ_s	0.55	-	-
Wheel Hub diameter (m) - D_h	0.3	-	-
Wheel Diameter (m) - D_w	0.7	0.05	1.2
Wheel Width (m) - b_w	0.4	0.01	1.0
Wheel Vertical stiffness (kN/m) - K_V	5	1	10
Wheel Lateral stiffness (kN/m) - K_L	15	0.5	5
Wheel Torsional stiffness (kNm/rad) - K_T	5	0.5	5

Increasing b_w and D_w both reduce C_r until a minimum is achieved, while an increase of K_V negatively affects C_r as seen in Figure A.2.1(a). This is caused by the increase in wheel sinkage due to the smaller contact area of a stiffer wheel. Neither K_T nor K_L plays any role in rolling resistance. The drawbar pull coefficient C_{DP} , similarly to C_r , is negatively affected by an increase in K_V as shown in Figure A.2.1(b). An

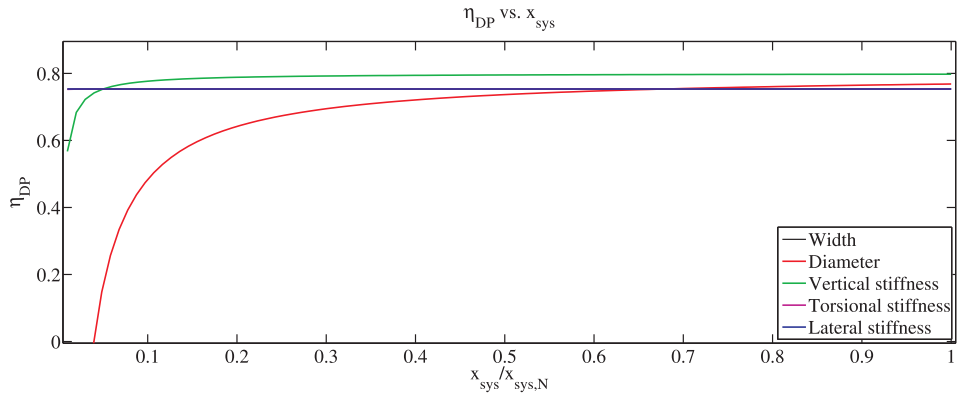
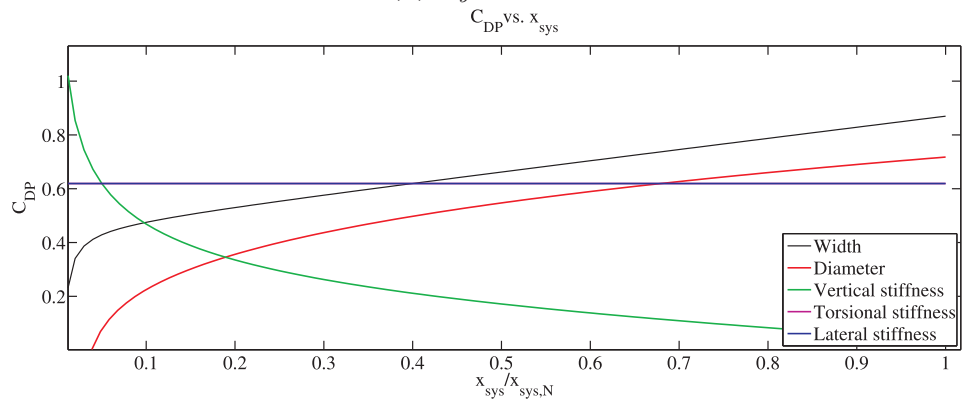
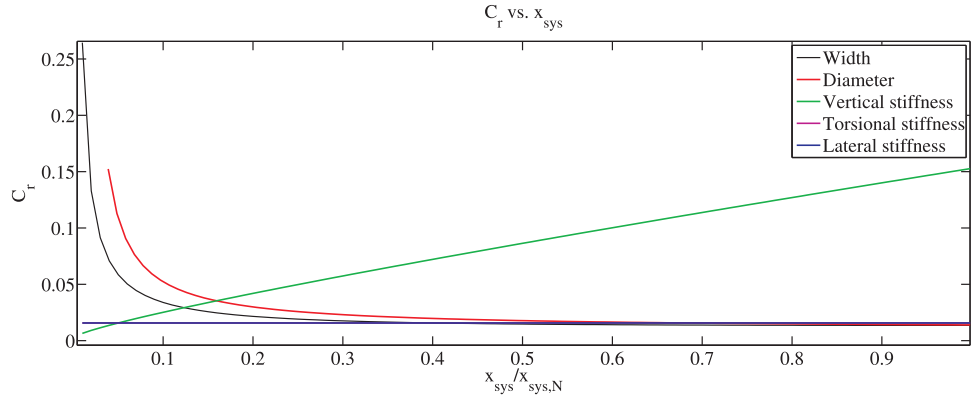


Figure A.6: Trafficability Performance Analysis

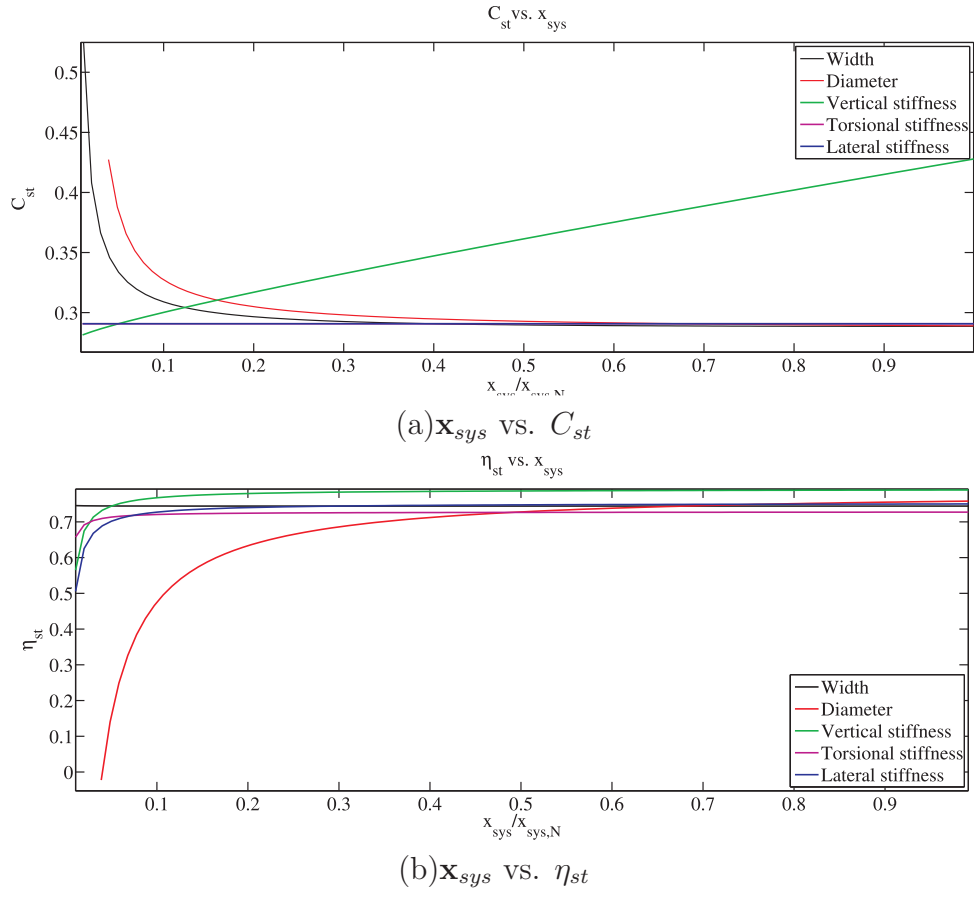


Figure A.7: Maneuverability Performance Analysis

increase in b_w and D_w both increase the C_{DP} , while K_T and K_L do not play a role. Tractive efficiency η_{DP} is increased with D_w , as shown in Figure A.2.1(c). An increase in K_V , unlike with C_r and C_{DP} , positively affects η_{DP} . Increasing the K_T and b_w does positively affect η_{DP} ; however it is hardly distinguishable in Figure A.2.1(c). Nonetheless, increasing K_T serves to reduce energy loss as shown in Equation (4.22). Like C_r , the steering resistance C_{st} is reduced by an increase in b_w and D_w and a reduction of K_V . It should be noted, however, that μ_s will be a function of wheel material, K_L , sinkage, and wheel shape. From Equation (4.27), however, it is known that a reduction in μ_s leads to a reduction of steering resistance and this should be considered when selecting wheel configurations. Steering efficiency η_{st} increases with an increase in K_V , K_T and K_L , as well as an increase in D_w . b_w , on the other hand, plays a minor role as seen in Figure A.2.1(e).

The findings of the trafficability and maneuverability analysis can be summarized as follows:

- i *Wheel diameter*: the size of the wheel is the most important parameter in vehicle trafficability in soft soil. Larger diameter wheels provide a longer contact length, contributing to higher drawbar pull; however the diameter of the wheel is typically limited by vehicle size. Additionally, larger diameter wheels require higher torque, thereby increasing the mobility power requirements.
- ii *Wheel width*: a greater width provides a larger contact area, which increases available thrust. However, it also increases bulldozing resistance, which can reduce overall drawbar pull performance.

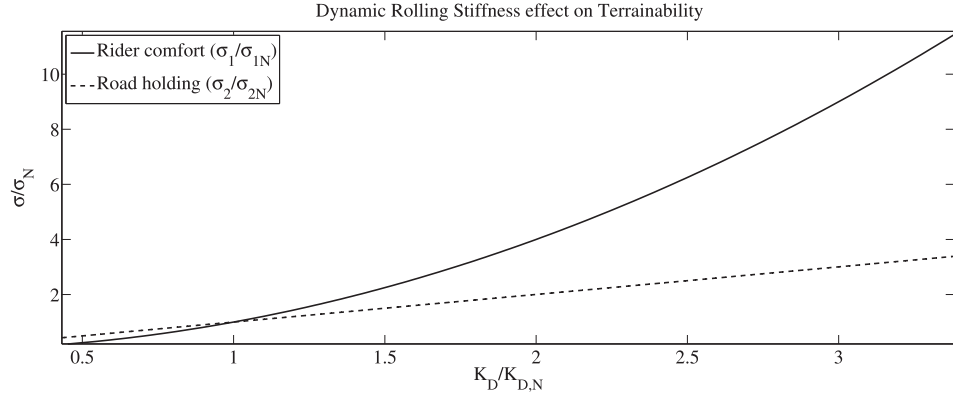
- iii *Wheel vertical stiffness*: a low stiffness improves contact area and therefore traction; but also contributes to reducing rolling and turning efficiency. The vertical stiffness proves to be conflicting with several performance objectives of the rover.
- iv *Wheel lateral stiffness*: Deflection in the lateral direction while undergoing a turning maneuver, especially one which involves skid-steering, can significantly reduce the turning efficiency.
- v *Wheel torsional stiffness*: Much like lateral stiffness, a low torsional stiffness serves only to reduce tractive efficiency. However, given the relationship between torsional and vertical stiffness, this parameter is rarely independent from the other stiffness parameters in explicit wheel concepts.

A.2.2 Rover Dynamic Terrainability Analysis

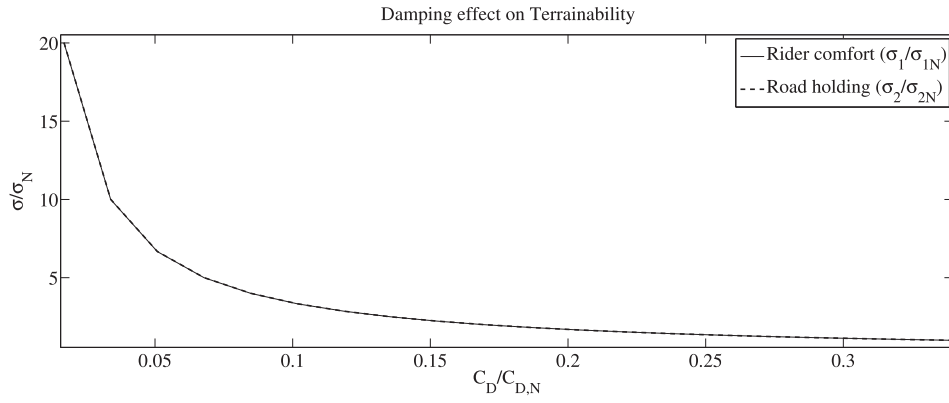
A parametric analysis using the parameters in Table A–4 was complete to verify the wheel parameters which affect the dynamic response of the rover to terrain induced vibrations. It should be noted that the appropriate wheel stiffness used in the analysis is the dynamic rolling stiffness K_D and can be up to 26% lower than the static wheel stiffness K_V [119].

Table A–4: Dynamic Terrainability Parameters (\mathbf{x}_{sys} and \mathbf{C}_{rover})

Parameters	Nominal	Min	Max
Quarter vehicle mass (kg) - m_w	50	-	-
Speed (km/hr) - v	5	-	-
Surface roughness constant ($m^2/cycles/m$) - G_0	$7e^{-5}$	-	-
Dynamic Vertical stiffness (kN/m) - K_D	5	1	20
Dynamic damping coefficient (kNs/m) - C_D	1	0.5	2



(a) K_D vs. σ_1 and σ_2



(b) C_D vs. σ_1 and σ_2

Figure A.8: Dynamic Terrainability Performance Analysis

Each parameter was varied to verify the change in response of the system with respect to the reference value. The non-dimensional performance values for rider comfort ($\frac{\sigma_1}{\sigma_{1,N}}$) and road holding ($\frac{\sigma_2}{\sigma_{2,N}}$) are plotted against non-dimensional stiffness ($K_D/K_{D,N}$) and damping coefficient ($C_D/C_{D,N}$) in Figure A.8(a) and (b) respectively. From Figures A.8(a) and (b) it can be seen that:

- i Decreasing stiffness improves both rider comfort and road handling;
- ii Increasing damping improves both rider comfort and road handling;

Furthermore, speed and roughness cancel out in the computation of the dimensionless performance metric. This signifies that although speed and surface roughness do affect the response of the system, their magnitude does not change the wheel design variable direction of improvement on dynamic terrainability performance.

APPENDIX B

Closed-form Material Constitutive Models

The closed-form expressions for the constitutive material models for a cubic, body centered cubic, face centered cubic and cuboctahedron unit cells are presented in this Appendix. Additionally, the closed-form expression for yield and buckling of hexagonal unit cells is also provided.

B.1 2D Hexagonal Unit Cell Properties

The closed-form expression for buckling ($\sigma_{buckling}$) and yield stress ($\sigma_{yield,cell}$) of the hexagonal unit cell walls, as a function of base material elastic modulus E_s and yield stress $\sigma_{yield,base}$, can be found in [45] as:

$$\frac{\sigma_{buckling}}{E_s} = \frac{n^2 \pi^2}{24} \frac{t^3}{lh^2} \frac{1}{\cos \theta}$$

$$\frac{\sigma_{yield,cell}}{\sigma_{yield,base}} = \frac{t^2}{l} \frac{1}{2(h/l + \sin \theta) \sin \theta}$$

B.2 Cubic Unit Cell Properties

The closed-form expression describing the effective stiffness matrix K_{cubic} of a cellular material composed of periodic cubic unit cells is found as a function of unit cell design variables and base material elastic modulus E_s in [114] as:

$$K_{cubic} = \begin{pmatrix} \frac{AE_s}{L^2} & 0 & 0 & 0 & 0 & 0 \\ 0 & \frac{AE_s}{L^2} & 0 & 0 & 0 & 0 \\ 0 & 0 & \frac{AE_s}{L^2} & 0 & 0 & 0 \\ 0 & 0 & 0 & \frac{6EsI_{yy}}{L^4} & 0 & 0 \\ 0 & 0 & 0 & 0 & \frac{6EsI_{yy}}{L^4} & 0 \\ 0 & 0 & 0 & 0 & 0 & \frac{6EsI_{yy}}{L^4} \end{pmatrix}$$

The closed-form expression describing the internal forces $F_{b,cubic}$ in the struts of the cubic unit cell is found as a function of unit cell design variables and macroscopic strain vector $\epsilon_{i,j}$ acting on the homogeneous effective material in [114] as:

$$F_{b,cubic} = \begin{pmatrix} L^2\epsilon_{22} & L^2\epsilon_{12} & L^2\epsilon_{23} & 0 & \frac{L^3\epsilon_{23}}{2} & -\frac{L^3\epsilon_{12}}{2} \\ L^2\epsilon_{11} & -L^2\epsilon_{12} & -L^2\epsilon_{31} & 0 & -\frac{L^3\epsilon_{31}}{2} & \frac{L^3\epsilon_{12}}{2} \\ L^2\epsilon_{22} & L^2\epsilon_{12} & -L^2\epsilon_{23} & 0 & -\frac{L^3\epsilon_{23}}{2} & -\frac{L^3\epsilon_{12}}{2} \\ L^2\epsilon_{11} & -L^2\epsilon_{12} & L^2\epsilon_{31} & 0 & \frac{L^3\epsilon_{31}}{2} & \frac{L^3\epsilon_{12}}{2} \\ L^2\epsilon_{11} & -L^2\epsilon_{12} & -L^2\epsilon_{31} & 0 & -\frac{L^3\epsilon_{31}}{2} & \frac{L^3\epsilon_{12}}{2} \\ L^2\epsilon_{22} & L^2\epsilon_{12} & -L^2\epsilon_{23} & 0 & -\frac{L^3\epsilon_{23}}{2} & -\frac{L^3\epsilon_{12}}{2} \\ L^2\epsilon_{11} & -L^2\epsilon_{12} & L^2\epsilon_{31} & 0 & \frac{L^3\epsilon_{31}}{2} & \frac{L^3\epsilon_{12}}{2} \\ L^2\epsilon_{22} & L^2\epsilon_{12} & L^2\epsilon_{23} & 0 & \frac{L^3\epsilon_{23}}{2} & -\frac{L^3\epsilon_{12}}{2} \\ L^2\epsilon_{33} & L^2\epsilon_{31} & L^2\epsilon_{23} & 0 & \frac{L^3\epsilon_{23}}{2} & -\frac{L^3\epsilon_{31}}{2} \\ L^2\epsilon_{33} & L^2\epsilon_{31} & L^2\epsilon_{23} & 0 & \frac{L^3\epsilon_{23}}{2} & -\frac{L^3\epsilon_{31}}{2} \\ L^2\epsilon_{33} & L^2\epsilon_{31} & L^2\epsilon_{23} & 0 & \frac{L^3\epsilon_{23}}{2} & -\frac{L^3\epsilon_{31}}{2} \\ L^2\epsilon_{33} & L^2\epsilon_{31} & L^2\epsilon_{23} & 0 & \frac{L^3\epsilon_{23}}{2} & -\frac{L^3\epsilon_{31}}{2} \end{pmatrix}$$

B.3 Body Centred Cube Unit Cell Properties

The closed-form expression describing the effective stiffness matrix K_{BCC} of a cellular material composed of periodic body centred cubic unit cells is found as a function of unit cell design variables and base material elastic modulus E_s in [114] as:

$$K_{BCC} = \begin{pmatrix} K_{11,BCC} & K_{12,BCC} & K_{13,BCC} & 0 & 0 & 0 \\ K_{21,BCC} & K_{22,BCC} & K_{23,BCC} & 0 & 0 & 0 \\ K_{31,BCC} & K_{32,BCC} & K_{33,BCC} & 0 & 0 & 0 \\ 0 & 0 & 0 & K_{44,BCC} & 0 & 0 \\ 0 & 0 & 0 & 0 & K_{55,BCC} & 0 \\ 0 & 0 & 0 & 0 & 0 & K_{66,BCC} \end{pmatrix}$$

where

$$\begin{aligned}
K_{11,BCC} &= \frac{\text{Es}((9+4\sqrt{3})AL^2+128\sqrt{3}\text{Iyy})}{9L^4} \\
K_{12,BCC} &= K_{21,BCC} = \frac{4\text{Es}(AL^2-16\text{Iyy})}{3\sqrt{3}L^4} \\
K_{13,BCC} &= K_{31,BCC} = \frac{4\text{Es}(AL^2-16\text{Iyy})}{3\sqrt{3}L^4} \\
K_{22,BCC} &= \frac{\text{Es}((9+4\sqrt{3})AL^2+128\sqrt{3}\text{Iyy})}{9L^4} \\
K_{23,BCC} &= K_{32,BCC} = \frac{4\text{Es}(AL^2-16\text{Iyy})}{3\sqrt{3}L^4} \\
K_{33,BCC} &= \frac{\text{Es}((9+4\sqrt{3})AL^2+128\sqrt{3}\text{Iyy})}{9L^4} \\
K_{44,BCC} &= \frac{2\text{Es}(2\sqrt{3}AL^2+(27+16\sqrt{3})\text{Iyy})}{9L^4} \\
K_{55,BCC} &= \frac{2\text{Es}(2\sqrt{3}AL^2+(27+16\sqrt{3})\text{Iyy})}{9L^4} \\
K_{66,BCC} &= \frac{2\text{Es}(2\sqrt{3}AL^2+(27+16\sqrt{3})\text{Iyy})}{9L^4}
\end{aligned}$$

B.4 Face Centred Cube Unit Cell Properties

The closed-form expression describing the effective stiffness matrix K_{FCC} of a cellular material composed of periodic face centred cubic unit cells is found as a function of unit cell design variables and base material elastic modulus E_s in [114] as:

$$K_{FCC} = \begin{pmatrix} K_{11,FCC} & K_{12,FCC} & K_{13,FCC} & 0 & 0 & 0 \\ K_{21,FCC} & K_{22,FCC} & K_{23,FCC} & 0 & 0 & 0 \\ K_{31,FCC} & K_{32,FCC} & K_{33,FCC} & 0 & 0 & 0 \\ 0 & 0 & 0 & K_{44,FCC} & 0 & 0 \\ 0 & 0 & 0 & 0 & K_{55,FCC} & 0 \\ 0 & 0 & 0 & 0 & 0 & K_{66,FCC} \end{pmatrix}$$

where

$$\begin{aligned}
K_{11,FCC} &= \frac{\text{Es}((1+\sqrt{2})AL^2+24\sqrt{2}\text{Iyy})}{L^4} \\
K_{12,FCC} &= K_{21,FCC} = \frac{\text{Es}(AL^2-24\text{Iyy})}{\sqrt{2}L^4} \\
K_{13,FCC} &= K_{31,FCC} = \frac{\text{Es}(AL^2-24\text{Iyy})}{\sqrt{2}L^4}
\end{aligned}$$

$$\begin{aligned}
K_{22,FCC} &= \frac{\text{Es}\left(\left(1+\sqrt{2}\right)AL^2+24\sqrt{2}\text{Iyy}\right)}{L^4} \\
K_{23,FCC} &= K_{32,FCC} = \frac{\text{Es}\left(AL^2-24\text{Iyy}\right)}{\sqrt{2}L^4} \\
K_{33,FCC} &= \frac{\text{Es}\left(\left(1+\sqrt{2}\right)AL^2+24\sqrt{2}\text{Iyy}\right)}{L^4} \\
K_{44,FCC} &= \frac{\text{Es}\left(\sqrt{2}A(4\nu+5)L^2+12\text{Iyy}\left(2\left(2+\sqrt{2}\right)\nu+4\sqrt{2}+5\right)\right)}{2L^4(4\nu+5)} \\
K_{55,FCC} &= \frac{\text{Es}\left(\sqrt{2}A(4\nu+5)L^2+12\text{Iyy}\left(2\left(2+\sqrt{2}\right)\nu+4\sqrt{2}+5\right)\right)}{2L^4(4\nu+5)} \\
K_{66,FCC} &= \frac{\text{Es}\left(\sqrt{2}A(4\nu+5)L^2+12\text{Iyy}\left(2\left(2+\sqrt{2}\right)\nu+4\sqrt{2}+5\right)\right)}{2L^4(4\nu+5)}
\end{aligned}$$

B.5 Cuboctahedron Unit Cell Properties

The closed-form expression describing the effective stiffness matrix K_{cuboc} of a cellular material composed of periodic cuboctahedron unit cells is found as a function of unit cell design variables and base material elastic modulus E_s in [114] as:

$$K_{cuboc} = \begin{pmatrix} \frac{Es(AL^2 + 12I_{yy})}{\sqrt{2}L^4} & \frac{Es(AL^2 - 12I_{yy})}{2\sqrt{2}L^4} & \frac{Es(AL^2 - 12I_{yy})}{2\sqrt{2}L^4} & 0 & 0 & 0 \\ \frac{Es(AL^2 - 12I_{yy})}{2\sqrt{2}L^4} & \frac{Es(AL^2 + 12I_{yy})}{\sqrt{2}L^4} & \frac{Es(AL^2 - 12I_{yy})}{\sqrt{2}L^4} & 0 & 0 & 0 \\ \frac{Es(AL^2 - 12I_{yy})}{2\sqrt{2}L^4} & \frac{Es(AL^2 - 12I_{yy})}{\sqrt{2}L^4} & \frac{Es(AL^2 + 12I_{yy})}{\sqrt{2}L^4} & 0 & 0 & 0 \\ 0 & 0 & 0 & \frac{Es(A(8\nu+9)L^2 + 12I_{yy}(5\nu+6))}{2\sqrt{2}L^4(8\nu+9)} & 0 & 0 \\ 0 & 0 & 0 & 0 & \frac{Es(A(8\nu+9)L^2 + 12I_{yy}(5\nu+6))}{2\sqrt{2}L^4(8\nu+9)} & 0 \\ 0 & 0 & 0 & 0 & 0 & \frac{Es(A(8\nu+9)L^2 + 12I_{yy}(5\nu+6))}{2\sqrt{2}L^4(8\nu+9)} \end{pmatrix}$$

The closed-form expression describing the internal forces $F_{b,cuboc}$ in the struts of the cuboctahedron unit cell is found as a function of unit cell design variables and macroscopic strain vector $\epsilon_{i,j}$ acting on the homogeneous effective material in [114] as:

$$F_{b,cuboctahedron} = \begin{pmatrix} F_{x,b} & F_{y,b} & F_{z,b} & M_{x,b} & M_{y,b} & M_{z,b} \end{pmatrix}$$

where

$$F_{x,b} = \left(\begin{array}{l} \frac{L^2(-A^2(\epsilon_{11}-e_{22}-2e_{23}-\epsilon_{33})(8\nu+9)L^4 + 12AIyy(48\nu e_{23}+54e_{23}+15\epsilon_{33}+13\epsilon_{33}\nu+3\epsilon_{11}(\nu+1)+e_{22}(13\nu+15))L^2 + 144Iyy^2(\epsilon_{11}+e_{22}+\epsilon_{33})(5\nu+6)}{\sqrt{2}(AL^2+36Iyy)(A(8\nu+9)L^2+12Iyy(5\nu+6))} \\ L^2(-A^2(\epsilon_{11}-e_{22}+2e_{23}-\epsilon_{33})(8\nu+9)L^4 + 12AIyy(-48\nu e_{23}-54e_{23}+15\epsilon_{33}+13\epsilon_{33}\nu+3\epsilon_{11}(\nu+1)+e_{22}(13\nu+15))L^2 + 144Iyy^2(\epsilon_{11}+e_{22}+\epsilon_{33})(5\nu+6)}{\sqrt{2}(AL^2+36Iyy)(A(8\nu+9)L^2+12Iyy(5\nu+6))} \\ L^2(A^2(\epsilon_{11}-e_{22}-2\epsilon_{31}+\epsilon_{33})(8\nu+9)L^4 + 12AIyy(-48\nu e_{31}-54e_{31}+15\epsilon_{33}+13\epsilon_{33}\nu+3e_{22}(\nu+1)+\epsilon_{11}(13\nu+15))L^2 + 144Iyy^2(\epsilon_{11}+e_{22}+\epsilon_{33})(5\nu+6)}{\sqrt{2}(AL^2+36Iyy)(A(8\nu+9)L^2+12Iyy(5\nu+6))} \\ L^2(A^2(\epsilon_{11}-e_{22}+2\epsilon_{31}+\epsilon_{33})(8\nu+9)L^4 + 12AIyy(48\nu e_{31}+54e_{31}+15\epsilon_{33}+13\epsilon_{33}\nu+3e_{22}(\nu+1)+\epsilon_{11}(13\nu+15))L^2 + 144Iyy^2(\epsilon_{11}+e_{22}+\epsilon_{33})(5\nu+6)}{\sqrt{2}(AL^2+36Iyy)(A(8\nu+9)L^2+12Iyy(5\nu+6))} \\ L^2(A^2(\epsilon_{11}+2e_{12}+e_{22}-\epsilon_{33})(8\nu+9)L^4 + 12AIyy(13\nu e_{22}+15e_{22}+3\epsilon_{33}+3\epsilon_{33}\nu+6e_{12}(8\nu+9)+\epsilon_{11}(13\nu+15))L^2 + 144Iyy^2(\epsilon_{11}+e_{22}+\epsilon_{33})(5\nu+6)}{\sqrt{2}(AL^2+36Iyy)(A(8\nu+9)L^2+12Iyy(5\nu+6))} \\ L^2(-A^2(\epsilon_{11}-e_{22}+2e_{23}-\epsilon_{33})(8\nu+9)L^4 + 12AIyy(-48\nu e_{23}-54e_{23}+15\epsilon_{33}+13\epsilon_{33}\nu+3\epsilon_{11}(\nu+1)+e_{22}(13\nu+15))L^2 + 144Iyy^2(\epsilon_{11}+e_{22}+\epsilon_{33})(5\nu+6)}{\sqrt{2}(AL^2+36Iyy)(A(8\nu+9)L^2+12Iyy(5\nu+6))} \\ L^2(A^2(\epsilon_{11}-2e_{12}+e_{22}-\epsilon_{33})(8\nu+9)L^4 + 12AIyy(13\nu e_{22}+15e_{22}+3\epsilon_{33}+3\epsilon_{33}\nu-6e_{12}(8\nu+9)+\epsilon_{11}(13\nu+15))L^2 + 144Iyy^2(\epsilon_{11}+e_{22}+\epsilon_{33})(5\nu+6)}{\sqrt{2}(AL^2+36Iyy)(A(8\nu+9)L^2+12Iyy(5\nu+6))} \\ L^2(-A^2(\epsilon_{11}-e_{22}-2e_{23}-\epsilon_{33})(8\nu+9)L^4 + 12AIyy(48\nu e_{23}+54e_{23}+15\epsilon_{33}+13\epsilon_{33}\nu+3\epsilon_{11}(\nu+1)+e_{22}(13\nu+15))L^2 + 144Iyy^2(\epsilon_{11}+e_{22}+\epsilon_{33})(5\nu+6)}{\sqrt{2}(AL^2+36Iyy)(A(8\nu+9)L^2+12Iyy(5\nu+6))} \\ L^2(A^2(\epsilon_{11}-e_{22}+2\epsilon_{31}+\epsilon_{33})(8\nu+9)L^4 + 12AIyy(48\nu e_{31}+54e_{31}+15\epsilon_{33}+13\epsilon_{33}\nu+3e_{22}(\nu+1)+\epsilon_{11}(13\nu+15))L^2 + 144Iyy^2(\epsilon_{11}+e_{22}+\epsilon_{33})(5\nu+6)}{\sqrt{2}(AL^2+36Iyy)(A(8\nu+9)L^2+12Iyy(5\nu+6))} \\ L^2(A^2(\epsilon_{11}-2e_{12}+e_{22}-\epsilon_{33})(8\nu+9)L^4 + 12AIyy(13\nu e_{22}+15e_{22}+3\epsilon_{33}+3\epsilon_{33}\nu-6e_{12}(8\nu+9)+\epsilon_{11}(13\nu+15))L^2 + 144Iyy^2(\epsilon_{11}+e_{22}+\epsilon_{33})(5\nu+6)}{\sqrt{2}(AL^2+36Iyy)(A(8\nu+9)L^2+12Iyy(5\nu+6))} \\ L^2(A^2(\epsilon_{11}-e_{22}-2\epsilon_{31}+\epsilon_{33})(8\nu+9)L^4 + 12AIyy(-48\nu e_{31}-54e_{31}+15\epsilon_{33}+13\epsilon_{33}\nu+3e_{22}(\nu+1)+\epsilon_{11}(13\nu+15))L^2 + 144Iyy^2(\epsilon_{11}+e_{22}+\epsilon_{33})(5\nu+6)}{\sqrt{2}(AL^2+36Iyy)(A(8\nu+9)L^2+12Iyy(5\nu+6))} \\ L^2(A^2(\epsilon_{11}+2e_{12}+e_{22}-\epsilon_{33})(8\nu+9)L^4 + 12AIyy(13\nu e_{22}+15e_{22}+3\epsilon_{33}+3\epsilon_{33}\nu+6e_{12}(8\nu+9)+\epsilon_{11}(13\nu+15))L^2 + 144Iyy^2(\epsilon_{11}+e_{22}+\epsilon_{33})(5\nu+6)}{\sqrt{2}(AL^2+36Iyy)(A(8\nu+9)L^2+12Iyy(5\nu+6))} \end{array} \right)$$

$$\begin{aligned}
F_{y,b} &= \left(\begin{aligned} &\frac{12\text{Iyy}L^2(\epsilon12+\epsilon31)(5\nu+6)}{A(8\nu+9)L^2+12\text{Iyy}(5\nu+6)} \\ &\frac{12\text{Iyy}L^2(\epsilon12-\epsilon31)(5\nu+6)}{A(8\nu+9)L^2+12\text{Iyy}(5\nu+6)} \\ &\frac{12\text{Iyy}L^2(\epsilon12-\epsilon23)(5\nu+6)}{A(8\nu+9)L^2+12\text{Iyy}(5\nu+6)} \\ &\frac{12\text{Iyy}L^2(\epsilon12+\epsilon23)(5\nu+6)}{A(8\nu+9)L^2+12\text{Iyy}(5\nu+6)} \\ &\frac{12\sqrt{2}\text{Iyy}L^2(\epsilon11-\epsilon22)}{AL^2+36\text{Iyy}} \\ &\frac{12\text{Iyy}L^2(\epsilon12-\epsilon31)(5\nu+6)}{A(8\nu+9)L^2+12\text{Iyy}(5\nu+6)} \\ &\frac{12\sqrt{2}\text{Iyy}L^2(\epsilon11-\epsilon22)}{AL^2+36\text{Iyy}} \\ &\frac{12\text{Iyy}L^2(\epsilon12+\epsilon31)(5\nu+6)}{A(8\nu+9)L^2+12\text{Iyy}(5\nu+6)} \\ &\frac{12\text{Iyy}L^2(\epsilon12+\epsilon23)(5\nu+6)}{A(8\nu+9)L^2+12\text{Iyy}(5\nu+6)} \\ &\frac{12\sqrt{2}\text{Iyy}L^2(\epsilon11-\epsilon22)}{AL^2+36\text{Iyy}} \\ &\frac{12\text{Iyy}L^2(\epsilon12-\epsilon23)(5\nu+6)}{A(8\nu+9)L^2+12\text{Iyy}(5\nu+6)} \\ &\frac{12\sqrt{2}\text{Iyy}L^2(\epsilon11-\epsilon22)}{AL^2+36\text{Iyy}} \end{aligned} \right) \\
F_{z,b} &= \left(\begin{aligned} &\frac{12\sqrt{2}\text{Iyy}L^2(\epsilon22-\epsilon33)}{AL^2+36\text{Iyy}} \\ &\frac{12\sqrt{2}\text{Iyy}L^2(\epsilon22-\epsilon33)}{AL^2+36\text{Iyy}} \\ &\frac{12\sqrt{2}\text{Iyy}L^2(\epsilon11-\epsilon33)}{AL^2+36\text{Iyy}} \\ &\frac{12\sqrt{2}\text{Iyy}L^2(\epsilon11-\epsilon33)}{AL^2+36\text{Iyy}} \\ &\frac{12\text{Iyy}L^2(\epsilon23+\epsilon31)(5\nu+6)}{A(8\nu+9)L^2+12\text{Iyy}(5\nu+6)} \\ &\frac{12\sqrt{2}\text{Iyy}L^2(\epsilon22-\epsilon33)}{AL^2+36\text{Iyy}} \\ &\frac{12\text{Iyy}L^2(\epsilon23-\epsilon31)(5\nu+6)}{A(8\nu+9)L^2+12\text{Iyy}(5\nu+6)} \\ &\frac{12\sqrt{2}\text{Iyy}L^2(\epsilon22-\epsilon33)}{AL^2+36\text{Iyy}} \\ &\frac{12\sqrt{2}\text{Iyy}L^2(\epsilon11-\epsilon33)}{AL^2+36\text{Iyy}} \\ &\frac{12\text{Iyy}L^2(\epsilon23+\epsilon31)(5\nu+6)}{A(8\nu+9)L^2+12\text{Iyy}(5\nu+6)} \\ &\frac{12\sqrt{2}\text{Iyy}L^2(\epsilon22-\epsilon33)}{AL^2+36\text{Iyy}} \end{aligned} \right) \\
M_{x,b} &= \left(\begin{aligned} &\frac{6\text{Iyy}L^3(\epsilon12+\epsilon31)}{A(8\nu+9)L^2+12\text{Iyy}(5\nu+6)} \\ &\frac{6\text{Iyy}L^3(\epsilon31-\epsilon12)}{A(8\nu+9)L^2+12\text{Iyy}(5\nu+6)} \\ &\frac{6\text{Iyy}L^3(\epsilon23-\epsilon12)}{A(8\nu+9)L^2+12\text{Iyy}(5\nu+6)} \\ &\frac{6\text{Iyy}L^3(\epsilon12+\epsilon23)}{A(8\nu+9)L^2+12\text{Iyy}(5\nu+6)} \\ &\frac{6\text{Iyy}L^3(\epsilon23+\epsilon31)}{A(8\nu+9)L^2+12\text{Iyy}(5\nu+6)} \\ &\frac{6\text{Iyy}L^3(\epsilon12-\epsilon31)}{A(8\nu+9)L^2+12\text{Iyy}(5\nu+6)} \\ &\frac{6\text{Iyy}L^3(\epsilon31-\epsilon23)}{A(8\nu+9)L^2+12\text{Iyy}(5\nu+6)} \\ &\frac{6\text{Iyy}L^3(\epsilon12+\epsilon31)}{A(8\nu+9)L^2+12\text{Iyy}(5\nu+6)} \\ &\frac{6\text{Iyy}L^3(\epsilon12+\epsilon23)}{A(8\nu+9)L^2+12\text{Iyy}(5\nu+6)} \\ &\frac{6\text{Iyy}L^3(\epsilon23-\epsilon31)}{A(8\nu+9)L^2+12\text{Iyy}(5\nu+6)} \\ &\frac{6\text{Iyy}L^3(\epsilon12-\epsilon23)}{A(8\nu+9)L^2+12\text{Iyy}(5\nu+6)} \\ &\frac{6\text{Iyy}L^3(\epsilon23+\epsilon31)}{A(8\nu+9)L^2+12\text{Iyy}(5\nu+6)} \end{aligned} \right)
\end{aligned}$$

REFERENCES

- [1] J.T. Allison. *Optimal partitioning and coordination decisions in decomposition-based design optimization*. PhD thesis, University of Michigan, 2008.
- [2] Altair Engineering Inc., Troy, MI. *RADIOSS Theory Manual, Version, Revision 5.1*, 2008.
- [3] G.K. Ananthasuresh, S. Kota, and N. Kikuchi. Strategies for systematic synthesis of compliant mems. *Dynamic Systems and Control*, 2:677–686, 1994.
- [4] M. Apfelbeck, S. Kuß, B. Rebele, and B. Schäfer. A systematic approach to reliably characterize soils based on bevameter testing. *Journal of Terramechanics*, 48(5):360–371, 2011.
- [5] M. Apfelbeck, S. Kuß, A. Wedler, A. Gibbesch, B. Rebele, and B. Schäfer. A novel terramechanics testbed setup for planetary rover wheel-soil interaction. In *Proceedings of 11th European Regional Conference of the ISTVS, Bremen, Germany*, 2009.
- [6] D. Apostolopoulos. *Analytic Configuration of Wheeled Robotic Locomotion*. PhD thesis, The Robotics Institute, Carnegie Mellon University, 2001.
- [7] V. Asnani, D. Delap, and C. Creager. The development of wheels for the lunar roving vehicle. *Journal of Terramechanics*, 46(3):89–103, 2009.
- [8] A. Azimi, J. Kovecses, and J. Angeles. Wheel-soil interaction model for rover simulation based on plasticity theory. In *Proceedings of IEEE/RSJ International Conference on Intelligent Robots and Systems (IROS)*, pages 280–285. IEEE, 2011.
- [9] J. Banhart. Manufacture, characterisation and application of cellular metals and metal foams. *Progress in Materials Science*, 46(6):559–632, 2001.
- [10] R. Bauer, W. Leung, and T. Barfoot. Development of a dynamic simulation tool for the exomars rover. In *Proceedings of the 8th International Symposium on Artificial Intelligence, Robotics and Automation in Space*, 2005.

- [11] R. Bauer, W. Leung, and T. Barfoot. Experimental and simulation results of wheel-soil interaction for planetary rovers. In *IEEE/RSJ International Conference on Intelligent Robots and Systems (IROS)*, pages 586–591. IEEE, 2005.
- [12] Z.P. Bažant and M. Christensen. Analogy between micropolar continuum and grid frameworks under initial stress. *International Journal of Solids and Structures*, 8(3):327–346, 1972.
- [13] M.G. Bekker. *Theory of Land Locomotion: The Mechanics of Vehicle Mobility*. University of Michigan Press, 1962.
- [14] M.G. Bekker. *Introduction to Terrain-Vehicle Systems*. University of Michigan Press Ann Arbor, MI, 1969.
- [15] MG Bekker. The development of a moon rover. *Journal of the British Interplanetary Society*, 38:537, 1985.
- [16] M.P. Bendsoe and O. Sigmund. *Topology Optimization: Theory, Methods and Applications*. Springer, 2004.
- [17] R. Briend. Modelling wheel-soil interactions using the discrete element method for tread shape optimization. Master’s thesis, McGill University, 2011.
- [18] R. Briend, P. Radziszewski, and D. Pasini. Virtual soil calibration for wheel-soil interaction simulations using the discrete-element method. *Canadian Aeronautics and Space Journal*, 57(1):59–64, 2011.
- [19] B.B. Burkhalter and M.R. Sharpe. Lunar roving vehicle- historical origins, development and deployment. *British Interplanetary Society, Journal*, 48(5):199–212, 1995.
- [20] D. Cardile, N. Viola, S. Chiesa, and A. Rougier. Applied design methodology for lunar rover elastic wheel. *Acta Astronautica*, 81(1):1–11, 2012.
- [21] W.D. Carrier III. Lunar soil simulation and trafficability parameters. Technical report, Lunar Geotechnical Institute, 2006.
- [22] J.Y. Chen, Y. Huang, and M. Ortiz. Fracture analysis of cellular materials: a strain gradient model. *Journal of the Mechanics and Physics of Solids*, 46(5):789–828, 1998.

- [23] S. Chhaniyara, C. Brunskill, B. Yeomans, MC Matthews, C. Saaj, S. Ransom, and L. Richter. Terrain trafficability analysis and soil mechanical property identification for planetary rovers: A survey. *Journal of Terramechanics*, 2012.
- [24] A.J. Chipperfield and P.J. Fleming. The matlab genetic algorithm toolbox. In *IEEE Colloquium on Applied Control Techniques Using MATLAB*, pages 10/1–10/4. IET, 1995.
- [25] J.R. Cho, H.S. Jeong, and W.S. Yoo. Multi-objective optimization of tire carcass contours using a systematic aspiration-level adjustment procedure. *Journal of Computational Mechanics*, 29(6):498–509, 2002.
- [26] E.J. Cramer, J.E. Dennis Jr, P.D. Frank, R.M. Lewis, and G.R. Shubin. Problem formulation for multidisciplinary optimization. *SIAM Journal on Optimization*, 4(4):754–776, 1994.
- [27] K. Deb. *Multi Objective Optimization Using Evolutionary Algorithms*. John Wiley and Sons, 2001.
- [28] K. Deb, A. Pratap, S. Agarwal, and T. Meyarivan. A fast and elitist multiobjective genetic algorithm: Nsga-ii. *IEEE Transactions on Evolutionary Computation*, 6(2):182–197, 2002.
- [29] T.K. Derry and T.I. Williams. Short history of technology, 1985.
- [30] C.S. Desai, H.V. Phan, and S. Sture. Procedure, selection and application of plasticity models for a soil. *International Journal for Numerical and Analytical Methods in Geomechanics*, 5(3):295–311, 1981.
- [31] V.S. Deshpande, M.F. Ashby, and N.A. Fleck. Foam topology: bending versus stretching dominated architectures. *Acta Materialia*, 49(6):1035–1040, 2001.
- [32] S. Desrochers, D. Pasini, and J. Angeles. Optimum design of a compliant uniaxial accelerometer. *Journal of Mechanical Design*, 132:041011–1, 2010.
- [33] P. Eckart and B. Aldrin. *The Lunar Base Handbook: An Introduction to Lunar Base Design, Development, and Operations*. McGraw-Hill, 2006.
- [34] A. Ellery. Environment–robot interaction the basis for mobility in planetary micro-rovers. *Journal of Robotics and Autonomous Systems*, 51(1):29–39, 2005.

- [35] M.S.A. Elsayed and D. Pasini. Analysis of the elastostatic specific stiffness of 2d stretching-dominated lattice materials. *Mechanics of Materials*, 42(7):709–725, 2010.
- [36] A.C. Eringen. *Microcontinuum Field Theories. I. Foundations and Solids*. Springer-Verlag, New York, 1999.
- [37] A.G. Evans, J.W. Hutchinson, N.A. Fleck, M.F. Ashby, and H.N.G. Wadley. The topological design of multifunctional cellular metals. *Progress in Materials Science*, 46(3):309–327, 2001.
- [38] M. Faragalli, D. Pasini, and P. Radziszewski. A parametric study and experimental testing of lunar-wheel suspension on dynamic terrainability. *Canadian Aeronautics and Space Journal*, 57(1):65–74, 2011.
- [39] M. Faragalli, D. Pasini, and P. Radziszewski. Multi-objective optimization of a segmented lunar wheel concept. In *Proceedings of ASME’s International Design and Engineering Conference & Computers and Information in Engineering Conference*, Washington, DC, August 28-31 2011.
- [40] M. Farhat, E. Dupuis, S. Lake, and A. Salerno. Preliminary design, fabrication and testing of the fw-350 lunar flexible wheel prototype. In *ESA/ESTEC Symposium on Advanced Space Technologies in Robotics and Automation (ASTRA)*, Noordwijk, The Netherlands, April 12-14 2011.
- [41] C.M. Fonseca, P. J. Fleming, et al. Genetic algorithms for multiobjective optimization: Formulation, discussion and generalization. In *Proceedings of the 5th International Conference on Genetic Algorithms*, volume 423, pages 416–423. San Mateo, California, 1993.
- [42] M.I. Frecker, G.K. Ananthasuresh, S. Nishiwaki, N. Kikuchi, and S. Kota. Topological synthesis of compliant mechanisms using multi-criteria optimization. *Journal of Mechanical design*, 119(2):238–245, 1997.
- [43] A. Genta G. Genta. Modeling and nonlinear analysis of an elastic wheel for low-gravity. In *XXXVIII Convegno Nazionale Associazione Italiana per l’Analisi delle Sollecitazioni*, 2009.
- [44] W.B. Garry and J.E. Bleacher. Field geology conducted from the lunar electric rover, nasa desert rats 2009: Strategies for human surface science operations

- on the moon. In *Lunar and Planetary Institute Science Conference*, volume 41, page 2209, 2010.
- [45] L.J. Gibson and M.F. Ashby. *Cellular Solids: Structure and Properties*. Cambridge university press, 1999.
 - [46] M. Gobbi, F. Levi, and G. Mastinu. Multi-objective stochastic optimisation of the suspension system of road vehicles. *Journal of Sound and Vibration*, 298(4):1055–1072, 2006.
 - [47] M. Gobbi and G. Mastinu. Analytical description and optimization of the dynamic behaviour of passively suspended road vehicles. *Journal of sound and vibration*, 245(3):457–481, 2001.
 - [48] D.E. Goldberg. *Genetic Algorithms in Search, Optimization, and Machine Learning*. Addison-Wesley Professional, 1989.
 - [49] B. Hassani and E. Hinton. A review of homogenization and topology optimization ihomogenization theory for media with periodic structure. *Computers & Structures*, 69(6):707–717, 1998.
 - [50] D.R. Headrick. *The Tentacles of Progress: Technology Transfer in the Age of Imperialism, 1850-1940*. Oxford University Press, USA, 1988.
 - [51] S.J. Hollister and N. Kikuchi. A comparison of homogenization and standard mechanics analyses for periodic porous composites. *Computational Mechanics*, 10(2):73–95, 1992.
 - [52] L.L. Howell. *Compliant Mechanisms*. Springer, 2001.
 - [53] R.G. Hutchinson. *Mechanics of Lattice Materials*. PhD thesis, University of Cambridge, 2004.
 - [54] R.G. Hutchinson and N.A. Fleck. The structural performance of the periodic truss. *Journal of the Mechanics and Physics of Solids*, 54(4):756–782, 2006.
 - [55] K. Iagnemma, C. Senatore, B. Trease, R. Arvidson, K. Bennett, A. Shaw, F. Zhou, L. Van Dyke, and R. Lindemann. Terramechanics modeling of mars surface exploration rovers for simulation and parameter estimation. In *Proceedings of ASME’s International Design and Engineering Conference & Computers and Information in Engineering Conference*, Washington, DC, August 28-31 2011.

- [56] K. Iizuka and T. Kubota. Development of a flexible wheel that allows rovers to traverse lunar soil. *Journal of Asian Electric Vehicles*, 7(1):1231–1237, 2009.
- [57] G. Ishigami, M. Otsuki, T. Kubota, and K. Iagnemma. Modeling of flexible and rigid wheels for exploration rover on rough terrain. In *Proceedings of the 28th International Symposium on Space Technology and Science*, 2011.
- [58] I.G. Jang, Y.H. Sung, E.J. Yoo, and B.M. Kwak. Pattern design of a non-pneumatic tyre for stiffness using topology optimization. *Engineering Optimization*, 44(2):119–131, 2012.
- [59] Z. Janosi and B. Hanamoto. The analytical determination of drawbar pull as a function of slip for tracked vehicles in deformable soils. In *Proceedings of the 1st Int Conference on Terrain-Vehicle Systems*, 1961.
- [60] C.H. Jenkins. *Compliant Structures in Nature and Engineering*. WIT Press, 2005.
- [61] B. Jones, P. Visscher, D. Boucher, P. Radziszewski, M. Faragalli, S. Spenler, and D. Apostolopoulos. The juno rover: an extraction vehicle for in-situ resource utilization. In *15th CASI Astronautics Conference (ASTRO)*, Toronto, Canada, May 4-6 2010.
- [62] J. Ju, D.M. Kim, and K. Kim. Flexible cellular solid spokes of a non-pneumatic tire. *Composite Structures*, 94(8):2285–2295, 2012.
- [63] J. Ju and J.D. Summers. Shear compliant hexagonal cellular solids with a shape memory alloy. In *Proceedings of ASME’s International Design and Engineering Conference & Computers and Information in Engineering Conference*, Washington, DC, August 28-31 2011.
- [64] N. Kaveh-Moghaddam. Experimental investigation of lunar prototype wheel traction performance on deformable terrain. Master’s thesis, McGill University, 2011.
- [65] S. A. Khanoki. Mechanical properties of lattice materials via asymptotic homogenization and comparison with alternative homogenization methods. *International Journal of Mechanical Sciences*, 2012 (submitted).
- [66] S.A. Khanoki and D. Pasini. Multiscale design and multiobjective optimization of orthopedic hip implants with functionally graded cellular material. *Journal of biomechanical engineering*, 134:031004, 2012.

- [67] U. Kirsch. *Structural Optimization: Fundamentals and Applications*. Springer-Verlag Berlin Heidelberg, 1993.
- [68] M.A. Knuth, J.B. Johnson, M.A. Hopkins, R.J. Sullivan, and J.M. Moore. Discrete element modeling of a mars exploration rover wheel in granular material. *Journal of Terramechanics*, 49(1):27–36, 2011.
- [69] M. Kokkolaras, Z.P. Mourelatos, and P.Y. Papalambros. Design optimization of hierarchically decomposed multilevel systems under uncertainty. *Journal of Mechanical Design*, 128(2):503–508, 2005.
- [70] R. Krenn and A. Gibbesch. Soft soil contact modeling technique for multi-body system simulation. *Trends in Computational Contact Mechanics, Lecture Notes in Applied and Computational Mechanics*, 58:135–155, 2011.
- [71] G.K. Lau, H. Du, and M.K. Lim. Use of functional specifications as objective functions in topological optimization of compliant mechanism. *Computer methods in applied mechanics and engineering*, 190(34):4421–4433, 2001.
- [72] A.C. Leite and B. Schäfer. Mass, power and static stability optimization of a 4-wheeled planetary exploration rover. In *2nd International Conference on Engineering Optimization. Lisbon, Portugal*, 2010.
- [73] A.C. Leite and B. Schäfer. On multi-objective optimization of planetary exploration rovers applied to exomars-type rovers. In *ESA/ESTEC Symposium on Advanced Space Technologies in Robotics and Automation (ASTRA)*, Noordwijk, The Netherlands, April 12-14 2011.
- [74] L. Li and C. Sandu. On the impact of cargo weight, vehicle parameters, and terrain characteristics on the prediction of traction for off-road vehicles. *Journal of Terramechanics*, 44(3):221–238, 2007.
- [75] W. Li, Y. Huang, Y. Cui, S. Dong, and J. Wang. Trafficability analysis of lunar mare terrain by means of the discrete element method for wheeled rover locomotion. *Journal of Terramechanics*, 47(3):161–172, 2010.
- [76] C.H. Liu, J.Y. Wong, and H.A. Mang. Large strain finite element analysis of sand: model, algorithm and application to numerical simulation of tire-sand interaction. *Computers & Structures*, 74(3):253–265, 2000.
- [77] N. Lobontiu. *Compliant Mechanisms: Design of Flexure Hinges*. CRC Press, 2002.

- [78] J. Ma, J.D. Summers, and P.F. Joseph. Numerical simulation of tread effects on the interaction between cellular shear band based non-pneumatic tire and sand. In *Proceedings of ASME's International Design and Engineering Conference & Computers and Information in Engineering Conference*, Washington, DC, August 28-31 2011.
- [79] J.R.R.A. Martins and A.B. Lambe. Multidisciplinary design optimization: Survey of architectures. *AIAA Journal*, 2012.
- [80] S. Michaud, M. Hoepflinger, T. Thueer, C. Lee, A. Krebs, B. Despont, A. Gibbesch, and L. Richter. Lesson learned from exomars locomotion system test campaign. In *10th ESA Workshop on Advanced Space Technologies for Robotics and Automation (ASTRA)*, Noordwijk, The Netherlands, November 11-14 2008.
- [81] J.C. Michel, H. Moulinec, and P. Suquet. Effective properties of composite materials with periodic microstructure: a computational approach. *Computer methods in applied mechanics and engineering*, 172(1):109–143, 1999.
- [82] H. Nakashima, H. Fujii, A. Oida, M. Momozu, Y. Kawase, H. Kanamori, S. Aoki, and T. Yokoyama. Parametric analysis of lugged wheel performance for a lunar microrover by means of dem. *Journal of terramechanics*, 44(2):153–162, 2007.
- [83] T. Okada, S. Sasaki, T. Sugihara, K. Saiki, H. Akiyama, M. Ohtake, H. Takeda, N. Hasebe, M. Kobayashi, J. Haruyama, et al. Lander and rover exploration on the lunar surface: A study for selene-b mission. *Advances in Space Research*, 37(1):88–92, 2006.
- [84] HA Oravec, X. Zeng, and VM Asnani. Design and characterization of grc-1: A soil for lunar terramechanics testing in earth-ambient conditions. *Journal of Terramechanics*, 47(6):361–377, 2010.
- [85] M.K. Orr. Development of a finite element model to predict the behavior of a prototype wheel on lunar soil. Master's thesis, Clemson University, 2010.
- [86] N. Patel, R. Slade, and J. Clemmet. The exomars rover locomotion subsystem. *Journal of Terramechanics*, 47(4):227–242, 2010.
- [87] B.O. Peirce. *A Short Table of Integrals*. Ginn, New York, 1897.

- [88] M. Powell. A fast algorithm for nonlinearly constrained optimization calculations. *Numerical analysis, Lecture Notes in Mathematics*, 630:144–157, 1978.
- [89] J.P. Pruiksma, J.A.M. Teunissen, G.A.M. Kruse, and M. Van Winnendael. Tractive performance modelling of the exomars rover wheel design on loosely packed soil using the coupled eulerian lagrangian finite element technique. In *ESA/ESTEC Symposium on Advanced Space Technologies in Robotics and Automation (ASTRA)*, Noordwijk, The Netherlands, April 12-14 2011.
- [90] P. Radziszewski, S. Martins, M. Faragalli, N. Kaveh-Moghaddam, D. Oyama, R. Briend, N. Gharib, C. Prahacs, S. Ouellette, D. Pasini, et al. ings: development of a wheel prototype concept for lunar mobility. *Canadian Aeronautics and Space Journal*, 57(1):1–11, 2011.
- [91] X.C. Ren and Z.H. Yao. Structure optimization of pneumatic tire using an artificial neural network. *Advances in Neural Networks Lecture Notes in Computer Science*, 3174:841–847, 2004.
- [92] J.D. Renton. *Elastic Beams and Frames*. Woodhead Publishing, 2002.
- [93] T.B. Rhyne and S.M. Cron. Development of a non-pneumatic wheel. *Tire Science and Technology*, 34(3):150–169, 2006.
- [94] W. Rozema. The use of spectral analysis in describing lunar surface roughness. *US Geological Survey*, pages 180–188, 1968.
- [95] T.A. Schaedler, A.J. Jacobsen, A. Torrents, A.E. Sorensen, J. Lian, J.R. Greer, L. Valdevit, and W.B. Carter. Ultralight metallic microlattices. *Science*, 334(6058):962–965, 2011.
- [96] B. Schäfer, A. Gibbesch, R. Krenn, and B. Rebele. Planetary rover mobility simulation on soft and uneven terrain. *Vehicle System Dynamics*, 48(1):149–169, 2010.
- [97] B. Schäfer, A.C. Leite, and B. Rebele. Development environment for optimized locomotion system of planetary rovers. In *14th International Symposium on Dynamic Problems of Mechanics*, São Sebastião, São Paulo, Brazil, March 13-18 2011.
- [98] J. Schmitt, G. Heiken, D. Vaniman, and B.M. French. *Lunar Sourcebook: A User's Guide to the Moon*. Cambridge University Press, 1991.

- [99] K. Skonieczny, D.S. Wettergreen, et al. Parameters governing regolith site work by small robots. In *ASCE Earth & Space Conference*, Honolulu, Hawaii, March 14-17 2010. Citeseer.
- [100] J.J. Skrzypek, A.W. Ganczarski, F. Rustichelli, and H. Egner. *Advanced Materials and Structures for Extreme Operating Conditions*. Springer, 2008.
- [101] J. Sobieszczanski-Sobieski. Optimization by decomposition in structural and multidisciplinary optimization. *Optimization of large structural systems*, 1:193–234, 1993.
- [102] J. Sobieszczanski-Sobieski and R.T. Haftka. Multidisciplinary aerospace design optimization: survey of recent developments. *Structural and Multidisciplinary Optimization*, 14(1):1–23, 1997.
- [103] J. Stampfl, H. Fouad, S. Seidler, R. Liska, F. Schwager, A. Woesz, and P. Fratzl. Fabrication and moulding of cellular materials by rapid prototyping. *International Journal of Materials and Product Technology*, 21(4):285–296, 2004.
- [104] D. Stowe, K. Conger, J.D. Summers, P. Joseph, B. Thompson, and J. Matthews. Designing a lunar wheel. In *Proceedings of ASME’s International Design and Engineering Conference & Computers and Information in Engineering Conference*, Brooklyn, NY, August 3-6 2008.
- [105] G.S. Sukhatme, G.A. Bekey, et al. An evaluation methodology for autonomous mobile robots for planetary exploration. In *1st ECPD International Conference on Advanced Robotics and Intelligent Automation*, pages 558–563, 1995.
- [106] B.P. Taylor. Experimental evaluation and semi-empirical modeling of the tractive performance of rigid and flexible wheels on lunar soil simulant. Master’s thesis, Virginia Polytechnic Institute and State University, 2009.
- [107] C.P. Teng, S. Bai, and J. Angeles. Shape synthesis in mechanical design. *Acta Polytechnica*, 47(6):56–62, 2007.
- [108] N. Thyagaraja, P. Shankar, G. Fadel, and P. Guarneri. Optimizing the shear beam of a non-pneumatic wheel for low rolling resistance. In *ASME’s International Design and Engineering Conference & Computers and Information in Engineering Conference*, Washington, DC, August 28- 31 2011.
- [109] B. Trease, R. Arvidson, R. Lindemann, K. Bennett, F. Zhou, K. Iagnemma, C. Senatore, and L. Van Dyke. Dynamic modeling and soil mechanics for path

- planning of mars exploration rovers. In *ASME's International Design and Engineering Conference & Computers and Information in Engineering Conference*, Washington, DC, August 28- 31 2011.
- [110] J.M. Tyrus, M. Gosz, and E. DeSantiago. A local finite element implementation for imposing periodic boundary conditions on composite micromechanical models. *International Journal of Solids and Structures*, 44(9):2972–2989, 2007.
 - [111] M. Veeramurthy, J. Ju, L.L. Thompson, and J.D. Summers. Optimization of a non-pneumatic tire for reduced rolling resistance. In *ASMEs International Design and Engineering Conference & Computers and Information in Engineering*, Washington, DC, August 28-31 2011.
 - [112] G. Verros, S. Natsiavas, and C. Papadimitriou. Design optimization of quarter-car models with passive and semi-active suspensions under random road excitation. *Journal of Vibration and Control*, 11(5):581–606, 2005.
 - [113] A. Vigliotti and D. Pasini. Linear multiscale analysis and finite element validation of stretching and bending dominated lattice materials. *Mechanics of Materials*, 46:57–68, 2012.
 - [114] A. Vigliotti and D. Pasini. Stiffness and strength of tridimensional periodic lattices. *Computer Methods in Applied Mechanics and Engineering*, 229-232:27–43, 2012.
 - [115] H.N.G. Wadley. Multifunctional periodic cellular metals. *Philosophical Transactions of the Royal Society A: Mathematical, Physical and Engineering Sciences*, 364(1838):31–68, 2006.
 - [116] A.J. Wang and D.L. McDowell. In-plane stiffness and yield strength of periodic metal honeycombs. *Journal of Engineering Materials and Technology*, 126(2):137–156, 2004.
 - [117] D. Wettergreen, D. Jonak, D. Kohanbash, SJ Moreland, S. Spiker, J. Teza, and WRL Whittaker. Design and experimentation of a rover concept for lunar crater resource survey. In *47th AIAA Aerospace Sciences Meeting Including The New Horizons Forum and Aerospace Exposition*, 2009.
 - [118] A. Wilkinson and A. DeGennaro. Digging and pushing lunar regolith: Classical soil mechanics and the forces needed for excavation and traction. *Journal of Terramechanics*, 44(2):133–152, 2007.

- [119] J.Y. Wong. *Theory of Ground Vehicles*. Wiley, 2008.
- [120] J.Y. Wong. Predicting the performances of rigid rover wheels on extraterrestrial surfaces based on test results obtained on earth. *Journal of Terramechanics*, 2011.
- [121] J.Y. Wong and V.M. Asnani. Study of the correlation between the performances of lunar vehicle wheels predicted by the nepean wheeled vehicle performance model and test data. *Proceedings of the Institution of Mechanical Engineers, Part D: Journal of Automobile Engineering*, 222(11):1939–1954, 2008.
- [122] A.C. Woodward. Experimental analysis of the effects of the variation of draw-bar pull test parameters for exploration vehicles on gre-1 lunar soil simulant. Master’s thesis, Virginia Polytechnic Institute and State University, 2011.
- [123] Z. Xia, Y. Zhang, and F. Ellyin. A unified periodical boundary conditions for representative volume elements of composites and applications. *International Journal of Solids and Structures*, 40(8):1907–1921, 2003.
- [124] Z. Xia, C. Zhou, Q. Yong, and X. Wang. On selection of repeated unit cell model and application of unified periodic boundary conditions in micro-mechanical analysis of composites. *International Journal of Solids and Structures*, 43(2):266–278, 2006.
- [125] R.N. Yong and F. Eiyo. Road surface roughness and tyre performance. *Journal of Terramechanics*, 27(3):219–239, 1990.
- [126] R.N. Yong, E.A. Fattah, and P. Boonsinsuk. Analysis and prediction of tyre-soil interaction and performance using finite elements. *Journal of Terramechanics*, 15(1):43–63, 1978.